

**NUMERICAL CLOSED-FORM SOLUTIONS OF SKIN  
FLAP SURGERIES USING 3D FACE MODELS**

**NUR NADIRAH BINTI KHAIRU NAJHAN**

**DISSERTATION SUBMITTED IN FULFILMENT OF THE  
REQUIREMENTS FOR THE DEGREE OF MASTER OF  
ENGINEERING SCIENCE**

**FACULTY OF ENGINEERING  
UNIVERSITY OF MALAYA  
KUALA LUMPUR**

**2021**

## ORIGINAL LITERARY WORK DECLARATION

Name of Candidate: Nur Nadirah Binti Khairu Najhan

Matric No: 17198449/1

Name of Degree: Master of Engineering Science

Title of Thesis ("this Work"): Numerical Closed-form Solutions of Skin Flap Surgeries Using 3D Face Models

Field of Study: 1. Biomechanics

2. Computer-Aided Design

I do solemnly and sincerely declare that:

- (1) I am the sole author/writer of this Work;
- (2) This Work is original;
- (3) Any use of any work in which copyright exists was done by way of fair dealing and for permitted purposes and any excerpt or extract from, or reference to or reproduction of any copyrighted work has been disclosed expressly and sufficiently and the title of the Work and its authorship have been acknowledged in this Work;
- (4) I do not have any actual knowledge nor do I ought reasonably to know that the making of this work constitutes an infringement of any copyrighted work;
- (5) I hereby assign all and every right in the copyright to this Work to the University of Malaya ("UM"), who henceforth shall be the owner of the copyright in this Work and that any reproduction or use in any form or by any means whatsoever is prohibited without the written consent of UM having been first had and obtained;
- (6) I am fully aware that if in the course of making this Work I have infringed any copyright whether intentionally or otherwise, I may be subject to legal action or any other action as may be determined by UM.

Candidate's Signature

Date: 13/12/2021

Subscribed and solemnly declared before,

Witness's Signature

Date: 13/12/2021

Name:

Designation:

# NUMERICAL CLOSED-FORM SOLUTIONS OF SKIN FLAP SURGERIES USING 3D FACE MODELS

## ABSTRACT

A computational-based surgical simulation that typically relies on the Finite Element method has added value to surgical planning. A plethora of FE modeling in local flap surgery has been developed to better understand the biomechanics of local flaps. However, to the best of our knowledge, none considered using a three-dimensional head template as a base model as well as associating ethnic and gender demographics. Therefore, the present work aims to address these gaps, including exploring the stress profiles of three common flap designs on their respective anatomic locations. It is expected that incorporating three-dimensional patient-like models into the simulations would provide better post-operative visualization of facial reconstruction instead of two-dimensional planar approaches as well as serves as training aids and pre-operative patient information. The intended study began with creating a set of facial deformities using a Caucasian-like head template. The deformities were formed by cut-extruding a set of local flap designs: advancement, rotation, and rhomboid flaps at three different facial locations: forehead, cheek, and temple, respectively. These local flaps were embedded in the outermost face layer (epidermis). Concurrently, a single layer of skin thicknesses and third-order Yeoh hyper-elastic skin properties were adopted from the work of existing literature and implemented into the face models to accommodate the realization of human skin behaviors. The post-operative simulations demonstrated standard local flap closures along with the commonplaces of peak tensions in which were found consistent with the available literature. Additionally, Burow's triangles were superimposed on the advancement and rotation flaps to assist the mobility of the flaps

towards the defect. The study was then further in applying the original method to Asian-like head templates with a focus on gender-related differences. Rotation and rhomboid flaps demonstrated maximal tension at the apex of the flap for both genders as well as advancement flap in the female face model. However, advancement flap closure in the male face model presented otherwise. Yet, the deformation patterns and the maximal tension of the discussed flaps were consistent with the conventional. Moreover, male face models generated higher stress compared to the female face models with a 70.34% mean difference. Overall, these operations were executed manually and the designed surgery models met the objectives successfully while acknowledging the study limitations. Future work will involve the adoption of multiple layering, pre-stress effects, and specific material properties according to a particular demographic.

Keywords: *Facial Reconstruction, Local Flap, Hyper-elastic, Deformation, and Wound Closure.*

# NUMERASI PENYELESAIAN PENUTUPAN PEMBEDAHAN KULIT MENGUNAKAN MODEL 3D WAJAH

## ABSTRAK

Simulasi pembedahan berasaskan komputasi yang kebiasaanya bergantung kepada kaedah 'Finite Element' mempunyai nilai tambahan pada pra-operasi pembedahan. Sejumlah besar pemodelan 'Finite Element' dalam operasi 'local flap' telah dikembangkan dengan lebih baik untuk memahami biomekanik 'local flap'. Namun, sepanjang pengetahuan kami, tiada yang mempertimbangkan untuk menggunakan templat tiga dimensi sebagai model asas dan juga mengaplikasikan demografi etnik dan jantina. Oleh itu, hasil kerja ini bertujuan untuk mengatasi jurang yang sedia ada dan termasuk meneroka profil tekanan tiga umum reka bentuk 'local flap' di tiga lokasi anatomi. Dijangkakan dengan memasukkan tiga dimensi model seakan muka pesakit ke dalam simulasi akan memberikan hasil visualisasi rekonstruktif pembedahan wajah yang lebih baik berbanding dengan pendekatan dua dimensi yang juga akan berfungsi sebagai tujuan latihan dan maklumat pesakit pra-operasi. Kajian ini bermula dengan mencipta satu set luka di muka menggunakan templat seakan kepala Kaukasian. Luka itu dibentuk oleh potongan-potongan ekstrusi reka 'local flap': 'advancement flap', 'rotation flap', dan 'rhomboid flap' di tiga lokasi muka yang berbeza iaitu dahi, pipi, dan pelipis. 'Local flap' ini terletak di lapisan muka paling luar (epidermis). Pada masa yang sama, satu lapisan kulit dan sifat kulit yang hiperelastik daripada Yeoh kelas ketiga diadaptasikan daripada karya sastera yang sedia ada dan diterapkan ke dalam model wajah dengan tujuan untuk merealisasikan tingkah laku kulit manusia. Simulasi pasca-pembedahan menunjukkan penutupan 'local flap' yang standard bersama dengan

lokasi ketegangan maksima yang sama dengan karya sastera sedia ada. Selain itu, 'Burow's triangle' dilapiskan bersama dengan 'advancement flap' dan 'rotation flap' untuk membantu pergerakan 'flap' ke arah luka. Kajian ini seterusnya menerapkan kaedah yang sama pada templat seakan kepala Asia dengan memfokuskan pada perbezaan antara jantina. 'Rotation flap' dan 'rhomboid flap' menunjukkan ketegangan maksima pada puncak 'flap' bagi kedua-dua jantina dan begitu juga dengan 'advancement flap' bagi model berwajahkan wanita. Walau bagaimanapun, penutupan 'flap' pada model berwajahkan lelaki menunjukkan hasil yang berbeza. Namun, corak ubah bentuk dan ketegangan maksima dari 'flap' serasi dengan konvensional. Tambahan pula, model berwajahkan lelaki menghasilkan tekanan yang lebih tinggi berbanding dengan model berwajahkan wanita dengan perbezaan minima 70.34%. Secara keseluruhan, operasi ini dilaksanakan secara manual dan simulasi berdasarkan bedah rekonstruksi memenuhi objektif dengan jaya dengan mengakui batasan yang wujud sepanjang kajian ini dilakukan. Di masa hadapan, kajian ini akan menggunakan pelbagai lapisan, kesan pra-tekanan, dan sifat bahan tertentu sesuai dengan demografi tertentu.

Kata kunci: *Rekonstruksi Muka, Analisis Elemen Hingga, Hiperelastik, Deformasi, dan Penutupan Luka.*

## ACKNOWLEDGEMENTS

This research would not have been accomplished without enormous support and cooperation from countless inspirational people. First and foremost, thank you to my parents for their unceasing love, prayers, and support for educating and grooming me for my future.

My deepest gratitude then goes to my research supervisor, Professor Ir. Dr. Yau Yat Huang, whose encouragement, guidance, and support throughout the stages enabled me to finish the research successfully. His suggestions and ways of troubleshooting the problem help me to understand the issues and effectively improvise the project. My appreciation also extends to my second research supervisor, Dr. Kwan Zhenli from the Faculty of Medicine, University of Malaya, whose assistance and suggestions have been especially valuable. This research has been a success because of these two important people and I am deeply thankful.

I convey my gratitude to Professor Yan Luximon from The Hong Kong Polytechnic University, Hong Kong for providing me with one of her works, the head templates, that shaped the present work. Also, a thank you to Dr. Fethma M Nor from Curtin University, Malaysia for her kind suggestions and knowledge in the area of face reconstruction modeling.

Above all, I would like to express my appreciation to God for his blessings by providing me with the opportunity to finish the research in time by giving me good health.

## TABLE OF CONTENTS

<b>ABSTRACT .....</b>	<b>iii</b>
<b>ACKNOWLEDGEMENTS.....</b>	<b>vii</b>
<b>TABLE OF CONTENTS.....</b>	<b>viii</b>
<b>LIST OF FIGURES .....</b>	<b>xi</b>
<b>LIST OF TABLES .....</b>	<b>xvi</b>
<b>LIST OF SYMBOLS AND ABBREVIATIONS .....</b>	<b>xvii</b>
<b>CHAPTER 1 .....</b>	<b>1</b>
<b>1.1 Background .....</b>	<b>1</b>
<b>1.2 Problem Statement .....</b>	<b>3</b>
<b>1.3 Research Objectives .....</b>	<b>3</b>
<b>1.4 Novelty of Research .....</b>	<b>4</b>
<b>1.5 Scope of Work.....</b>	<b>4</b>
<b>CHAPTER 2 .....</b>	<b>7</b>
<b>2.1 Local Flap Surgery .....</b>	<b>7</b>
<b>2.2 Surgical Techniques .....</b>	<b>11</b>
<b>2.2.1 Advancement flaps .....</b>	<b>11</b>
<b>2.2.2 Rotation flaps .....</b>	<b>14</b>
<b>2.2.3 Rhomboid flap .....</b>	<b>19</b>

<b>2.3</b>	<b>Skin Anatomy .....</b>	<b>21</b>
2.3.1	<i>Components and functions of human skin.....</i>	21
2.3.2	<i>Skin Thicknesses.....</i>	23
<b>2.4</b>	<b>Mechanical Behavior of the Skin .....</b>	<b>28</b>
2.4.1	<i>Nonlinear stress-strain relationship .....</i>	28
2.4.2	<i>Anisotropy and viscoelasticity behavior .....</i>	30
<b>2.5</b>	<b>Skin Constitutive Modeling .....</b>	<b>31</b>
2.5.1	<i>Linear-elastic modeling .....</i>	31
2.5.2	<i>Hyper-elastic modeling.....</i>	33
<b>2.6</b>	<b>Deriving Constitutive Model Equation.....</b>	<b>36</b>
<b>2.7</b>	<b>Wound Closure Simulation .....</b>	<b>39</b>
<b>2.8</b>	<b>Summary for Literature Survey .....</b>	<b>41</b>
<b>CHAPTER 3 .....</b>		<b>43</b>
<b>3.1</b>	<b>Case Study 1: Caucasian Model.....</b>	<b>43</b>
3.1.1	<i>Face model .....</i>	46
3.1.2	<i>Local flap designs .....</i>	48
3.1.3	<i>Material constitutive model.....</i>	51
3.1.4	<i>Finite element mesh.....</i>	52
3.1.5	<i>Boundary conditions .....</i>	60
3.1.6	<i>Assumptions on the FE analysis model.....</i>	63

<b>3.2</b>	<b>Case Study 2: Asian Models</b> .....	<b>63</b>
3.2.1	<i>Face model</i> .....	65
3.2.2	<i>Local flap designs</i> .....	68
3.2.3	<i>Material constitutive model</i> .....	70
3.2.4	<i>Finite element mesh</i> .....	70
3.2.5	<i>Boundary conditions</i> .....	81
3.2.6	<i>Assumptions on the FE analysis model</i> .....	86
<b>CHAPTER 4</b>	.....	<b>88</b>
4.1	<b>Case Study 1: Caucasian Model</b> .....	88
4.2	<b>Case Study 2: Asian Models</b> .....	94
<b>CHAPTER 5</b>	.....	<b>104</b>
5.1	<b>Case Study 1 – Accuracy and Stress Evaluation</b> .....	106
5.2	<b>Case Study 2 – The Sensitiveness of Local Flaps Towards Gender Group</b> 111	
<b>CHAPTER 6</b>	.....	<b>114</b>
<b>REFERENCES</b>	.....	<b>117</b>
<b>LIST OF PUBLICATION AND PAPER PRESENTED</b>	.....	<b>123</b>
<b>CO-AUTHORS CONSENT</b>	.....	<b>124</b>

## LIST OF FIGURES

<b>Figure 2.1.</b> Local flap techniques (a) advancement flap: moves linearly sliding forward over the underlying tissue (b) rotation flap: rotates about point central to the triangular-shaped wound (c) transposition flap: rectangular flap rotates across the tissue in the wound. ....	8
<b>Figure 2.2.</b> Relaxed skin tension lines (RSTL) are drawn on the diagram of a human face. (Kaufman, 2016).....	10
<b>Figure 2.3.</b> Classic advancement flap. (A) The defect was squared off along with the incision lines drawn adjacent to the forehead rhytides. (B) Wound sutured following the excision and reconstruction. (C) Post-operative surgery result. (Turner & Smith, 2011).....	14
<b>Figure 2.4.</b> Classic rotation flap. (A) Circular-shaped wound following the excision of a lentigo maligna. (B) Sutured wound after flap (C) Postoperative surgery result. (Kaufman, 2016).....	19
<b>Figure 2.5.</b> Classic rhomboid flap. (A) 60° and 120° angles of a rhombus-shaped wound with four possible flap options. (B) The resulting shape and suture of the flap. (Momeni & Souza, 2019).....	20
<b>Figure 2.6.</b> Classic rhomboid flap. (A) Round-shaped wound adjacent to the eyebrow area. (B) Wound sutured after flap. (C) Postoperative surgery result. (Kaufman, 2016).....	21
<b>Figure 2.7.</b> Architectural representation of human skin and its components (McGrath & J., 2010). ....	22
<b>Figure 2.8.</b> In vitro skin thickness measurement between 82 years old female and 78 years old male cadavers against 15 head anatomical locations. [Reproduced from Ha et al. (2005)] .....	26
<b>Figure 2.9.</b> In vivo skin thickness measurement between 10 females and 8 males subjects with a median of 26 years against 21 body sites [Reproduced from L. Overgaard Olsen et al. (1995)]	26
<b>Figure 2.10.</b> In vivo skin thickness measurement between four different ethnic groups against three body sites (Querleux et al., 2009). ....	27
<b>Figure 2.11.</b> In vivo skin thickness measurement between three different ethnic groups against four body sites (Laurent et al., 2007). ....	27

<b>Figure 2.12.</b> J-shaped nonlinear response of the skin stress-strain curve due to the corresponding collagen fibers to the direction of the stress. [Redrawn and modified based on Kalra et al. (2016)].	29
<b>Figure 3.1.</b> The methodology used in designing a 3D wound closure.	44
<b>Figure 3.2.</b> Untextured mesh and low quadrilateral-shaped cells were observed on the Turbosquid 3D head template of a Caucasian male which was obtained from an open-source platform. (A) Front view. (B) Isometric view. [Obtained from Mad Mouse Design (2007)].	47
<b>Figure 3.3.</b> A restructured and redefined quadrilateral-shaped cells of a Caucasian head template. (A) Front view. (B) Isometric view.	48
<b>Figure 3.4.</b> Geometrical descriptions of (A) advancement flap (B) rotation flap and (C) rhomboid flap. All measurements are in mm unit.	50
<b>Figure 3.5.</b> Meshed base face model using tetrahedral mesh method. (A) Full view (B) Close-up view.	54
<b>Figure 3.6.</b> Meshed base model using hex dominant mesh method. (A) Full view (B) Close-up view.	55
<b>Figure 3.7.</b> Jacobian ratio of the tetrahedral mesh (left) and hex dominant mesh (right).	56
<b>Figure 3.8.</b> Skewness of the tetrahedral mesh (left) and hex dominant mesh (right).	56
<b>Figure 3.9.</b> Meshed geometries of advancement flap with the tetrahedral mesh assuming that forehead thickness was 1.22 mm, element size of 2.60 mm and a total of 124 862 elements (A) Caucasian model with an opening advancement-shaped hole. (B) Area of interest at closed proximity.	57
<b>Figure 3.10.</b> Meshed geometries of rotation flap with the tetrahedral mesh assuming that cheek thickness was 1.34 mm, element size of 2.60 mm and a total of 124 717 elements (A) Caucasian model with an opening rotation-shaped hole. (B) Area of interest at closed proximity.	58
<b>Figure 3.11.</b> Meshed geometries of the rhomboid flap with the tetrahedral mesh assuming that temple thickness was 1.29 mm, element size of 2.60 mm and a total of 124 238 elements (A) Caucasian model with an opening rhomboid-shaped hole. (B) Area of interest at closed proximity.	59

<b>Figure 3.12.</b> The overall workflow. ....	64
<b>Figure 3.13.</b> An unstructured grid with triangular-shaped cells was observed on the SizeChina 3D head template of an Asian female obtained from a creditable source. (A) Front view. (B) Isometric view.....	66
<b>Figure 3.14.</b> Quadrilateral-shaped cells of the female head template. (A) Front view. (B) Isometric view.....	67
<b>Figure 3.15.</b> An unstructured grid with triangular-shaped cells was observed on the SizeChina 3D head template of an Asian male obtained from a creditable source. (A) Front view. (B) Isometric view.....	67
<b>Figure 3.16.</b> Quadrilateral-shaped cells of the male head template. (A) Front view. (B) Isometric view.....	68
<b>Figure 3.17.</b> Geometrical descriptions of (A) advancement flap (B) rotation flap and (C) rhomboid flap. All measurements are in mm unit.....	69
<b>Figure 3.18.</b> Meshed base face model from tetrahedral mesh method. (A) Meshed female face model in full view (left) and close-up view (right) (B) Meshed male face model in full view (left) and at closed proximity (right).....	72
<b>Figure 3.19.</b> Meshed base face model using the hex dominant mesh method. (A) Meshed female face model in full view (left) and at the closed view (B) Meshed male face model in full view (left) and at closed view. ....	74
<b>Figure 3.20.</b> Tetrahedral method generated the best mesh quality out of Jacobian ratio. (A) Meshed female face model in the tetrahedral mesh (left) and hex dominant mesh (right). (B) Meshed male face model in the tetrahedral mesh (left) and hex dominant mesh (right).....	76
<b>Figure 3.21.</b> Tetrahedral method generated the best mesh quality out of skewness. (A) Meshed female face model in the tetrahedral mesh (left) and hex dominant mesh (right). (B) Meshed male face model in the tetrahedral mesh (left) and hex dominant mesh (right).....	77
<b>Figure 3.22.</b> Meshed geometries of advancement flap with the tetrahedral mesh assuming that forehead thickness was 1.22 mm and 2.20 mm element size (A) From left to right: female (63	

037 elements) and male (64 419 elements) face models. <b>(B)</b> Area of interest at close proximity. .....	78
<b>Figure 3.23.</b> Meshed geometries of rotation flap with the tetrahedral mesh assuming that cheek thickness was 1.34 mm and 2.20 mm element size <b>(A)</b> From left to right: female (65 221 elements) and male (63 470 elements) face models. <b>(B)</b> Area of interest at close proximity.....	79
<b>Figure 3.24.</b> Meshed geometries of the rhomboid flap with the tetrahedral mesh assuming that temple thickness was 1.29 mm and 2.20 mm element size <b>(A)</b> From left to right: female (63 029 elements) and male (62 222 elements) face models. <b>(B)</b> Area of interest at close proximity.....	80
<b>Figure 4.1.</b> Sequential steps of closed-form simulations of advancement, rotation, and rhomboid flaps for the Caucasian face model are shown from left to right. ....	90
<b>Figure 4.2.</b> Advancement flap closure on the Caucasian face model. Maximal von Mises stress concentrated on one side of lateral corners. ....	91
<b>Figure 4.3.</b> Rotation flap closure on the Caucasian face model. Maximal von Mises stress concentrated along the distal border of the flap. ....	92
<b>Figure 4.4.</b> Rhomboid flap closure on the Caucasian face model. Maximal von Mises stress concentrated at the point of rhombus edges adjacent to the primary defect closure. ....	93
<b>Figure 4.5.</b> Sequential steps of closed-form simulations of advancement, rotation, and rhomboid flaps for Asian female are shown from left to right. ....	96
<b>Figure 4.6.</b> Sequential steps of closed-form simulations of advancement, rotation, and rhomboid flaps for the Asian male face model are shown from left to right.....	97
<b>Figure 4.7.</b> Advancement flap closure on the Asian female face model. Maximal von Mises stress concentrated on one side of lateral corners. ....	98
<b>Figure 4.8.</b> Advancement flap closure on a male face model. Maximal von Mises concentrated at the border of the incision lines. ....	99
<b>Figure 4.9.</b> Rotation flap closure on the Asian female face model. Maximal von Mises stress concentrated at the tip of Burow’s triangle. ....	100
<b>Figure 4.10.</b> Rotation flap closure on a male face model. Maximal von Mises stress concentrated at the tip of Burow’s triangle. ....	101

<b>Figure 4.11.</b> Rhomboid flap closure on the Asian female face model. Maximal von Mises stress concentrated at the point of rhombus edges adjacent to the primary defect closure.....	102
<b>Figure 4.12.</b> Rhomboid flap closure on the Asian male face model. Maximal von Mises stress concentrated at the point of rhombus edges adjacent to the primary defect closure.....	103
<b>Figure 5.1.</b> J-shaped nonlinear curve of the skin stress-strain generated from the existing material coefficients, $c_{10}$ , $c_{20}$ , and $c_{30}$ .....	106
<b>Figure 5.2.</b> Findings from the work of Lee et al. (2019) that focused on advancement, rotation and rhomboid flap. Advancement flap produced higher stress at the linear corner of the flap base. Rotation flap produced greater stress distal to the flap. The Rhomboid flap exerted maximal stress at the point of rhombus edges near to the secondary closure.....	109
<b>Figure 5.3.</b> Findings from the work of Tepole et al. (2014) focused on direct advancement flap with parallel and perpendicular collagen fiber orientations. Both cases exerted maximal stresses at the distal edges of the flaps. ....	110
<b>Figure 5.4.</b> Findings from the work of Rajabi et al. (2015). Limberg flap with $\phi = \theta_2 = 60^\circ$ and $\theta_1 = 0$ and edges of equal lengths. The flap exerted maximal stress at a point of distal edges adjacent to the primary closure.....	111

## LIST OF TABLES

<b>Table 2.1.</b> The terminology used in local flap surgery.....	11
<b>Table 2.2.</b> Listing of advancement flaps. (Baker, 2015) .....	12
<b>Table 2.3.</b> Listing of rotation flaps. (Dockery, 2012).....	15
<b>Table 2.4.</b> Summary of several works of literature on the skin's Young's modulus measurement. FR: forearm at rest, IFL: isometric flexor loading, IEL: isometric extensor loading, VO: venous occlusion. ....	33
<b>Table 2.5.</b> Four commonly used hyper-elastic models. $c_{ij}$ = material constant, $\mu$ = shear modulus, $\lambda_i$ = principle stretch and $\alpha_i$ = strain hardening exponent.....	34
<b>Table 3.1.</b> Skin thickness values for the corresponded anatomical location. [Obtained from Chopra et al. (2015)] .....	48
<b>Table 3.2.</b> Material parameters of the Yeoh model. The coefficients $c_{10}$ , $c_{20}$ , and $c_{30}$ are defined as material constants whereas $d_1$ , $d_2$ , and $d_3$ are the incompressibility constraints. [Obtained from (Chanda & Unnikrishnan, 2017)].....	52
<b>Table 3.3.</b> A tabulated list of the applied displacements. The arrows show the direction of movement according to the applied values. ....	60
<b>Table 3.4.</b> A tabulated list of the applied displacements on Asian female model. The arrows show the direction of movement according to the applied values. ....	81
<b>Table 3.5.</b> A tabulated list of the applied displacements on Asian male model. The arrows show the direction of movement according to the applied values.....	84

## LIST OF SYMBOLS AND ABBREVIATIONS

### Symbols

$m$	Meter
$mm$	Millimeter
$\%$	Percentage
$I_i$	Strain Invariants
$\lambda_i$	Principle Stretches
$\Psi$	Isotropic Strain Energy Functions
$J$	Jacobian Ratio
$c_{ij}$	Material Constants
$\sigma$	Stress
$d_i$	Incompressibility Constraints
$\mu$	Shear Modulus
$\alpha_i$	Strain Hardening Exponent
$E$	Young's Modulus

### Abbreviations

$2D$	Two Dimensional
$3D$	Three Dimensional
$CAD$	Computer-aided Design

<i>FE</i>	Finite Element
<i>FR</i>	Forearm at Rest
<i>GOH</i>	Ogden-Holzapfel
<i>GP</i>	General polynomial
<i>IEL</i>	Isometric Extensor Loading
<i>RP</i>	Reduced polynomial
<i>RSTL</i>	Relaxed Skin Tension Lines
<i>VO</i>	Venous Occlusion

Universiti Malaya

# CHAPTER 1

## INTRODUCTION

### 1.1 Background

Most of our body is covered by the skin and it is considered the largest organ with a surface area of 2 m<sup>2</sup>, accounting for about 15% of the body weight (*Naegel et al., 2011; Wentrup-Byrne et al., 2020*). The skin is an impressive organ where it acts as a primary defense against the physical interface and provides protection from harmful environment such as UV light, microbes, pathogens, and chemical and mechanical trauma (*Patria et al., 2019; Yousef et al., 2019*). However, despite its functionality as the first line of defense, it is vulnerable to injury. Regardless of the size of the injuries, any cuts or wounds present on the skin requires immediate surgical procedures to prevent skin infection and scar formation.

The human face represents one's identity and represents one of the most important features in determining physical attractiveness. Any defects, wounds, or tissue loss that disfigures the face would surely affect the person physically and emotionally, thus proper treatment such as facial reconstruction is essential to avoid skin trauma and provide acceptable cosmetic outcomes. One common method of closing the traumatic wound is to perform local flap surgery in which adjacent tissue is repositioned to cover and repair the defect area. The outcome of wound closure depends on the expertise of a surgeon and this requires a profound understanding of skin anatomy, skin biomechanics, and tissue geometry, at which point provides a challenging endeavor for any reconstruction surgeon.

A common problem in local flap surgery is that surgeons depend on their practical experience and expertise to manually measure (Chanda & Upchurch, 2018) and predict skin stress in a clinical setting, yet this approach is still unable to incorporate the skin stress quantitatively (Lee et al., 2019). Moreover, anatomical and geometrical estimation may no longer be feasible considering the availability of accurate pre-operative planning activities that may be employed prior to reconstructive surgery (Molinari et al., 2005). This is where computational simulations come in handy. With significant advancements in engineering and biological technologies, rapid progress in computational models has opened up the possibility to model complex tissues that incorporate nonlinearity, viscoelasticity, and anisotropy (De et al., 2010). Computer simulations that typically rely on the Finite Element (FE) analysis have proven to be a helpful approach in predicting how human skin reacts to physical forces as well as providing an outcome interface of flap reconstructive surgery. There are several commercially available FE software packages, including ANSYS and Abaqus.

A plethora of FE modeling of local flap surgery has been developed by past researchers to better understand the biomechanics of local flaps. These lines of research work often focused on the mechanical movement of the flap upon closing. Such derivation from these simulations leads to optimization techniques and design improvement of the local flap itself. Likewise, the present work aimed at a similar focus with the objectives centered on three different local flaps. The whole concept was to create an inexpensive prototype of computer-assisted surgery that was capable of simulating wound closures on three-dimensional (3D) head templates with a focus on advancement, rotation, and rhomboid flaps.

## **1.2 Problem Statement**

Although FE modeling of facial reconstruction using local flaps has shown remarkable development over a period, none considered a defined approach using a 3D head template. Most of the existing studies focus on two-dimensional (2D) and 3D planar templates in their modeling while neglecting the fact that the relevant structure of the face is practically curved instead of a flat surface. Thus, the present work took the opportunity to address this gap. This can be done by importing 3D scanning head templates into the Computer-aided Design (CAD) realm.

Instead of focusing on standardized models, it is best to associate 3D head templates with various demographics in the FE modeling. It is well-known that the Earth has demographic diversity. Researchers commonly use demographics to define a group of people or societies based on the distinct characteristics of a population. Demographics can be gender, age, nationality, religion, education, ethnicity, and so on. In this study, ethnicity and gender were chosen. 3D head templates representing Caucasian and Asian ethnicities for both male and female genders were obtained from available sources. The diversities in stress distribution upon wound closing across these demographics were analyzed and discussed.

## **1.3 Research Objectives**

FE analysis was fully exploited and 3D head templates were obtained for use to visualize realistic post-operative local flap surgery results. The objectives are specified as follows:

- 1) To demonstrate the possibility of skin flap closures on the 3D head templates using ANSYS Software.
- 2) To describe the stress profiles qualitatively as well as the mechanical movements of advancement, rotation, and rhomboid flaps.
- 3) To explore the sensitivity of the local flaps associated with ethnic and gender groups.

#### **1.4 Novelty of Research**

- 1) 3D head templates were considered to address the gap as 3D face models were uncommonly employed in understanding the biomechanics of the local flaps realistically. Most of the existing studies focus on the 2D and 3D planar geometry in their models.
- 2) As the gender comparison has yet to be addressed, this study is intended to fill this gap by exploring the stress contours of the local flap designs in different genders and ethnicities.
- 3) Create a 3D face model from two opposite genders which is capable of simulating closure of wounds using local flaps with a focus on advancement, rotation and rhomboid flaps.

#### **1.5 Scope of Work**

This work focused on two populations, namely Caucasian and Asian. To enhance the flow of this paper, this research is divided into two case studies where Case Study 1 focuses on the Caucasian model whereas Case Study 2 focuses on the Asian models. The research first approached the Caucasian model as a base study where the results

were analyzed with numerical evidence which in return determines the establishment of the post-operative simulations. Following the validation, the methodology then extrapolated to the Asian models with a focus on gender-related differences. The work involves a straightforward methodology that includes the use of ANSYS software and different types of deformed head templates.

At the preceding stage, this work was spent mostly on establishing numerical models. The local flaps that were involved in this work include advancement, rotation, and rhomboid flaps. The idea was to create a surrogate model that mimicked the exact clinical scenario where a patient lost a part of skin tissue following tumor excision. The work involved preparing the head templates into the CAD realm using ANSYS® Spaceclaim, Release 19.0 software and embedding the local flap designs onto the surface of the templates at three different anatomical locations. The CAD models were then exported into the FE modeling where the program evaluates for stress deformation. The closed-form solutions were performed using ANSYS® Workbench Mechanical™, Release 19.0 software. The simulation was quite straightforward as the solution required only a configured displacement load to maneuver the flap towards the boundary of the defect, yet time-consuming as the convergence required a lot of effort and trials. The concluding phase includes the assessment of the numerical results where the results were compared with existing literature. The position of the maximum stress was used as a benchmark to conclude the validity of the simulations. Following this, the deformation of the local flap designs was evaluated and discussed with a notable remark that the stress values were forecasted with no justified values and solely used to compare the sensitivity of flap deformation on genders.

It was important to underline that the implemented data was mostly extracted from available literature instead of derived from experimental studies. Therefore, the underlying behavioral and geometrical designs were adopted into the modeling after an

in-depth review to ensure that the parameters were compatible and susceptible to failure. This consideration was undertaken due to the complex procedures of approval and lack of expertise in skin biopsy. Nonetheless, this study was monitored strictly and guided by an experienced dermatologist to ensure the surrogate models followed the conventional local flap surgery.

This thesis is arranged in the following manner. Chapter 2 describes the fundamentals of local flap surgery as well as reviews the structure and mechanical behavior of the skin. This insight is essential to understand the primary contributor to skin mechanical behavior. Following this, the constitutive equations used are derived in detail according to the proposed skin behavior. In Chapter 3, the study elaborates the methodology used in modeling the local flap closures. The results were presented in Chapter 4 and then discussed in Chapter 5 where the solutions were analyzed with numerical evidence along with the gender-effect. In closing, Chapter 6 draws the conclusion along with the discussion on the potential methods for refining the simulations in the near future.

## CHAPTER 2

### LITERATURE REVIEW

This chapter reviews the fundamental understanding of local flaps terminology, human skin structure, and skin mechanical properties that may contribute to the development of computerized reconstruction surgery using finite element analysis. From the earliest until recent years, researchers have presented a variety of assumptions and numerical modeling. Human skin is indeed a complex organ and, thus, modeling biological systems in the CAD realm is often explorative, meaning that breakthroughs frequently emerge. Therefore, there is no universal acceptance of human skin modeling. Nevertheless, the constitutive modeling and methodology adopted in the literature are the focus of interest in establishing a realistic surrogate reconstructive surgery at an acceptable computational intricacy.

#### 2.1 Local Flap Surgery

Local flap surgery is a technique that moves a portion of tissue from its original location to its transplanted site with the intent of closing a wound (*Kang, 2017*). Most of the flaps, as opposed to grafts, consist of live tissue as it remains intact with the blood supply. Multiple terms have been used to distinguish the flaps based on the method of transfer (from donor tissue to the recipient). Among the terms that existed (regional, distant, and local flaps), local flaps are considered in this study as the flaps provide variable assessment options and better outcomes (*Jin & Jeong, 2009; Rao & Shende, 2016*). Unlike regional and distant flaps, local flaps derive from freed tissues

immediately adjacent to the open wound where the freed tissues are stretched to fill in the gap.

Local flaps are known to provide an endless amount of flap designs to choose from to cover simple to complex defects that are present in any part of the body. They can be classified into various types of flaps depending on the geometric configuration. These are pivotal flaps (rotation, interpolated, and transposition flaps), advancement flaps (unilateral, bilateral, V-Y, and island flaps), and hinge flaps (Oliaei & Chu, 2013). An illustration of several local flap techniques can be seen in Figure 2.1. The decision on determining which type of local flap should be used for coverage depends on the location and size of the wound. It is the job of the surgeon to choose the least complex type that will achieve the desired cosmetic outcome. Moreover, the effect of reconstruction surgery must be strictly focused on the aesthetic and functional aspects to minimize the visual impact of post-operation such as scars (Hofer & Mureau, 2011).

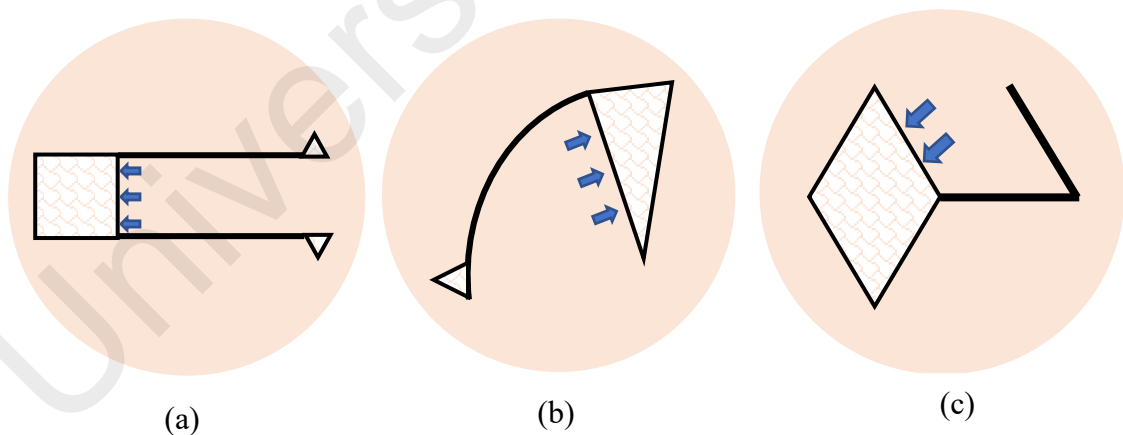


**Figure 2.1.** Local flap techniques (a) advancement flap: moves linearly sliding forward over the underlying tissue (b) rotation flap: rotates about point central to the triangular-shaped wound (c) transposition flap: rectangular flap rotates across the tissue in the wound.

Another important aspect to add when considering better cosmetic results is the placement of flap incisions. It is advisable to position the incision flap lines parallel to the relaxed skin tension lines (RSTL) where the scar would be well-hidden when healed (*Kaufman, 2016*). RSTLs, which are also known as Langer's lines, are illusory lines that are mapped to the face according to the direction of tension in the skin (*Kang, 2017*). These lines can be observed in Figure 2.2 where the skin tension lines are drawn on a diagram of a human face. RSTLs are most visible as rhytides, wrinkles, or furrows where elastic properties are high, though can be less noticeable in certain people, especially in youngsters, in which surgical planning in incision flap designing is required where RSTL would be expected. While most incision flap designs align with RSTL, there are locations where RSTL can be more ambiguous. Specifically, laxity on the temple-forehead junction and central forehead can be determined by pinching the skin, whereas incision flap designs at free margins that include the eyelids, alar rim and lip border are more perpendicular to the margin (*Kaufman, 2016*).

Employing the neighboring skin in the form of a local flap provides long-term longevity due to being similar in color-and texture-matched as well as the dermis and hypodermis remain attached to the body (*Cuddy, 2017*). Satisfaction with the post-operative cosmetic aspect using local flaps was entirely confirmed by *Lee et al. (2017)* with a series of 119 cases in which the patients received facial reconstruction (cheek, nose, temple, lower eyelid, lip, periauricle, forehead, and chin) using Limberg flap and V-Y advancement flaps where the latter scored with a scale of 4.3 out of 5 compared to skin graft surgery. While nasal reconstruction requires a delicate execution and proper selection of flap design, post-operative esthetic results of local flaps were deemed satisfactory in most cases (*Ebrahimi et al., 2016; Losco et al., 2020*). For example, *Salgarelli et al. (2011)* evaluated 203 patients who underwent nasal reconstruction with bilobed, transposition and modified flaps and the majority of the patients reported no

irregular scar. Therefore, providing inconspicuous and less noticeable scars should be the aim for every reconstructive surgeon as these superior cosmetic results would increase the recognition of a surgeon's capability.



**Figure 2.2.** Relaxed skin tension lines (RSTL) are drawn on the diagram of a human face. (Kaufman, 2016)

Common expressions used in local flap reconstruction are listed in Table 2.1 to gain a better insight into the discussion as the chapter advances.

**Table 2.1.** The terminology used in local flap surgery.

<b>Terminology</b>	<b>Description</b>
Defect	Wound or hole
Wound	A part of a body that experiences a loss of tissue.
Primary defect	A wound that is created by trauma or tumor and subsequently closed by a local flap.
Secondary defect	A wound that is created following the primary defect closure (if any).
Incision	The act of cutting or slicing into the body tissues.
Excision	The act of removing a part of body tissue.
<i>In vivo</i>	A procedure that is done on a living subject.
<i>In vitro</i>	A procedure that is done in a laboratory setting within the test tube or Petri dishes boundaries.
Burow's triangle	A triangular skin excision

## **2.2 Surgical Techniques**

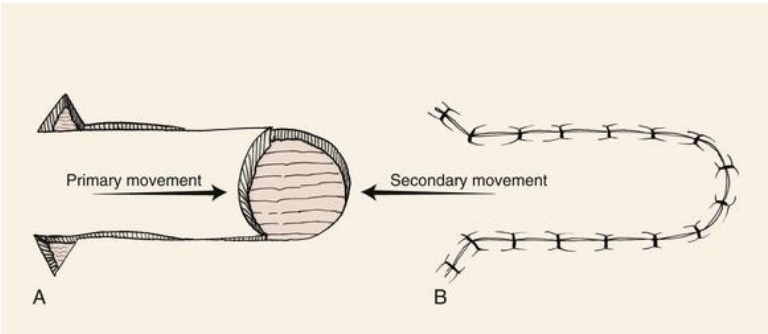
Facial reconstruction is a broad topic, therefore specific areas of focus are selected. Herein, this research focused on advancement, rotation, and rhomboid flaps as these flaps provide versatile options for forehead, cheek, and temple reconstruction. The research considers a situation where a patient was diagnosed with a tumor at a designated facial area and required immediate local flap surgery following tumor excision. The basic techniques of each local flap design are discussed in this section.

### **2.2.1 Advancement flaps**

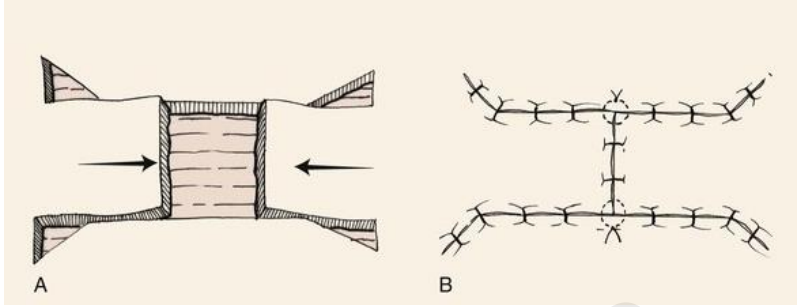
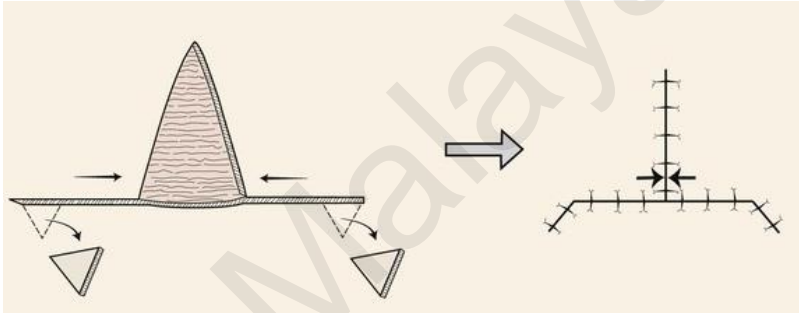
The term “advancement flaps” refers to an incision flap (freed tissue) that undergoes a sliding motion directly to the adjacent wound without any rotational or lateral

movement. There are wide variations of flaps that are listed as advancement flap designs. The basic design of an advancement flap consists of a wound that can be designed in any shape, let it be circular, oval, or rectangular, as long as it matches the width of the tumor (*Dockery, 2012*). Additionally, two parallel incision lines are also created by extending oppositely from the open wound. The width of the incision lines should be adequate to allow some mobility for the flap to advance. According to *Cuddy (2017)*, the author suggested that the incision lines should be equivalent to the width of the wound. Apart from the classic advancement flap, the common modified designs are introduced as single-pedicle, H-plasty, T-plasty, and V-Y or Y-V flaps. Table 2.2 demonstrates geometric configurations and the resulting shapes of each of the advancement flaps. Note that in some cases, although it may not be required, Burow's triangle may be implemented at the tip of the flap to alleviate the tension on the flap itself and also allow more spreading to the freed flap.

**Table 2.2.** Listing of advancement flaps. (*Baker, 2015*)

Advancement Flaps	The Resulting Shapes
Classic	

**Table 2.2.** Continued.

Advancement Flaps	The Resulting Shapes
H-plasty	
T-plasty	
V-Y	

In clinical practice, forehead reconstruction may respond well to advancement flaps. Favorably, the use of these flaps may reduce the possibility of lifting the eyebrows and hairlines and thereby maintain the aesthetic boundaries of the forehead (Kaufman, 2016). Figure 2.3 demonstrates a surgical technique on a forehead using a horizontal advancement flap explained by Turner and Smith (2011). As such, the incision lines were placed within the horizontal rhytids. By doing this, the scar can be

camouflaged by the rhytides. Following the excision of a 3 mm tumor margin, the freed tissue stretches over the underlying tissues as well as the wound to cover the primary defect. Subsequently, the secondary defect closure was done by suturing the incision line to prevent any gap existing which could lead to infection.

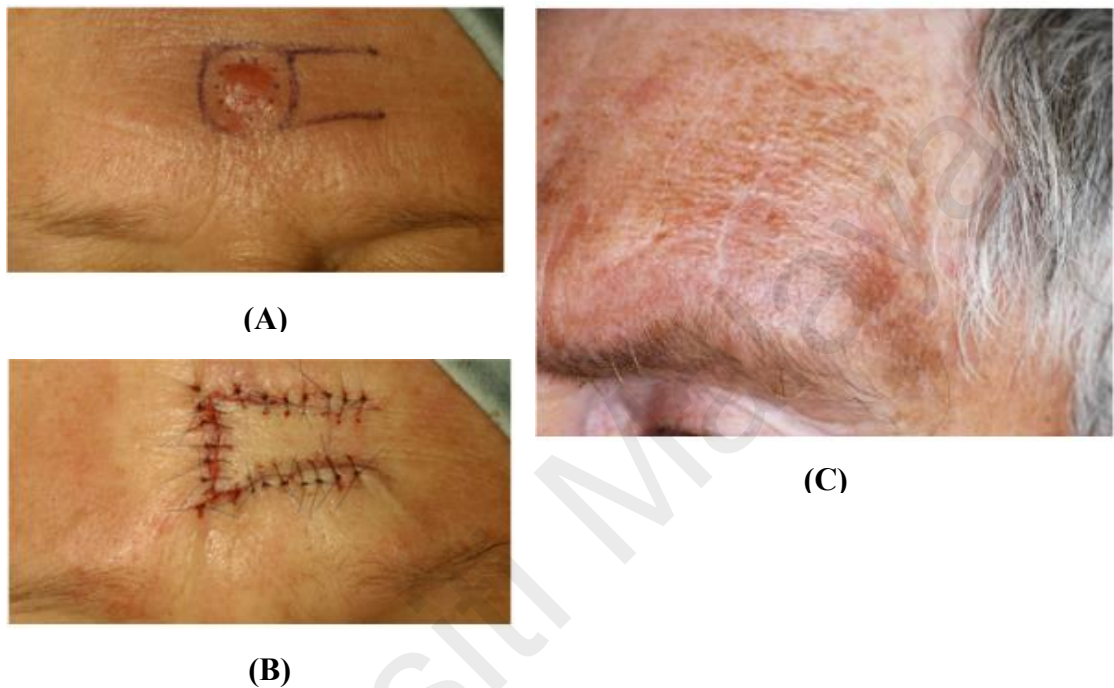


**Figure 2.3.** Classic advancement flap. **(A)** The defect was squared off along with the incision lines drawn adjacent to the forehead rhytides. **(B)** Wound sutured following the excision and reconstruction. **(C)** Post-operative surgery result. *(Turner & Smith, 2011)*

### 2.2.2 Rotation flaps

The term ‘rotation flaps’ refers to an incision flap (freed tissue) that undergoes rotation within a circle about a pivot point towards closing a triangular-or circular-shaped wound. Similar to advancement flaps, rotation flaps can be distributed into variations of designs (Table 2.3). The classic type is often described as a triangular defect with an

ideal height-width ratio of 2:1 as well as the symmetrical arc that extends away from the open wound with the ratio of curve radius to triangular height being 1:2 (Starkman et al., 2017). The length of the arc should be 4 times the width of the triangular defect (Momeni & Souza, 2019; Starkman et al., 2017). This concept leads to a modified rotation flap design to work on the high extremities and adding more rotational components. The modified rotation flaps include Satterfield-Jolly, Catanzariti-Wehman, single-lobed, and double-lobed rotation flaps.

**Table 2.3.** Listing of rotation flaps. (Dockery, 2012)

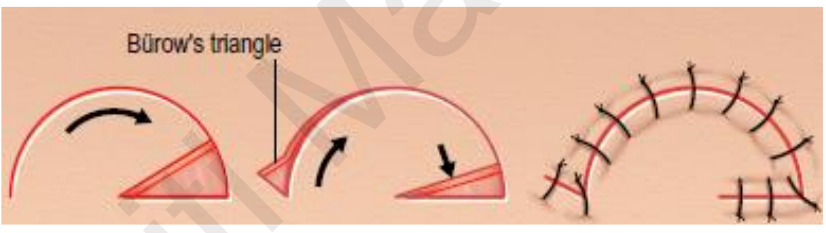
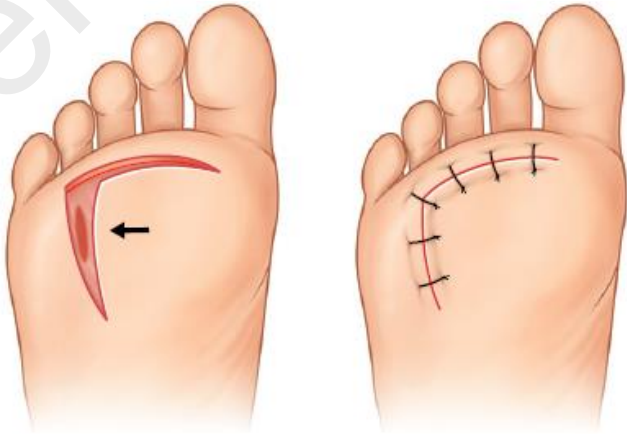
Rotation Flaps	The Resulting Shapes
Classic	
Satterfield-Jolly	

Table 2.3. Continued.

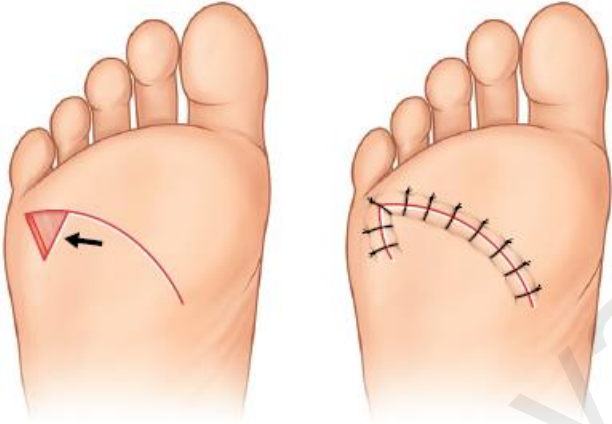
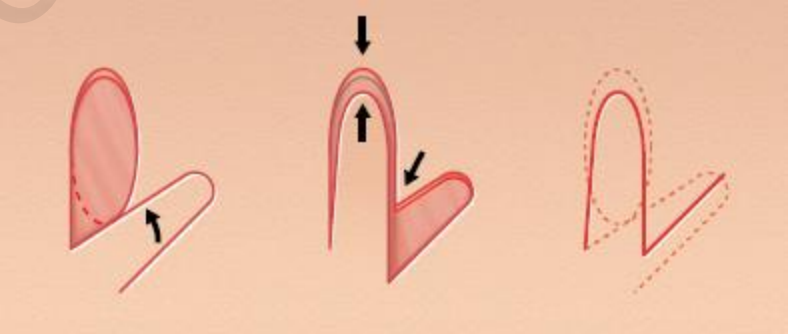
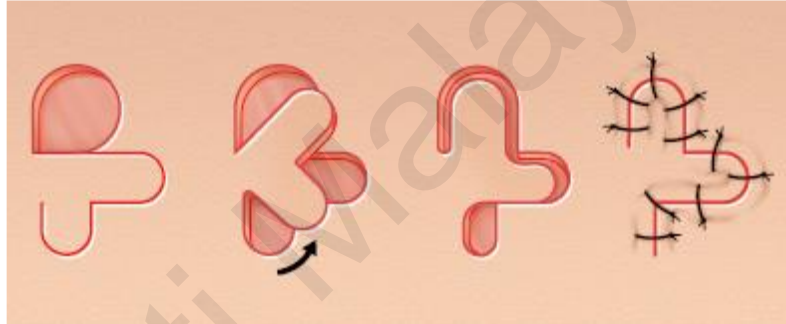
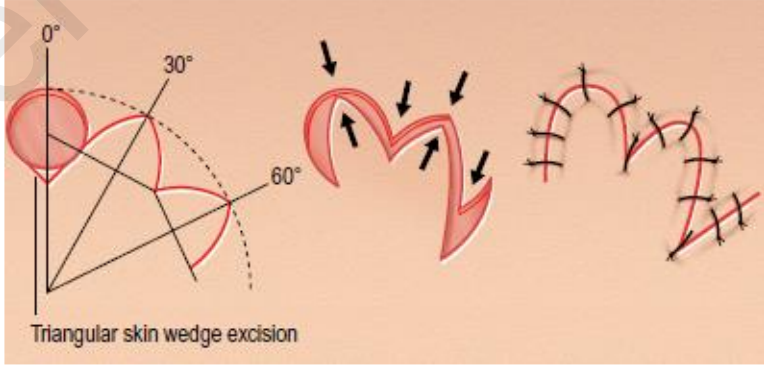
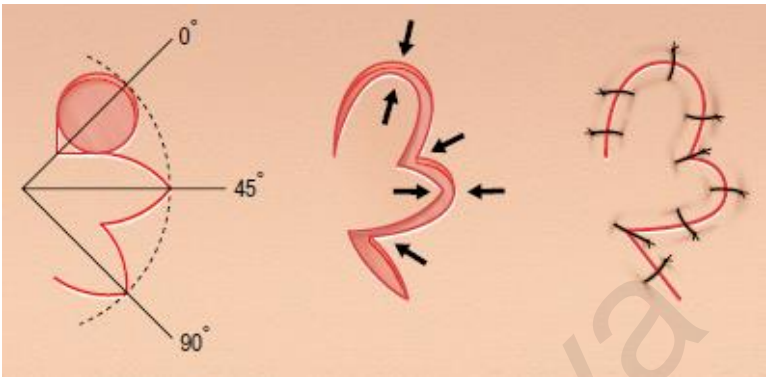
Rotation Flaps	The Resulting Shapes
Catanzariti-Wehman	
Single-lobed	<p>(a) Schrudde Type-1: Original 90° angle to the defect:</p>  <p>(b) Schrudde Type-2: 60° angle to the defect:</p> 

Table 2.3. Continued.

Single-lobed	<p>(c) Schrudde Type-3:</p>  <p>The diagram illustrates the Schrudde Type-3 repair for a single-lobed defect. It shows three stages: 1) A single-lobed defect with a curved flap on the right. 2) The flap is rotated and inset into the defect, with arrows indicating the direction of movement. 3) The final result is a single-lobed defect with a Z-plasty closure, shown as a dashed line.</p>
Double-lobed	<p>(a) The 90° angle between two lobes:</p>  <p>The diagram shows the repair of a double-lobed defect with a 90-degree angle between the lobes. It consists of four stages: 1) A double-lobed defect. 2) A flap is rotated and inset. 3) A Z-plasty closure. 4) A final view showing the sutured closure.</p> <p>(b) The 30° angle between two lobes:</p>  <p>The diagram illustrates the repair of a double-lobed defect with a 30-degree angle between the lobes. It includes a geometric diagram on the left showing the angles (0°, 30°, 60°) and the 'Triangular skin wedge excision'. The main diagram shows three stages: 1) A double-lobed defect with a 30-degree angle. 2) A flap is rotated and inset, with arrows indicating the direction of movement. 3) A Z-plasty closure with suture lines.</p>

**Table 2.3.** Continued.

Rotation Flaps	The Resulting Shapes
Double-lobed	<p>(c) The 45° angle between two lobes:</p> 

In clinical practice, rotation flaps work extremely well in cheek reconstruction to repair a defect that is 3 to 4 cm larger (Heller *et al.*, 2008). Taken from an example by Kaufman (2016), the author performed a classic rotation flap on the lateral cheek after excision of lentigo maligna which can be seen in Figure 2.4. The incision design of the rotation flap was curved upward onto the temple and then travelled downward until it reached the ear lobe. Considering that an oversized rotation arc was implied to counterbalance the undersized flap, the author suggested securing the superior flap first and followed by rotating the remaining flap towards the open wound at which suturing was then take place. This was to ensure unfavorable tension presented at the secondary defect closure. Contrary to the small rotation flap, suturing the primary defect was usually conducted first accompanied by the secondary defect closure.

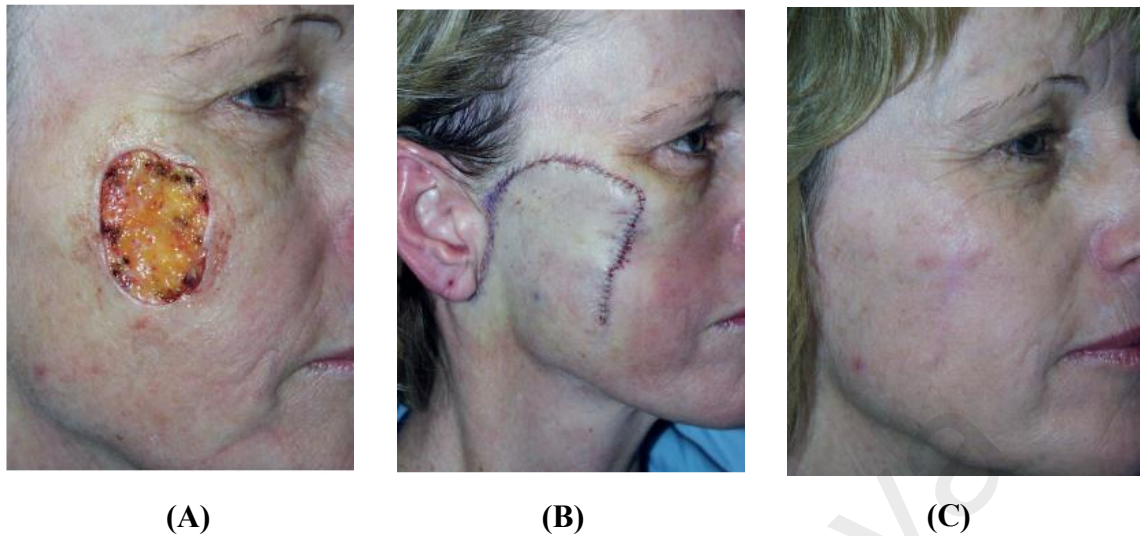


**Figure 2.4.** Classic rotation flap. (A) Circular-shaped wound following the excision of a lentigo maligna. (B) Sutured wound after flap (C) Postoperative surgery result. (Kaufman, 2016)

### 2.2.3 Rhomboid flap

A Rhomboid flap or Limberg flap is a combination of rotation and transposition flap. In contrast to the rotation flap, the transposition flap is often designed as a rectangular-shaped wound and the incised flap (freed flap) rotates over intact tissue at a pivot point towards the primary defect (Momeni & Souza, 2019). Rhomboid flap, as the name implied, is fashioned with an equilateral parallelogram of a rhombic-shaped wound. A typical geometric configuration is shown in Figure 2.5 where the rhombus is designed with  $60^\circ$  acute angle and  $120^\circ$  obtuse angle perpendicular to each other, whereas the incision of the flap is created by extending away from either two of the  $120^\circ$  angles of the rhombus and continuing  $60^\circ$  angle parallel to the first incision line where these two lengths are identical to the width of the rhombus. It is therefore possible to construct

four potential directions of incisions of the flaps in which the flap options are based on the degree of skin laxity and the location of the closure (*Momeni & Souza, 2019*).

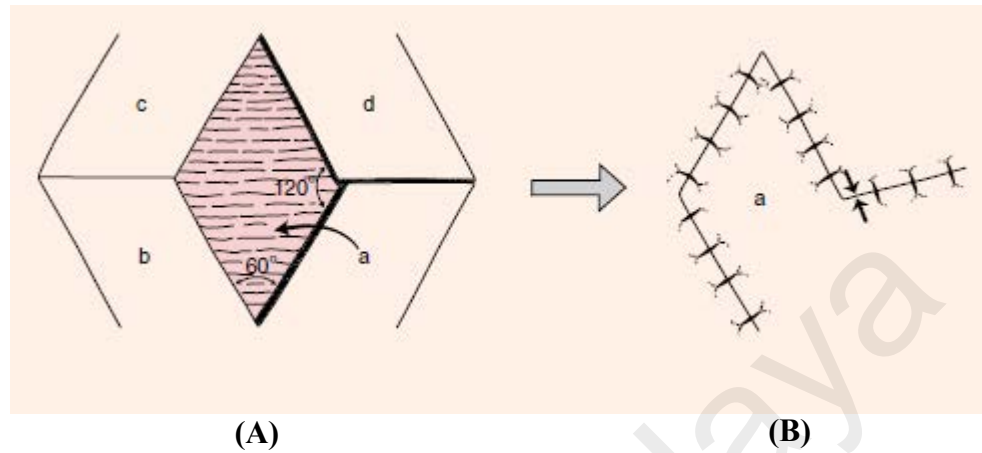


**Figure 2.5.** Classic rhomboid flap. (A) 60° and 120° angles of a rhombus-shaped wound with four possible flap options. (B) The resulting shape and suture of the flap. (*Momeni & Souza, 2019*)

A clinical procedure performed by *Kaufman (2016)* using a classic rhomboid flap to repair a temple defect can be seen in Figure 2.6. Once the incision of the flap was designed, the flap was raised and moved towards the open wound. In closing the wound, the author emphasized suturing the secondary defect followed by the primary defect to enable the flap to transpose into the rhombus-shaped wound. Aside from the standard 60° and 120° angles, the rhomboid flap can be varied into different angles such as Dufourmentel and Webster with the internal angle of the parallelogram, is not limited to 60° and 120° angles.

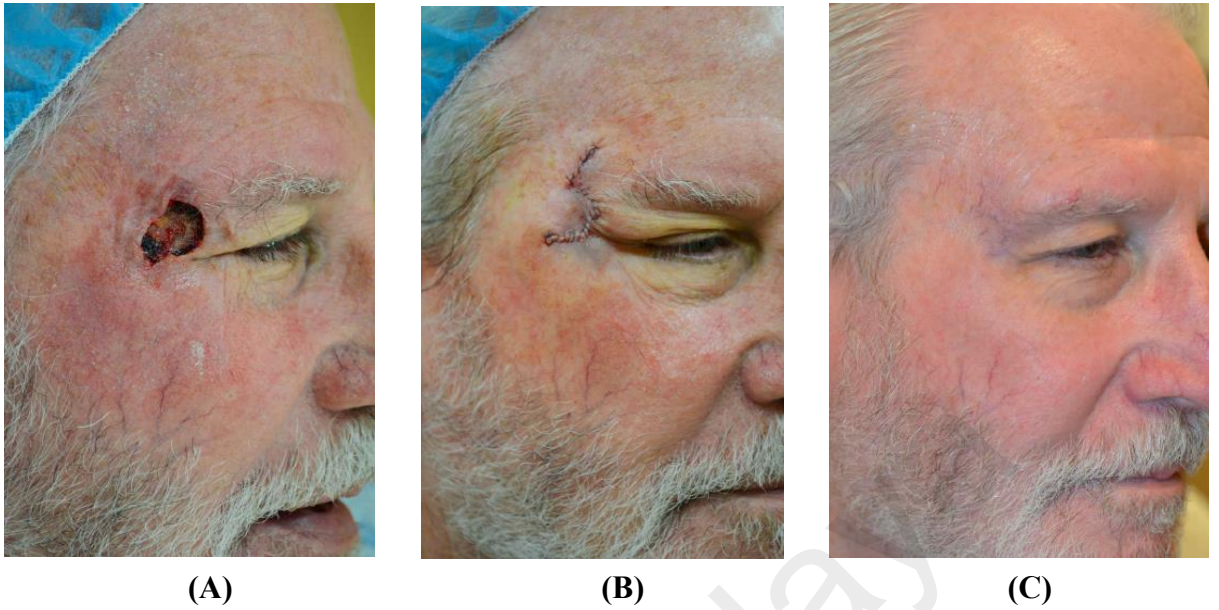


**Figure 2.6.** Classic rhomboid flap. (A) Round-shaped wound adjacent to the eyebrow area. (B) Wound sutured after flap. (C) Postoperative surgery result. (Kaufman, 2016)

## 2.3 Skin Anatomy

### 2.3.1 Components and functions of human skin

Human skin is made up of three basic layers, namely the epidermis, dermis, and subcutaneous tissue (hypodermis), which are held together by connective tissues. Individually, each layer has its own significant role in performing essential body functions and together they are considered as a dynamic system as the tissues work simultaneously as a single structure. Figure 2.7 illustrated the visual structure of human skin and accessory components that existed in each layer.

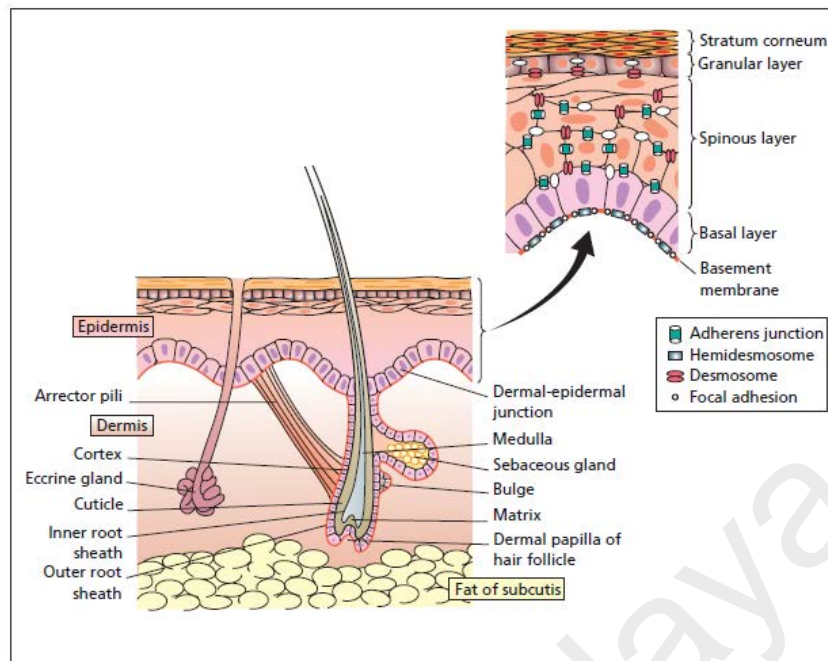


**Figure 2.7.** Architectural representation of human skin and its components (McGrath & J., 2010).

The epidermis, which is the first skin defense layer with the thinnest membrane, typically 0.05 mm (eyelids) to 1.5 mm (palm and soles) (Benítez & Montáns, 2017), is the most superficial surface of the skin. Its primary role includes skin color, pathogen insurance, and tactile sensation. Accessory structures such as hair follicles, glands, and nails are found within this layer. Most of the epidermis is made up of 95% keratinocytes and they are typically formed at the stratum basale (the lowermost epidermis) where mitosis occurs at this stage (Limbert, 2017). Keratinocytes are migrated cells and as the cells transit outwards to the skin surface, the keratinocytes diffuse and slowly become flattened through the keratinization and cellular differentiation process (Massella et al., 2019). This process formed four-division layers, organized from the lowermost epidermis to the superficial surface, called the stratum basale or stratum germinativum, stratum spinosum, stratum granulosum, and stratum corneum (Limbert, 2017).

Beneath the epidermis lies the dermis with thickness varies between 0.6 mm (eyelids) to 3 mm (back palm and soles) (Benítez & Montáns, 2017). These two regions interact with each other in preserving the properties of both tissues. The dermis comprises the bulk of the skin and provides strength and elasticity due to the presence of fibers (mainly collagen) that maintain the turgidity of the skin (Kolarsick et al., 2011). Tough connective tissue, hair follicles, and sweat glands with ducts are mostly found in this layer. Moreover, blood vessels are richly found together with a network of nerve fibers and sensory organs to relay the stimuli responses to the brain. Due to the extensive production of protein and the network of blood vessels, most of the mechanical properties and thermal units are dependent on the dermis (Benítez & Montáns, 2017; Weinzweig & Weinzweig, 2010).

Underneath the dermis lies the subcutaneous tissue, also known as hypodermis, which is the innermost layer of the integumentary system. The thickness of this region varies significantly compared to the upper layers (Groves et al., 2013; Hendriks, 2005). This layer is composed primarily of adipocytes which function as fat storage and thermal insulation. In essence, the fat contained in the subcutaneous tissue provides padding for the body as it protects the bones, muscles, and internal organs from physical damage while regulating the temperature of the body to prevent the body from overheating or cooling.

### 2.3.2 Skin Thicknesses

Understanding the topographic skin thickness is crucial, especially in facial reconstruction as it may guide in resection and restoration. Hence, the determination in determining human skin thickness has been attained through various methods either *in vivo* or *in vitro* in which both have their own advantages and disadvantages. *In vitro* is

usually implemented as a groundwork for future research as this method provides the possibility to alter the skin tissue and be tested until failure (skin tears). However, implementing the *in vitro* method implies that the study acknowledges the tendency to lose the freshness of the tested sample and precision of the measurement. Hence, *in vivo* is better suited for approaching the skin as naturally as possible, although the testing is unable to be pursued at a full range.

*Chopra et al. (2015)* have dedicated their work to comprehensively measuring 39 distinct anatomic locations across the facial region. All the data gathered was based on *in vitro* studies with normalizing factors, noting that the use of cadavers as specimens may not accurately correlate with living skin. Nonetheless, their work had contributed tremendously as they provided a full human facial topographic ‘map’ with epidermis and dermis skin thickness values. Compared to *Pellacani and Seidenari (1999)*, they advocated the use of healthy subjects based on *in vivo* ultrasound technique with a limited study of only 12 facial anatomic locations including age-related variations. They cited a significant increase in skin thickness at all assessed facial anatomic locations, excluding the infraorbital area, of the elderly compared to the youth, which confirmed the effect of age on skin thickness.

While age demonstrated its influence on skin thickness, so does gender. Genetic and hormonal discrepancies play a role as they influence the appearance of skin structure by causing variation between males and females (*Tur, 1997*). Generally, the skin thickness of men is greater than in women in all body regions while subcutaneous fat thickness is thicker in women compared to men (*Igarashi et al., 2007*). Such findings that women’s skin is thinner than men’s can be seen in the work of *Ha et al. (2005)* with a series of 3 cadaver subjects (2 females and 1 male) at 15 facial anatomic locations. Data grouped according to full-thickness, epidermis and dermis, were included and clearly indicated apparent discrepancies between these genders.

Accordingly, *L. Overgaard Olsen et al. (1995)* took a deep observation at 22 body sites with 18 healthy subjects from two sexes using an *in vivo* ultrasound scanner. The authors found similar findings with a notable conclusion that the female has thinner skin than male skin and thinner skin is acoustically denser compared to thicker skin. Figures 2.8 and 2.9 demonstrate the distribution of skin thickness measurement on each investigated anatomical locations according to gender reported from the existing literature.

Even so, a comprehensive analysis of facial skin thickness with a focus on ethnic skin types has been on a small scale. Caucasian subjects overwhelm most of the ethnic skin types used as samples in research, thus the literature on the skin thickness related to Asian subjects is limited. There is no definite conclusion about whether Caucasian skin is thicker than Asian skin or vice versa. However, *Querleux et al. (2009)* managed to extract a set of *in vivo* skin thickness values from four different ethnic groups: African American, Caucasian, Chinese, and Mexican. They found that the thickness of the dorsal and the ventral forearm was more pronounced in Caucasians, whereas the thickness of the cheek region was higher in Chinese, with Caucasians as the lowest. *Laurent et al. (2007)* also performed an *in vivo* measurement at 4 different body regions: thigh, waist, deltoid, and suprascapular. Ethnic differences showed that skin at the thigh and suprascapular areas were thicker in Caucasians, Asian skin was thicker at the waist area and the deltoid area had no significant difference between these two ethnic groups. Figures 2.10 and 2.11 represent the statistics of skin thickness measurement reported from each respective citation.

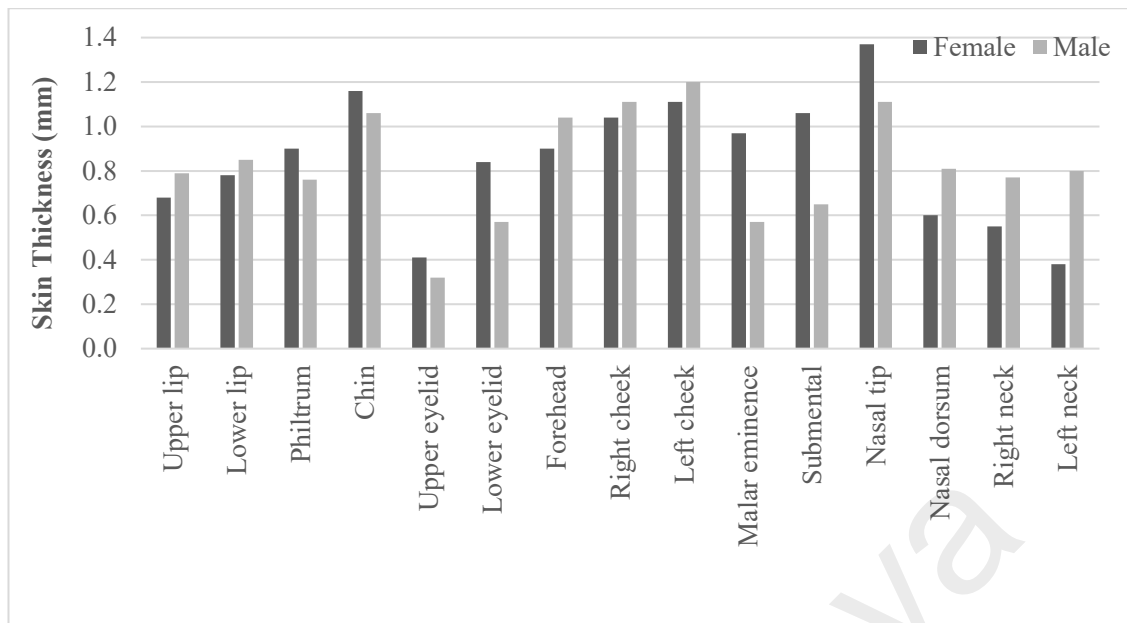


**Figure 2.8.** *In vitro* skin thickness measurement between 82 years old female and 78 years old male cadavers against 15 head anatomical locations. [Reproduced from *Ha et al. (2005)*]

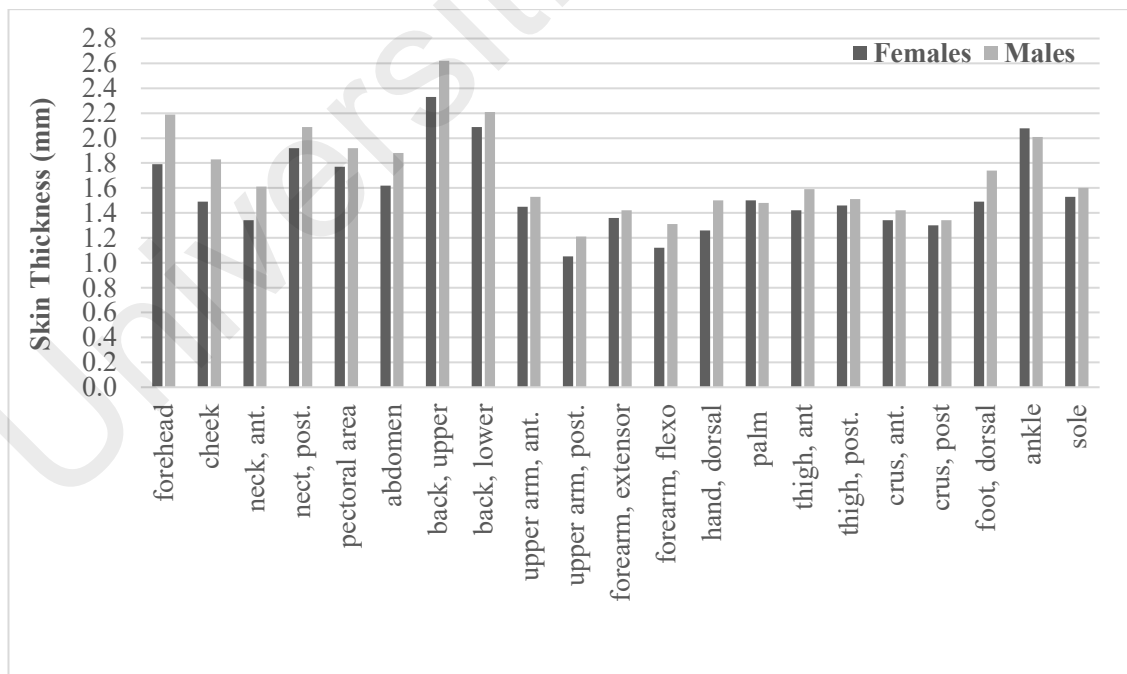


**Figure 2.9.** *In vivo* skin thickness measurement between 10 females and 8 males subjects with a median of 26 years against 21 body sites [Reproduced from *L. Overgaard Olsen et al. (1995)*]

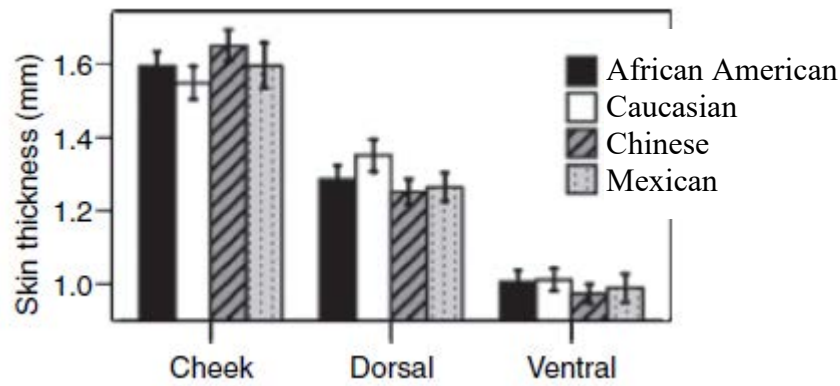


**Figure 2.10.** *In vivo* skin thickness measurement between four different ethnic groups against three body sites (Querleux et al., 2009).

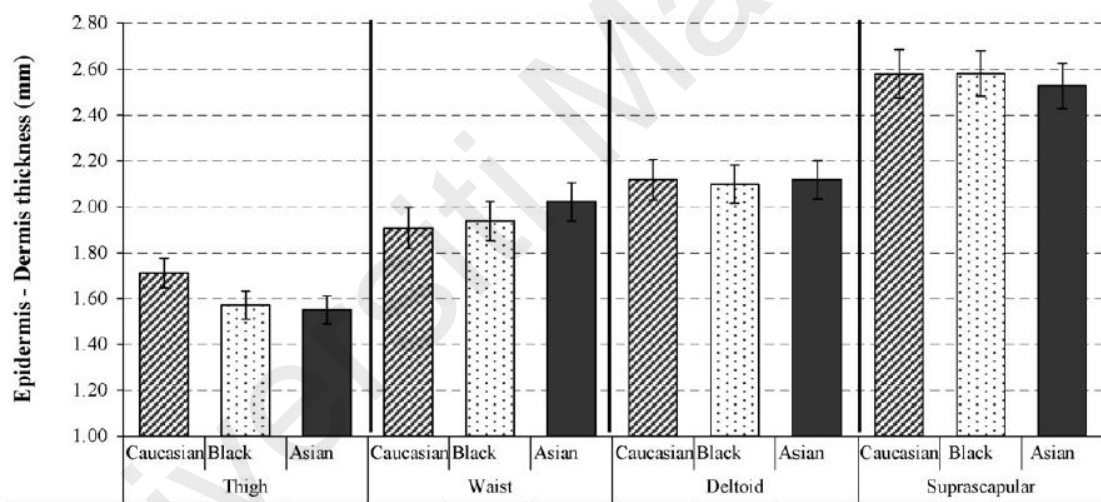


**Figure 2.11.** *In vivo* skin thickness measurement between three different ethnic groups against four body sites (Laurent et al., 2007).

Variations in skin thickness values are inevitable since quantitative modalities used in topographic skin thickness research have improved considerably, although with different foci. This contribution, however, provides a useful clinical context for reconstructive choices in matching the recipient and transplanted sites.

## 2.4 Mechanical Behavior of the Skin

In light of determining the appropriate constitutive model to account for the skin's mechanical properties, it is important to recognize the skin's behavior first. The stress-strain relationship is often used in describing the elastic deformation experienced by the skin when the skin undergoes testing. Skin testing can be performed by two common procedures which are *in vivo* or *in vitro* experiments. Subsequently, the sample or subject undergoes the preferred technique to extract the stress-strain data. These techniques often require an alteration to the skin's shape by either employing a perpendicular load on a small area of the skin (indentation), rotating the skin via an intermediary disk at constant torque (torsion), expanding (tension), or inflating the skin using a partial vacuum in an aperture (suction test) (Kalra *et al.*, 2016).

### 2.4.1 Nonlinear stress-strain relationship

In general, the dermis plays an important role in contributing to the mechanical behavior of the skin (Delalleau *et al.*, 2008). The collagen fibers within the dermis influence the elasticity of the skin, which provides the ability to resume its normal state after being stretched. This permits the competency to model the soft tissue as fiber-reinforced materials since 70% of the weight and 20% of volume in the dermis are mainly composed of collagen fibers (Benítez & Montáns, 2017). Hence, the measured skin properties are frequently attributed to the collagen fibers distribution in the dermis.

The study of the collagen fibers leads to a nonlinear elastic response from the stress-strain relationship. It is done by converting the raw data obtained from the skin testing at a time interval to a stress-strain plot. Under uniaxial tension, the skin tissue behaves in three phases (Figure 2.12). Phase I displays a linear behavior as load

application to skin remains at a low level. As stress increases, the collagen fibers begin to straighten regardless of their resistance to deformation, and thus, nonlinearity is formed in Phase II. In the final Phase III, the crimps disappear and fibers become aligned with the loading direction. The collagen fibers experience fracture after they reach their ultimate strength.

An approach by *Ni Annaidh et al. (2012)* justified the skin stress-strain relationship theory and the three-phase dermis collagen fibers behavior. A stress-stretch curve corresponding to the *in vitro* tensile test of human back skin confirmed the nonlinear response. Apart from the back skin area, *in vitro* tensile test following abdominoplasty conducted by *Lapeer et al. (2011)* illustrated similar responses despite different test areas on the human body. Observation on an *in vivo* uniaxial tension test toward the forearm area by *Barnhill et al. (1984)* also demonstrated nonlinear behavior through the force-strain curve. Hence, the results performed by various researchers clearly revealed that human skin shows a nonlinearity response regardless of age-related, different body regions, or method of testing.

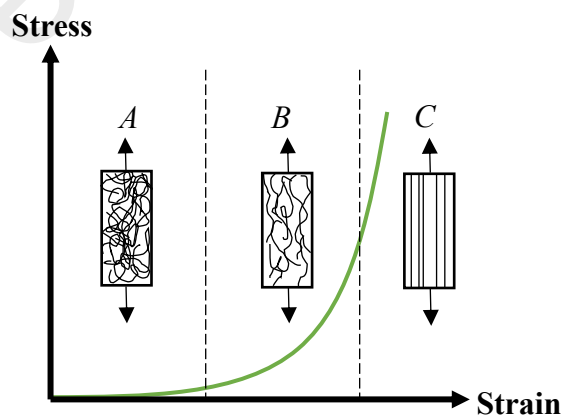


**Figure 2.12.** J-shaped nonlinear response of the skin stress-strain curve due to the corresponding collagen fibers to the direction of the stress. [Redrawn and modified based on *Kalra et al. (2016)*].

#### 2.4.2 Anisotropy and viscoelasticity behavior

The mechanical response of human skin tissue to external forces is known to be influenced by anisotropic and viscoelastic properties. This theory is agreed by numerous researchers through observation and evaluation that are done experimentally. These two effects can be observed by experimental tests involving mechanical testing on skin tissue at different lengths and directions.

Anisotropic properties address the variation in the distribution of the collagen fibers that are much related to the natural lines of tension that appear on the skin (*Chanda & Callaway, 2018*). The overall effects reflect the skin stress-strain curve described from the study of the collagen fibers through varying the loads and the orientation of collagen fibers (*Chanda & Callaway, 2018; Ni Annaidh et al., 2012*). For reconstructive surgeons, understanding the anisotropic behavior is important as the arrangement of incision lines according to the orientation of collagen fibers influences the scar formation. Viscoelastic properties, on the other hand, are observed as a combination of viscous and elastic characteristics under deformation where the material properties show a time-dependent behavior. The effect can be observed through the investigation of stress relaxation (*Liu & Yeung, 2008*) and creep (*Jee & Komvopoulos, 2014; Lin & Lin, 2021*). The basic response of the viscoelastic effect shows that stress relaxation occurs when stress decreases with time under constant strain, whereas creep occurs when strain decreases with time under constant stress.

From those views, several past models have incorporated these effects to characterize the skin. However, the complexity of the skin's mechanical properties is still under study. This is due to the wide variability of skin behavior that depends on the location of the body and individuality. *Joodaki and Panzer (2018)* have stated the importance of incorporating viscoelasticity in skin modeling, yet *Wong et al. (2016)*

questioned the effect of anisotropic and viscoelastic on the skin mechanical properties as the interaction was unclear. Nevertheless, exploring the role of anisotropic and viscoelasticity in the studies of skin tissue may contribute to a considerable extent in medical diagnosis, surgical simulation and planning, and skin deformation.

## 2.5 Skin Constitutive Modeling

Choosing an appropriate constitutive model to account for skin mechanical behavior is an essential step in computer simulations. Linear-elastic and hyper-elastic materials are often adopted as material properties in most of the skin's constitutive modeling. However, these materials have their own features when related to the stress-strain relationship. Thus, the rationality between these two materials to nonlinearity responses will be discussed accordingly.

### 2.5.1 Linear-elastic modeling

Linear-elasticity is the simplest form of material model that assumes a linear relationship between stress and strain under a small strain deformation. This linear relationship defines the general Hooke's law and the proportionality factor represents the properties of a material called Young's modulus (*Pawlaczyk et al., 2013*). In simple terms, Young's modulus is the Hooke's law constant. Skin stiffness has been associated with Young's modulus by the earliest studies to characterize the human skin. It is commonly used as a straightforward constitutive model that can provide a rough estimation of the skin tissue's responses to external loading. Table 2.4 shows the summary of the reported Young's modulus measurement (denoted as  $E$ ) through *in vivo* and *in vitro* skin testing found in the existing literature.

Several researchers viewed linear material as incompatible with imitating the actual human skin behavior. *Chanda and Unnikrishnan (2017)* emphasized that Young's modulus and Poisson's ratio were insufficient to represent soft materials. *Joodaki and Panzer (2018)* also stated in their review that incorporating linear-elastic modelling was inadequate to illustrate the nonlinearity, viscoelasticity, and soft tissue's loading history. *Delalleau et al. (2008)* at first believed that Hooke's law was not suitable to characterize human skin behavior. They eventually found that incorporating the Total and Updated Lagrangian formulations into Hooke's law could account for the large strains and displacements problems where the outcome found a good correlation with the standard Hooke's laws. When compared to the skin's stress-strain curve, the linear region at the initial and final phases are defined by Hooke's law where the linear slope is Young's modulus. This leaves uncertainty to the second phase whether the nonlinear region can be represented by Young's modulus. As stated by *Lapeer et al. (2011)*, Young's modulus can be acceptable if it was used at the lowest and the highest modulus range only. Nevertheless, *Retel et al. (2001)* and *Kirby et al. (1998)* insisted that Young's modulus could be adopted as skin's material properties if the shear modulus was included to represent the nonlinear region.

**Table 2.4.** Summary of several works of literature on the skin's Young's modulus measurement. FR: forearm at rest, IFL: isometric flexor loading, IEL: isometric extensor loading, VO: venous occlusion.

<b>Tension skin testing</b>	<b>E (MPa)</b>	<b>Langer lines</b>	<b>Test specimen</b>	<b>Method</b>
<i>Ni Annaidh et al. (2012)</i>	83.33 ± 34.9	n/a	Back	<i>In vitro</i>
<i>Ottenio et al. (2015)</i>	160.8 ± 53.2	Parallel	Back	<i>In vitro</i>
	70.6 ± 59.5	Perpendicular	Back	<i>In vivo</i>
<b>Suction skin testing</b>	<b>E (kPa)</b>	<b>Thickness (mm)</b>	<b>Test specimen</b>	<b>Method</b>
<i>Hendriks et al. (2003)</i>	56.4 ± 21.6	1.35	Volar forearm	<i>In vivo</i>
<i>Delalleau et al. (2008)</i>	131	0.86	Volar forearm	<i>In vivo</i>
	64	1.08	Volar forearm	<i>In vivo</i>
	41	1.51	Volar forearm	<i>In vivo</i>
<b>Indentation skin testing</b>	<b>E (kPa)</b>	<b>Probe size (µm)</b>	<b>Test specimen</b>	<b>Method</b>
<i>Zahouani et al. (2009)</i>	8.3 ± 2.1	1000	Volar forearm	<i>In vivo</i>
<i>Livarinen et al. (2011)</i>	210	2000	FR	<i>In vivo</i>
	446	2000	IFL	<i>In vivo</i>
	651	2000	IEL	<i>In vivo</i>
	254	2000	VO	<i>In vivo</i>

### 2.5.2 Hyper-elastic modeling

The term 'hyper' defines something that is excessive or beyond normal. Therefore, hyper-elasticity refers to a material that has high elastic behavior such as rubbers, polymers, elastomers, and biological tissue materials. Hyper-elastic materials use strain energy functions (denoted as  $\Psi$ ) to derive the stress-strain curve where the relationship between stress and strain is nonlinear under large deformation (*Shahzad et al., 2015*).

The most interesting property of hyper-elasticity is that it provides a means for the materials to model isotropic or anisotropic, incompressible, and viscoelasticity behaviors. A hyper-elastic model presumes its form from the derivation of the general form of the strain energy function based on three stress invariants  $I_1$ ,  $I_2$ , and  $I_3$ . The derivation eventually opens up a path to a wide range of hyper-elastic models to choose from, all depending on the expected range of strains, dependencies, and data sets to define a particular stress-strain relationship. Neo-Hookean and Mooney-Rivlin models were the first to be introduced as hyper-elastic models in 1948 and 1952 respectively and then followed by Veronda-Westmann (1970), Humphrey, Martins, Ogden (1972) Yeoh (1993) models, and so on (Martins *et al.*, 2006; Shahzad *et al.*, 2015). The strain energy functions of four main hyper-elastic models can be seen in Table 2.5.

**Table 2.5.** Four commonly used hyper-elastic models.  $c_{ij}$  = material constant,  $\mu$  = shear modulus,  $\lambda_i$  = principle stretch and  $\alpha_i$  = strain hardening exponent.

Hyper-elastic models	Strain energy functions, $\Psi$
Neo-Hookean	$\Psi = c_1(I_1 - 3)$ <p>where <math>c_1 = \frac{\mu}{2}</math></p>
Mooney-Rivlin	$\Psi = c_1(I_1 - 3) + c_2(I_2 - 3)$ <p>where <math>c_1 = \frac{\mu_1}{2}</math> and <math>c_2 = \frac{-\mu_2}{2}</math></p>
Ogden	$\Psi = \sum_{i=1}^n \frac{\mu_i}{\alpha_i} (\lambda_1^{\alpha_i} + \lambda_2^{\alpha_i} + \lambda_3^{\alpha_i} - 3)$
Yeoh	$\Psi = \sum_{i=1}^3 c_{i0}(I_1 - 3)^i$

The modeling of hyper-elastic materials comprises the selection of an appropriate strain energy function that describes a close fit to the measured curve and determination of the referred material constants,  $c_{ij}$ . This process can be determined by curve fitting where a data set of stress-strain relationships obtained from the experiment is input into the FE method and subsequently generates stress-strain curves depending on the referred strain energy functions. The interesting part of the FE method is that the software provides a convenient approach to compare different stress-strain curves of hyper-elastic models to the measured curve. *Shahzad et al. (2015)* conducted a comprehensive stress-strain relationship study of seven hyper-elastic models and compared them to the natural rubber's experiment data. The Yeoh model was found to provide the best fit to match the natural rubber's stress-strain curves at small and large strain values from four deformation tests.

As such, the application of hyper-elastic models to soft-biological tissues has received attention from the most recent researchers. This is due to the similarity found between both of the stress-strain curves. It can be seen from the work of *Gasson et al. (2008)* where they fitted three different hyper-elastic models (general polynomial (GP), reduced polynomial (RP), and Ogden) using raw data produced from an *in vitro* uniaxial tensile experiment on human skin and discovered an RP material such as first-term Neo-Hookean and third-term Yeoh models produced the most favorable result towards human skin behavior. Owing to that, most of the researchers who pioneered in biomechanics recommended adopting the human skin as a hyper-elastic material rather than as a linear material.

## 2.6 Deriving Constitutive Model Equation

Human skin is known to exhibit nonlinear anisotropic, viscoelastic, and incompressible mechanical properties (Delalleau et al., 2008; Lapeer et al., 2011). However, to describe anisotropic and viscoelastic behavior into a whole model would be complicated and time-consuming (Mahmud et al., 2012). This is due to the complex computational algorithm presented by the anisotropic properties where the behavior demands multiple directional variables (Cheng & Zhang, 2018) whereas the ignorance of viscoelastic effect is due to its strong interaction with the anisotropic properties (Benítez & Montáns, 2017). Thus, nonlinear isotropic was considered to simplify the correlation of the constitutive model equations with those experimental tests and reduce computational time.

It was concluded that the present work decided to implement hyper-elastic models as skin material properties due to their similar response to the skin stress-strain curve. Among the existence of hyper-elastic constitutive models, the Yeoh model was particularly chosen to characterize the nonlinear skin mechanical behaviour as this model was found fit and stable during the material fitting process from the uniaxial tensile experiment instead of the Ogden and GP hyper-elastic model (Gasson et al., 2008; Lapeer et al., 2011). Of note, this study focused on incompressible hyper-elastic material via uniaxial tension tests and the equations presented below incorporated with the mentioned approaches. The isotropic strain energy functions,  $\Psi$  is dependent upon the right Cauchy-Green tensor or strain invariants ( $I_1, I_2, I_3$ ) and principle stretches ( $\lambda_1, \lambda_2, \lambda_3$ ) (Martins et al., 2006) where  $\Psi$  is described as

$$\Psi_{isotropic} = \Psi (I_1, I_2, I_3) \quad (1)$$

where

$$I_1 = \sum_{i=1}^3 \lambda_i^2 \quad , \quad I_2 = \sum_{i,j=1}^3 \lambda_i^2 \lambda_j^2 \quad (i \neq j) \quad , \quad I_3 = \prod_{i=1}^3 \lambda_i^2 \quad (2)$$

An interesting particularity of this model is that the Yeoh model is a polynomial of the first invariant,  $I_1$  in which  $I_2$  and  $I_3$  are ignored (Cheng & Zhang, 2018). Thus,  $I_1$  take the form of

$$I_1 = \lambda_1^2 + \lambda_2^2 + \lambda_3^2 \quad (3)$$

For hyper-elastic materials subjected to uniaxial tension, the principal stretches are expressed as  $\lambda_1 = \lambda$  and  $\lambda_2 = \lambda_3$  whereas the incompressibility condition, denoted as  $J$  (also known as Jacobian) implies that

$$J = \prod_{i=1}^3 \lambda_i = 1 \quad \text{or} \quad J = \lambda_1 \lambda_2 \lambda_3 = 1 \quad (4)$$

By accommodating the constraints of  $\lambda_1 = \lambda$  and  $\lambda_2 = \lambda_3$  into Equation (4),

$$\begin{aligned} \lambda_1 \lambda_2 \lambda_3 &= 1 & \text{and} & & \lambda_1 \lambda_2 \lambda_3 &= 1 \\ \lambda \lambda_2 \lambda_2 &= 1 & & & \lambda \lambda_2 \lambda_3 &= 1 \\ \lambda_2^2 &= \frac{1}{\lambda} & & & \lambda_3^2 &= \frac{1}{\lambda} \end{aligned} \quad (5)$$

It can be concluded that,

$$\lambda_2^2 = \lambda_3^2 = \frac{1}{\lambda} \quad (6)$$

and substituting Equation (6) into Equation (3), the  $I_1$  variant achieved another form of

$$I_1 = \lambda^2 + \frac{2}{\lambda} \quad (7)$$

Taken from *Martins et al. (2006)*, the isotropic strain energy for the Yeoh model along with the incompressible condition is given by

$$\Psi_{Yeoh} = \sum_{i=1}^3 c_{i0} (I_1 - 3)^i \quad (8)$$

By expanding the above equation and then substitute Equation (7), it becomes

$$\Psi_{Yeoh} = c_{10} \left( \lambda^2 + \frac{2}{\lambda} - 3 \right) + c_{20} \left( \lambda^2 + \frac{2}{\lambda} - 3 \right)^2 + c_{30} \left( \lambda^2 + \frac{2}{\lambda} - 3 \right)^3 \quad (9)$$

The next step is to express the strain energy function in terms of principal Cauchy stress.

For the Yeoh model, its stress may take in the form of

$$\sigma = \lambda \frac{\partial \Psi}{\partial \lambda} \quad (10)$$

and by solving the equation,

$$\sigma_{Yeoh} = \lambda \left( \left( 2\lambda - \frac{2}{\lambda^2} \right) \left( c_{10} + 2c_{20} \left( \lambda^2 + \frac{2}{\lambda} - 3 \right) + 3c_{30} \left( \lambda^2 + \frac{2}{\lambda} - 3 \right)^2 \right) \right)$$

$$\sigma_{Yeoh} = \lambda \left( \left( 2\lambda - \frac{2}{\lambda^2} \right) (c_{10} + 2c_{20}(I_1 - 3) + 3c_{30}(I_1 - 3)^2) \right) \quad (11)$$

the strain energy function of the Yeoh model finally is expressed as

$$\sigma_{Yeoh} = 2 \left( \lambda^2 - \frac{1}{\lambda} \right) (c_{10} + 2c_{20}(I_1 - 3) + 3c_{30}(I_1 - 3)^2) \quad (12)$$

where  $c_{10}$ ,  $c_{20}$ , and  $c_{30}$  are defined as material constants and they are determined by curve fitting.

## 2.7 Wound Closure Simulation

Scientific interest in biomechanical modeling of human skin is not recent. Computational models that behave similarly to the human skin have an added value to the surgical planning. Computer simulations that typically rely on the FE analysis have proven to be a helpful approach in predicting how human skin reacts to physical forces as well as providing an outcome interface of flap reconstructive surgery. Among the existing literature, *Retel et al. (2001)* developed a 2D nonlinear model of Limberg and diamond-shaped incisions with the intent of determining the stress fields around the wounded skin along with resultant closure force. Orthotropic hyper-elastic and pre-stress conditions were included to characterize the skin. Apart from them, *Flynn (2010)* tried to find the force required in closing four types of excision shapes, namely the

circular, elliptical, fusiform, and lazy S-plasty. They used Young's modulus, shear modulus, and Poisson ratio as their choice of skin material. Such derivation from these findings will reduce the adverse stress profiles and minimize scarring.

Other upsides are the optimization techniques and design improvement of local flap design. The proposed designs could lead to better wound closure effectiveness with a focus on improving the size of incisions to avoid dog-ear formation. In particular, *Lovald et al. (2013)* and *Topp et al. (2014)* studied monopedicle and rhombic transposition flaps respectively and both of them discussed the ideal cutting patterns from variations of geometric flap patterns. The second order of the Yeoh hyper-elastic model along with nonlinear, incompressible, and isotropic assumptions was fitted as material properties of skin in their 2D planar model. Meanwhile, *Rajabi et al. (2015)* suggested implementing a rhombic flap pattern similar to Z-plasty results in the envisaged result. A second-order Ogden hyper-elastic was added as skin material properties.

*Chanda and Unnikrishnan (2017)* claimed that 2D model analyses provided limitations in surgery planning as well as clinical training. They believed that a realistic 3D computational study addressed the limitation. Hence, they developed a 3D analytical model of a two-layered diamond-shaped wound using interrupted sutures to close the wound. Third-order Yeoh hyper-elastic material models were adopted with the presence of skin prestress. *Tepole et al. (2014)*, on the other hand, explored the stress profiles of direct advancement flaps and double back-cut flaps. Their simulations captured the relationship between the maximum stress areas and tissue necrosis. Meanwhile, *Lee et al. (2019)* dealt with three local flap designs, namely advancement, transposition, and rotation flaps, and explored the flaps sensitivity in two different age groups. 3D planar models were developed in which each incision design was embedded and the Gasser-Ogden-Holzapfel (GOH) material properties were employed. Their results showed that

the elder group responded more sensitively to the flap deformation compared to the younger group.

Overall, earlier developments in this field used a vast array of assumptions, including different skin material, skin thickness and mechanical properties. As such, some of these assumptions adopted material parameters from the literature while others derived from experiments. Nevertheless, despite having countless proposals in computational studies, after an in-depth review, it can be concluded that all of these past attempts pursue identical methodology.

## 2.8 Summary of Literature Survey

Biomechanics studies on local flap surgery have been well-researched. The impact of this research line to the medical application has been well underlined and acknowledged. All of the past attempts including various used of techniques (indentation, tension, tensile or suction test), procedures (*in vitro* or *in vivo*), numerical modeling method (2D or 3D) and constitutive model (linear or hyperelastic) have been summarized and deeply reviewed to carefully reproduce the computational modeling with the identified gaps found in the literature.

Throughout the literature review, this study identified 3D modelling approach and demographics comparison as the two main gaps that has not been explored. Although initial work using 2D and 3D planar have been much contributed to the knowledge in this field, this study realized that 3D head structure would give more insight to the wound closure mechanism as 2D approaches were believed to be within their limits from pragmatic approach (*Chanda & Unnikrishnan, 2017*). Apart from this, analysis of demographics comparison in this field has been on a small scale. Majority of the past attempts focused on a single sample, yet different objectives. Therefore, this study has

considered to provide extensive research of the wound closure effect on different facial structure that focused on gender (female and male) and ethnicity (Caucasian and Asian) with a hope that this knowledge can provide aids in patient applications, especially in diagnosing and assessing the addressed treatment.

Overall, local flap surgery based on the finite element method should be dealt with effectively in order to achieve a promising result and meet the objectives successfully. Several of the techniques presented by the past researchers were manageable and adoptable for this study. In other words, these studies in the literature can still be referred to in spite of having minor similarity in terms of the work done between the current study and the existing literature. Of note, the whole concept of this study was to create an inexpensive computer-assisted surgery that is capable of simulating wound closure on three different wound patterns using 3D head templates of the Caucasian male, Asian female and Asian male. As such, limitations and assumptions used for this study are discussed in the following chapters.

## CHAPTER 3

### METHODOLOGY

This chapter elaborates on all research methodologies used for all cases. The research is divided into two focused case studies where Case Study 1 focuses on the effect of wound closure on the Caucasian head template while Case Study 2 focuses on the effect of wound closure on Asian head templates, both cases using three different techniques. These techniques involved the use of local flaps in which each of the local flaps has its own design and method of movement to cover the excised area. The idea was to deliver a CAD model of a human face that had a hole in the shape that mimicked the design of a local flap and was able to reproduce a reconstructive phenomenon. Boundaries were established to eliminate complications as well as to reduce computational time. Moreover, the 3D procedures were run through many trials of load inputs until the hole was completely covered. The final solutions were expected to illustrate a realistic virtual post-operative of reconstructive surgery.

#### **3.1 Case Study 1: Caucasian Model**

The FE modeling for Case Study 1 involved the creation of surrogate surgery models, based on the Caucasian population. The methodology in Figure 3.1 represents a complete process for one flap closure where the procedures will be repeated for the next local flap designs.

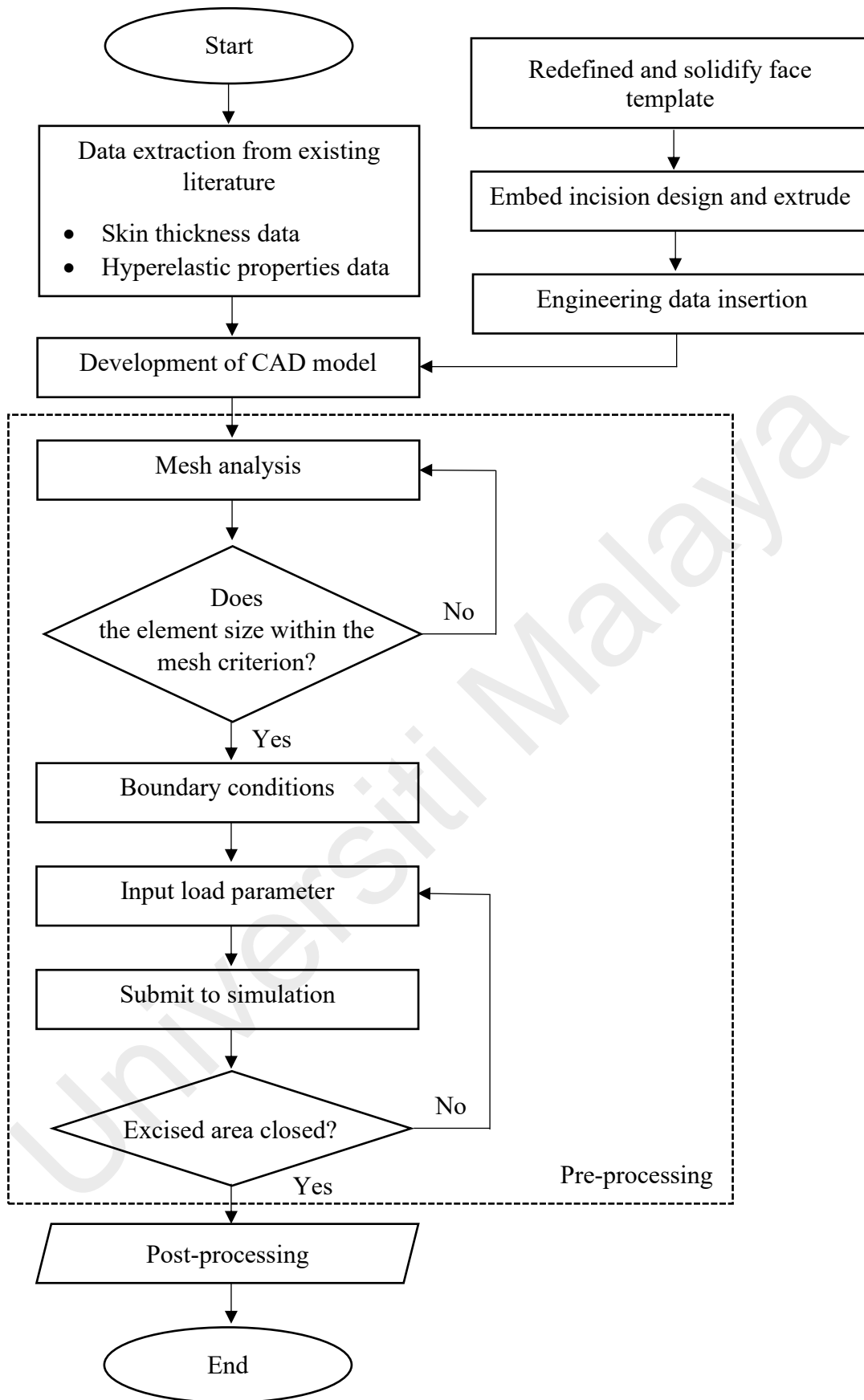


**Figure 3.1.** The methodology used in designing a 3D wound closure.

Research began by gathering data values from the existing literature that were needed to characterize the model's properties into the obtained 3D head template. Skin thickness and hyper-elastic properties were the two main data that were crucially important to replicating the underlying behavioral properties of human skin. These data were carefully selected with the consideration that was listed in the literature review. The next step was the development of a 3D wound closure using CAD tools. Prior to that, a base model was needed to create defects of varying shapes on different sites. This was done using ANSYS® Spaceclaim, Release 19.0. The best possibility to obtain the head template was from an open-source website where a wide variety of 3D head templates were readily available to choose from. However, obtaining a free template required a small effort so that its quality was at its highest before proceeding to the next step.

After redefining the mesh body of the head template and thickening the model, it was time to create a deformed part on the face model. The deformity was formed by designing a local flap onto the surface of the face model and extrude cut entirely. Following this, the deformed model was then transferred to Structural Analysis from ANSYS® Workbench Mechanical™, Release 19.0 where the Engineering Data module was accessed to define the material properties. Subsequently, mesh generation was executed in the Model module to improve the FE analysis model. A number of decisions were required to be made to ensure the accuracy of the mesh. These decisions were assessed based on mesh shapes, mesh criterion, and number of elements, thus a number of running trials of mesh size were performed until the anticipated mesh size was found. Boundary conditions and loads were then applied to the model before submitting it for simulations.

At this point of the workflow, the goal of closing the defect was quite challenging and time-consuming as numerous trials of load input were performed until the results

converged. The procedures were repeated for the following 3D deformed face model using other local flap designs. Final solutions of post-operative simulations using three local flap designs were gathered and analyzed. The current and existing results were compared by evaluating the stress profiles of three different reconstructive scenarios to assess the accuracy and effectiveness of the present work, which may alternatively help to refine for future visual reconstructive planning.

### 3.1.1 Face model

A standardized 3D head template of a Caucasian was obtained for use. A Caucasian male head template acquired through an open-source platform (*Mad Mouse Design, 2007*) and the dimension of the head template was described in a bounding box of 306 x 354 x 382 mm. Since the template originated from a rendered graphic, it was in the form of meshes where the body was covered with small discrete cells or faces. A mesh body is said to be efficient if it is a structured grid with quadrilateral cells in 2D and hexahedra cells in 3D. The head template contained quadrilateral-shaped cells and was already considered as a structured grid. However, it was untextured and had low face counts as seen in Figure 3.2. Modifications were done by filling the existing holes and redefined the density of faces as shown in Figure 3.3. Subsequently, half of the head template was excluded, starting from the ears to the back of the head, to avoid complications following the conversion to a 3D state.

Thickness was then applied to accommodate the realization of an actual human face. Three facial anatomic locations, namely forehead, cheek, and temple were considered. It should be emphasized that the ANSYS software provides a limitation in implying multiple thicknesses in one model. Due to this constraint, three modified head templates were prepared where each of them was thickened relative to the mentioned

anatomic locations (later referred to as “face model”). Moreover, only a single layer was considered in the modeling process with the thickness of this layer comprising the combined epidermis and dermis thickness in order to minimize the complexity of the numerical simulation. The epidermal and dermis thicknesses were readily available from existing literature (*Chopra et al., 2015*). Noted that the available data was based on biopsy (*in vitro*) findings using cadaveric Caucasian samples. The values of the thicknesses are given in Table 3.1.

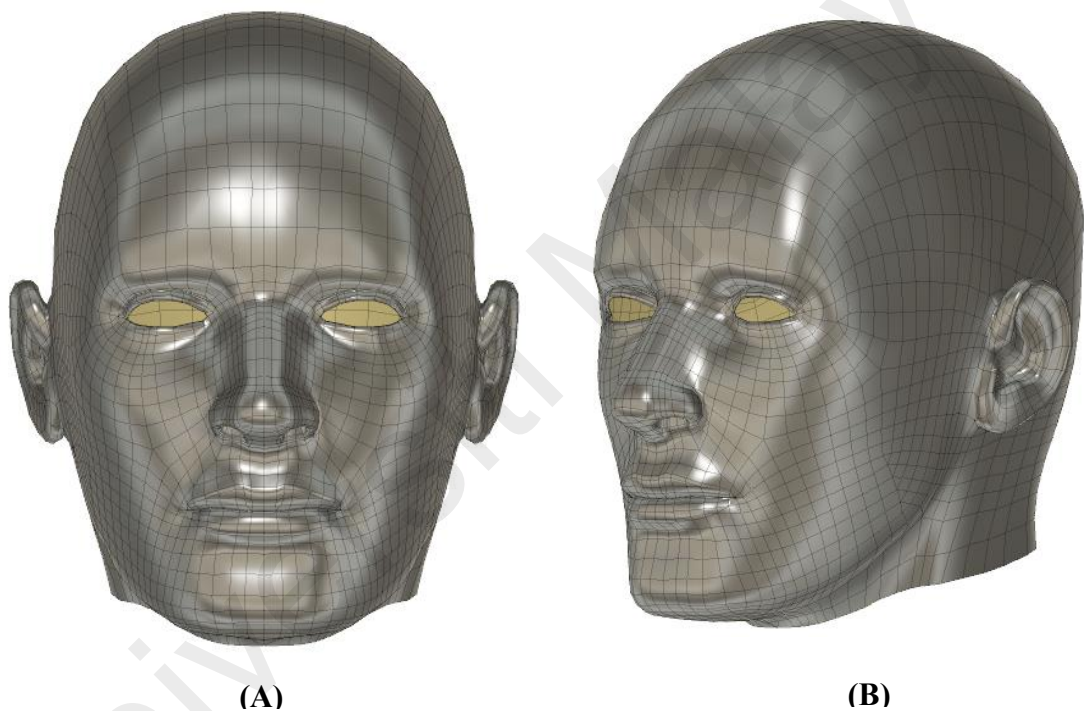


**Figure 3.2.** Untextured mesh and low quadrilateral-shaped cells were observed on the Turbosquid 3D head template of a Caucasian male which was obtained from an open-source platform. **(A)** Front view. **(B)** Isometric view. [Obtained from *Mad Mouse Design (2007)*]

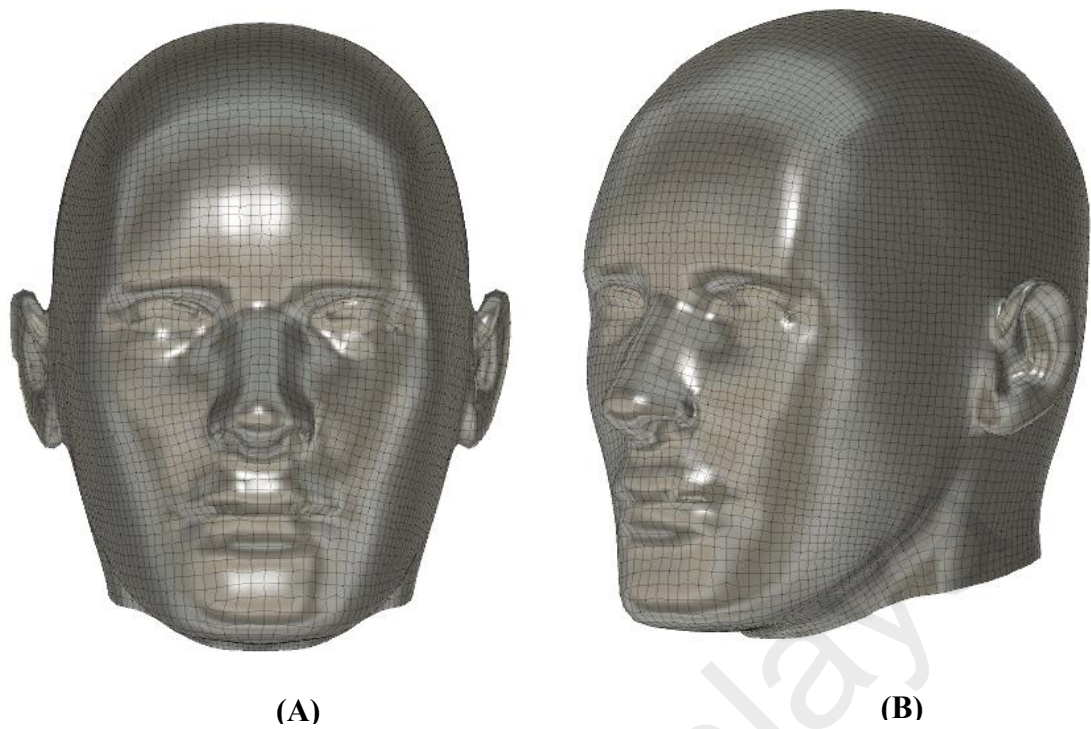


**Figure 3.3.** A restructured and redefined quadrilateral-shaped cells of a Caucasian head template. **(A)** Front view. **(B)** Isometric view.

**Table 3.1.** Skin thickness values for the corresponded anatomical location. [Obtained from *Chopra et al. (2015)*]

Anatomical Location	Skin Thickness (mm)
Forehead	1.22
Cheek	1.34
Temple	1.29

### 3.1.2 Local flap designs

The following step was to create deformities to the face model. The local flaps studied were advancement, rotation, and rhomboid. These local flaps were designed

based on general guidelines proposed by dermatologists (*Dockery, 2012; Momeni & Souza, 2019; Oliaei & Chu, 2013; Starkman et al., 2017*) and were parameterized according to the defect size of 20 mm. A dimension of 1.20 mm was configured to indicate the incision surgery size. The deformities were formed by embedding these designs on the outermost face layer, which was the epidermis, and then cut extruded thoroughly. Each of the local flaps was assigned to its respective anatomical locations. Geometry schematics defining each of the local flaps are shown in Figure 3.4. Note that the placement of the incision designs was within RSTL except for the temple-forehead junction where RSTL can be more ambiguous.

Advancement flap was an ideal option for forehead reconstruction. For this study, the advancement flap was designed with a defect-width to a flap-length ratio of 1:2.5 approximately as can be seen in Figure 3.4 (a). As such, the 20 mm defect was excised with a square-shaped of 25 mm. Two incision lines were made by extending away from the excision portion with a length of 62.50 mm in which creating a flap. Additionally, two Burow's triangles were excised on each corner of the flap base to provide the flexibility for the flap to extend. In clinical practice, Burow's triangles may aid in reducing the tension on the ends of advancement flaps. However, the excisions of Burow's triangles were unnecessary in most cases due to the minimal effect on supple skin. Note that the Burow's triangles were parameterized large enough to assist the flap mobility.

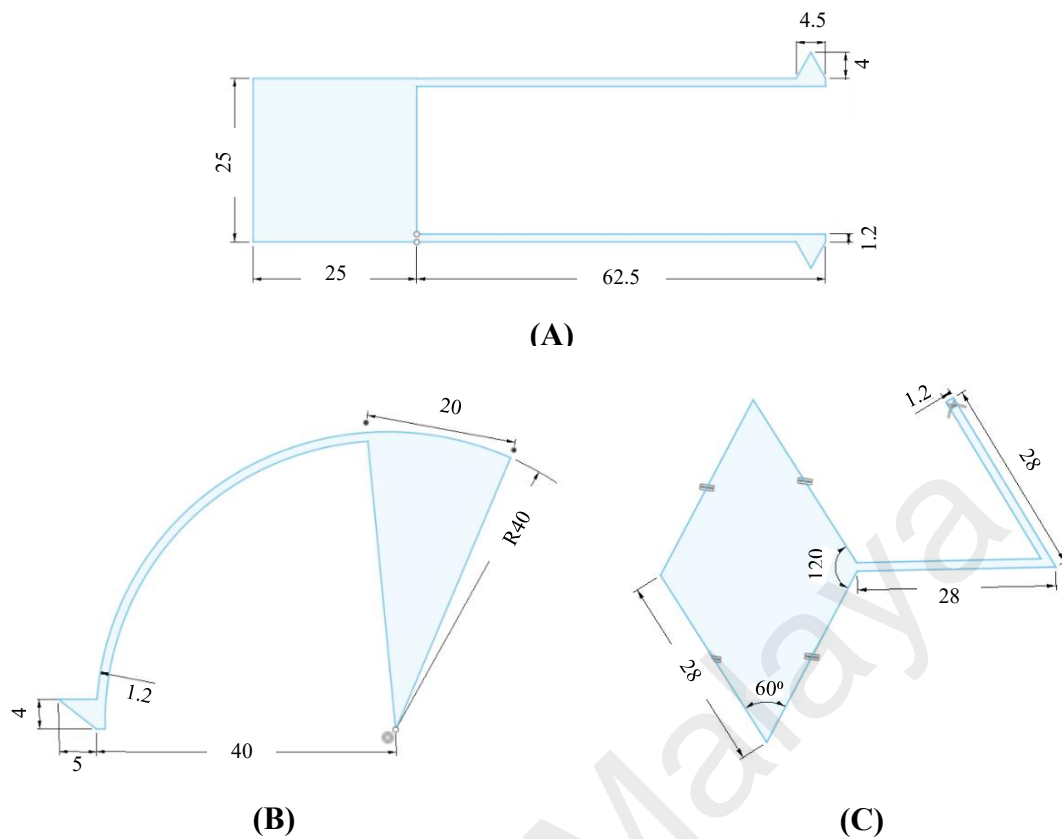


**Figure 3.4.** Geometrical descriptions of (A) advancement flap (B) rotation flap and (C) rhomboid flap. All measurements are in mm unit.

Meanwhile, a rotation flap was chosen to repair the cheek area. The rotation flap was designed in a curvilinear manner with a triangular-shaped effect. In this study, the height-width ratio of the triangular defect was 2:1 and the length of the arc was 4 times the width of the triangular defect as can be seen in Figure 3.4 (b). The 20 mm defect size was excised with a triangular-shaped at a given height of 40 mm and width of 20 mm. The incision line was drawn as an arc and the distance from the centre of the circle that made up an arc length was 40 mm. Additionally, a Burow's triangle was excised at the distal end and sufficiently parameterized to allow some extension to the rotation of the curved incision.

For the reconstruction of the temple area, a rhomboid flap was chosen instead. The rhomboid flap was designed as an equilateral parallelogram of 28 mm with an acute angle of  $60^\circ$  and  $120^\circ$ , in which created a rhombus-shaped defect as shown in Figure 3.4 (c). The incision lines were constructed with the same side length where the first incision was extended  $120^\circ$  from the rhombus-shaped defect while  $60^\circ$  was an angle measured from the first incision to the second incision.

### 3.1.3 Material constitutive model

The present work adopted material properties from the work of *Chanda and Unnikrishnan (2017)*. It was understood that their skin model considered nonlinear, isotropic, and incompressible. A third-order Yeoh's hyper-elastic model was used to represent the human skin. According to the literature, the skin stress-strain data was gained from an *in vitro* uniaxial tensile test on the cadaveric dermis by *Ni Annaidh et al. (2012)*. The stress-strain response was fitted into the strain energy function (Equation 8) and the coefficients  $c_{10}$ ,  $c_{20}$ , and  $c_{30}$  were estimated by curve fitting (listed in Table 3.2). Meanwhile, the incompressibility coefficients  $d_1$ ,  $d_2$ , and  $d_3$  were set to zero to be taken as fully incompressible material (*Shahzad et al., 2015*). These coefficients were used for all models in ANSYS engineering data. It is noteworthy that the skin material properties were dominated by dermis properties. Although epidermis was included in the thickness, it was assumed to be neglected in the mechanical properties as the current literature (*Chanda & Unnikrishnan, 2017; Ni Annaidh et al., 2012*) disregarded the contribution of the epidermis in their study. This can be accepted as it was common to neglect the epidermis layer due to its minimum influence on mechanical behavior (*Hendriks, 2005; Hendriks et al., 2003*) compared to the dermis layer as the dermis plays an important role in contributing to the mechanical behavior of the skin (*Delalleau et al., 2008*).

**Table 3.2.** Material parameters of the Yeoh model. The coefficients  $c_{10}$ ,  $c_{20}$ , and  $c_{30}$  are defined as material constants whereas  $d_1$ ,  $d_2$ , and  $d_3$  are the incompressibility constraints. [Obtained from (Chanda & Unnikrishnan, 2017)]

Coefficient	Parameter (MPa)
$c_{10}$	0.948
$c_{20}$	4.946
$c_{30}$	0.01
$d_1 = d_2 = d_3$	0

#### 3.1.4 Finite element mesh

The generation of the mesh demands decision-making on maintaining the accuracy of the solutions based on the shape of cells and their statistics. The attributes associated with the evaluation of mesh quality were Jacobian ratio and mesh skewness. The Jacobian matrix is a ratio of an ideal-shaped element to the given element in which the deviation should be between 1 (minimum) and 10 (maximum). It is considered unacceptable if the minimum and maximum possess different signs (+ve or -ve) (Ruggiero et al., 2019). The other important quality check is skewness. Skewness is defined as a measure of distortion of a given element compared to its ideal elements. It is advisable that the maximum value should be kept less than 0.95 for tetrahedral cells (Fabritius & Tabor, 2016). Off-range quality values may lead to convergence difficulties and inaccurate results.

Two main polygon meshes of tetrahedral and hex dominant mesh method using the base Caucasian model were compared based on mesh quality criterion to conclude the best quality between the latter. Subsequently, a significant amount of effort was

used to determine the appropriate element size using the size function control. It was found that the 2.60 mm element size fitted within the minimum mentioned range. After the meshing, it can be seen that the tetrahedral mesh method (Figure 3.5) had more uniform elements, whereas the hex dominant mesh method (Figure 3.6) contained a mix of quads-and triangular-shaped cells instead of all quads-shaped cells, which will result in an inaccurate solution. Moreover, the generated meshes as shown in Figures 3.7 and 3.8 suggested that the tetrahedral mesh method provided a more acceptable trade off on the general rule of Jacobian ratio and skewness. Subsequently, all deformed models were meshed using a 2.60 mm element size and tetrahedral mesh method. The results were presented from Figure 3.9 to 3.11. In a nutshell, a deformed face model with an advancement flap was discretized with 124 862 elements, whereas a rotation flap with 124 717 elements and finally, a rhomboid flap with 124 238 elements.

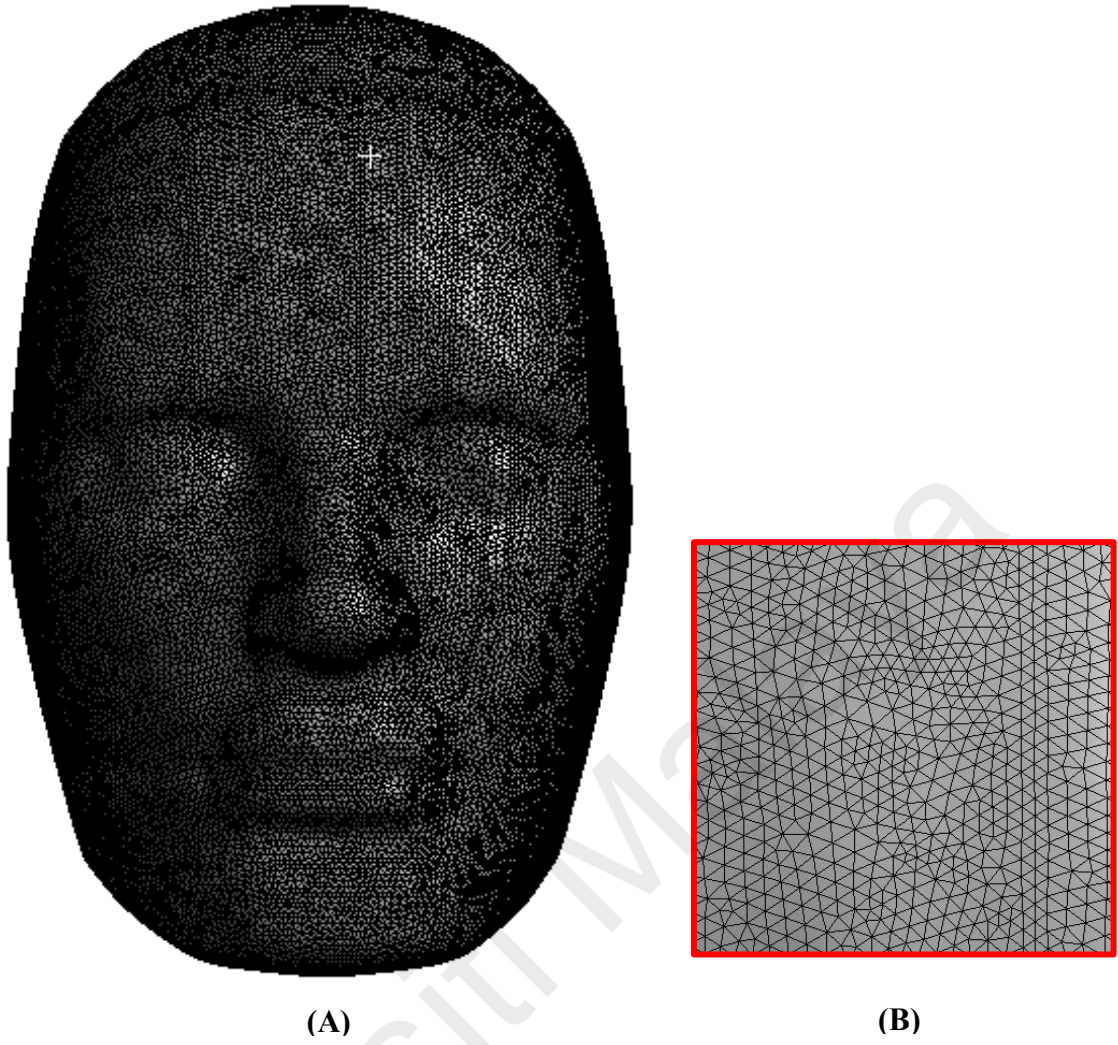


**Figure 3.5.** Meshed base face model using tetrahedral mesh method. **(A)** Full view **(B)** Close-up view.

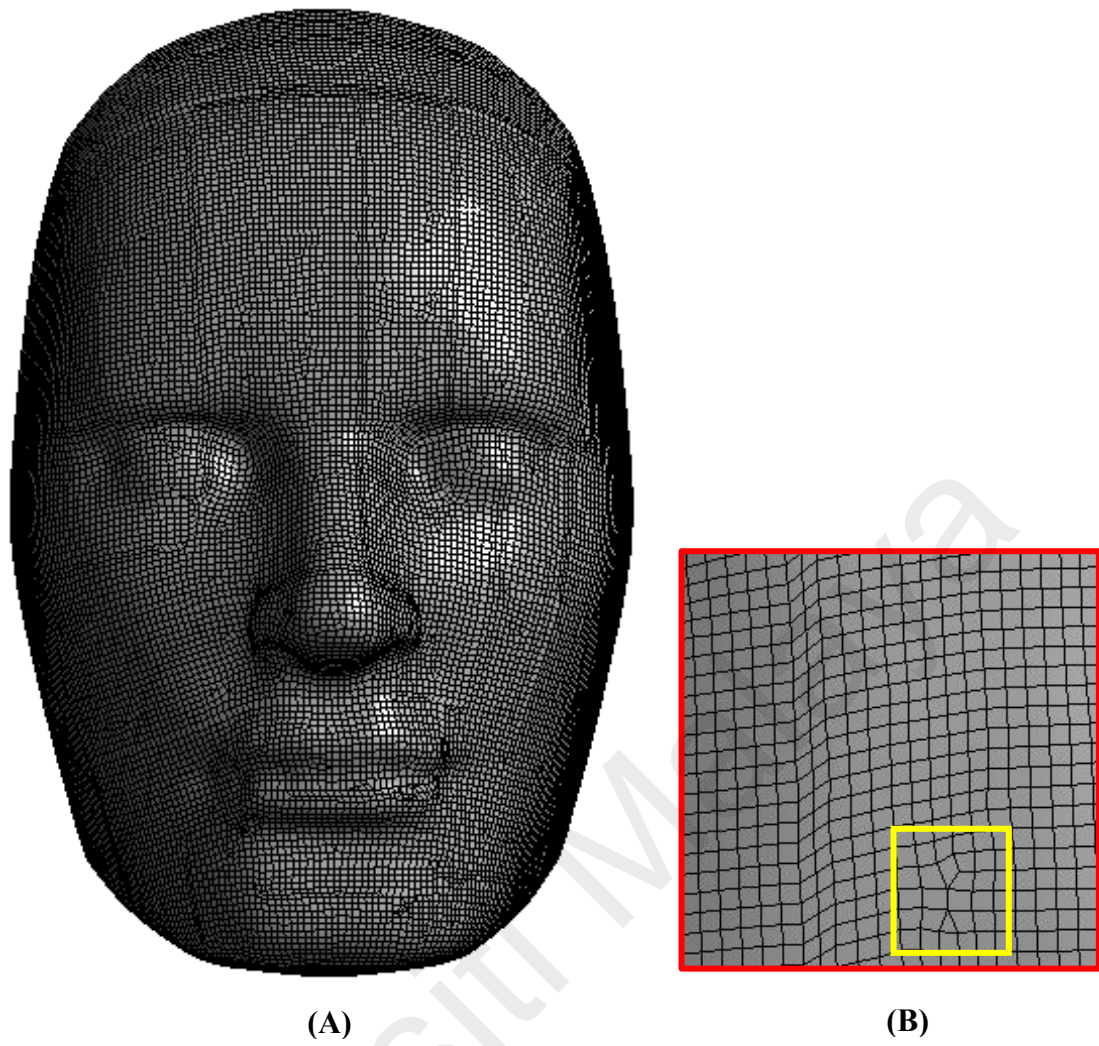


**Figure 3.6.** Meshed base model using hex dominant mesh method. **(A)** Full view **(B)** Close-up view.

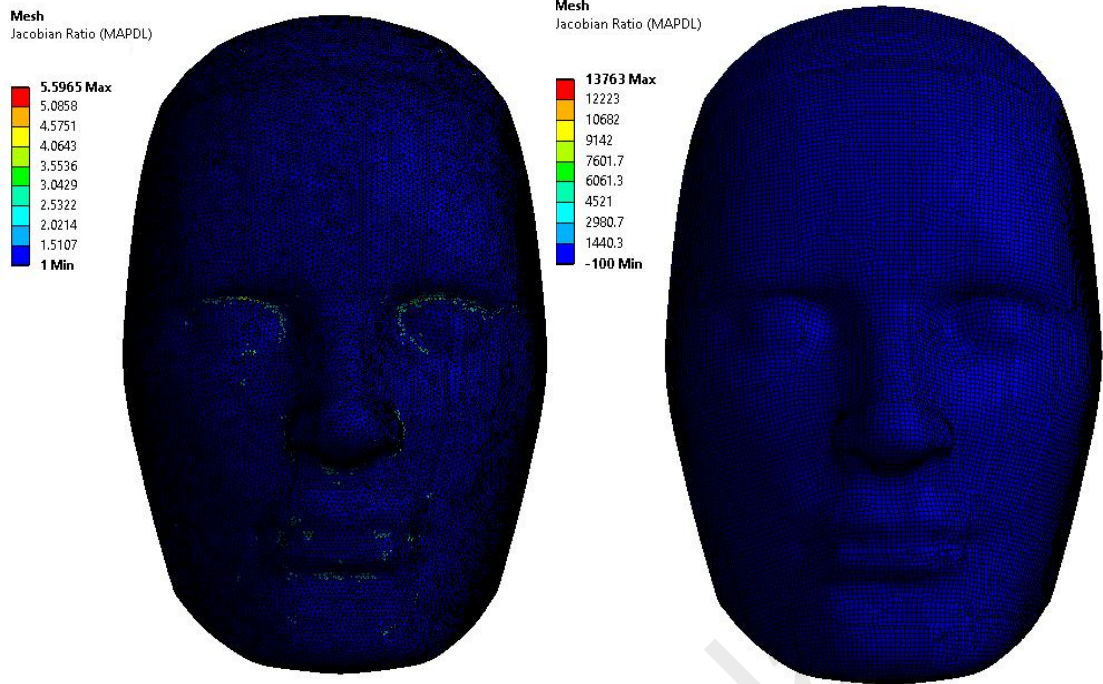


**Figure 3.7.** Jacobian ratio of the tetrahedral mesh (left) and hex dominant mesh (right).

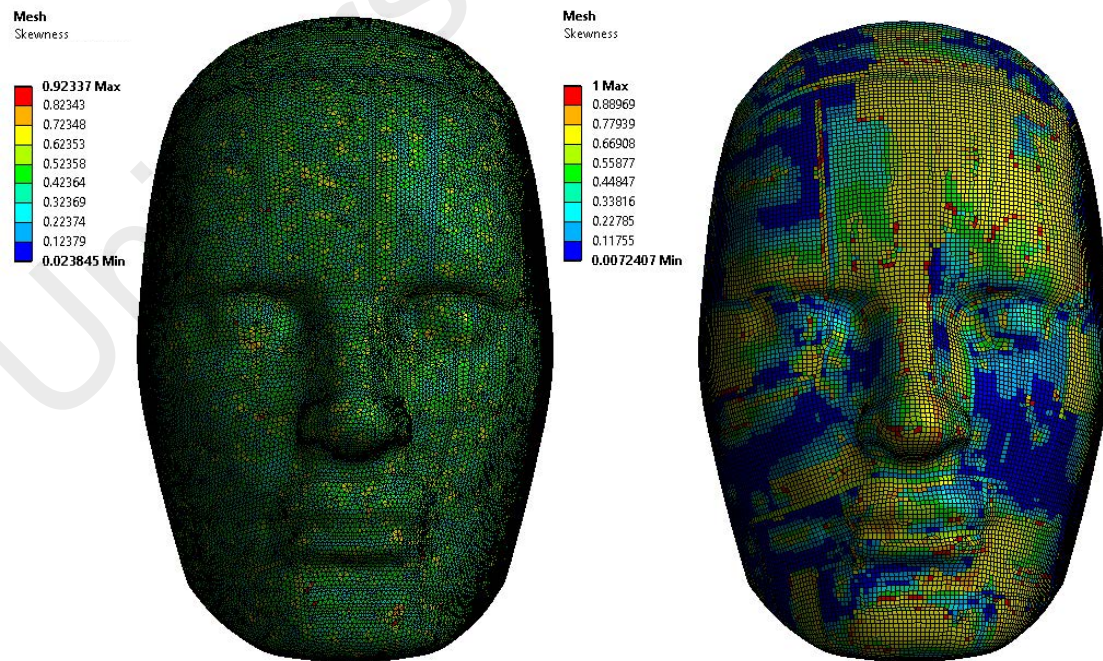


**Figure 3.8.** Skewness of the tetrahedral mesh (left) and hex dominant mesh (right).

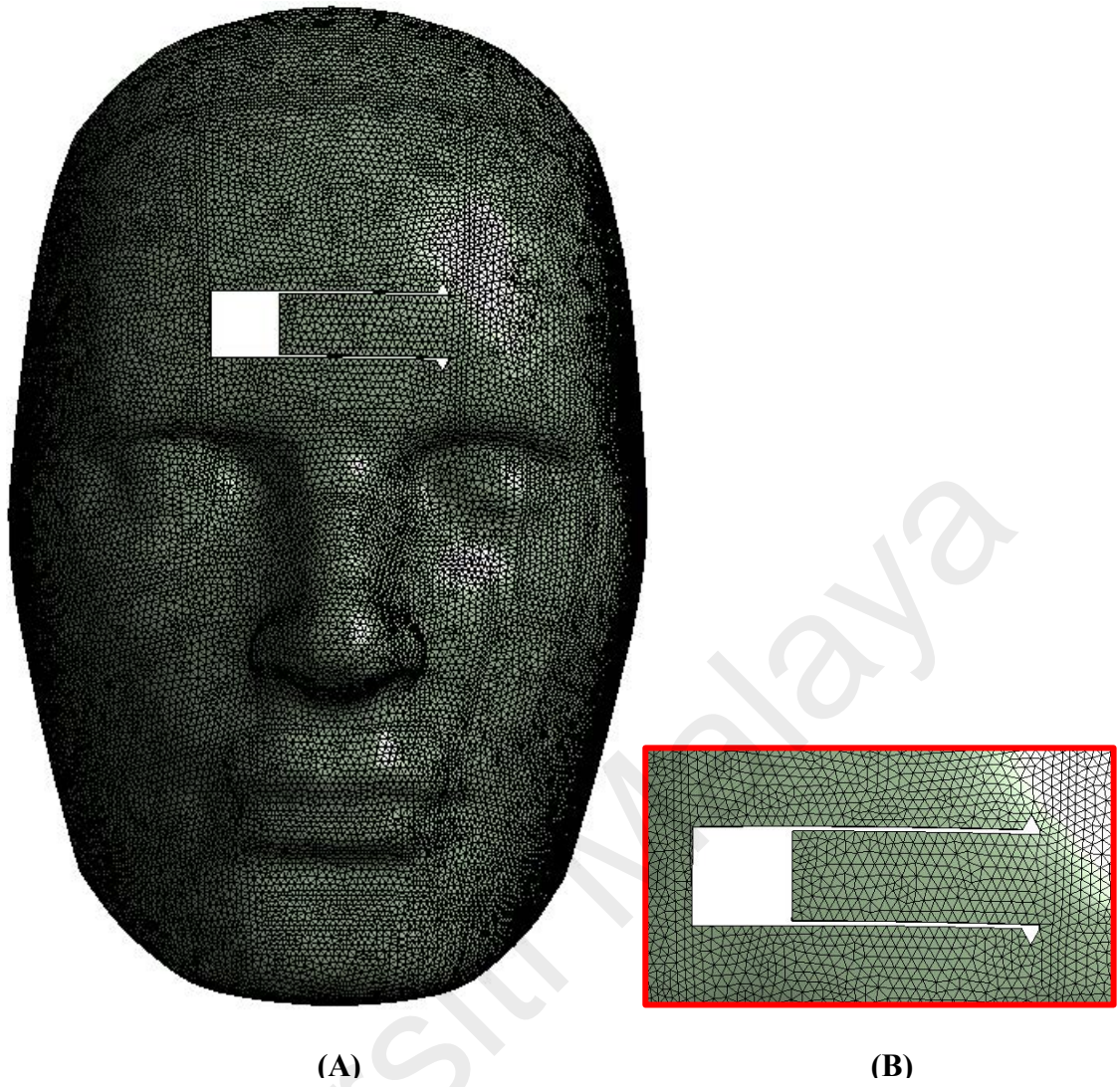


**Figure 3.9.** Meshed geometries of advancement flap with the tetrahedral mesh assuming that forehead thickness was 1.22 mm, element size of 2.60 mm and a total of 124 862 elements **(A)** Caucasian model with an opening advancement-shaped hole. **(B)** Area of interest at close proximity.

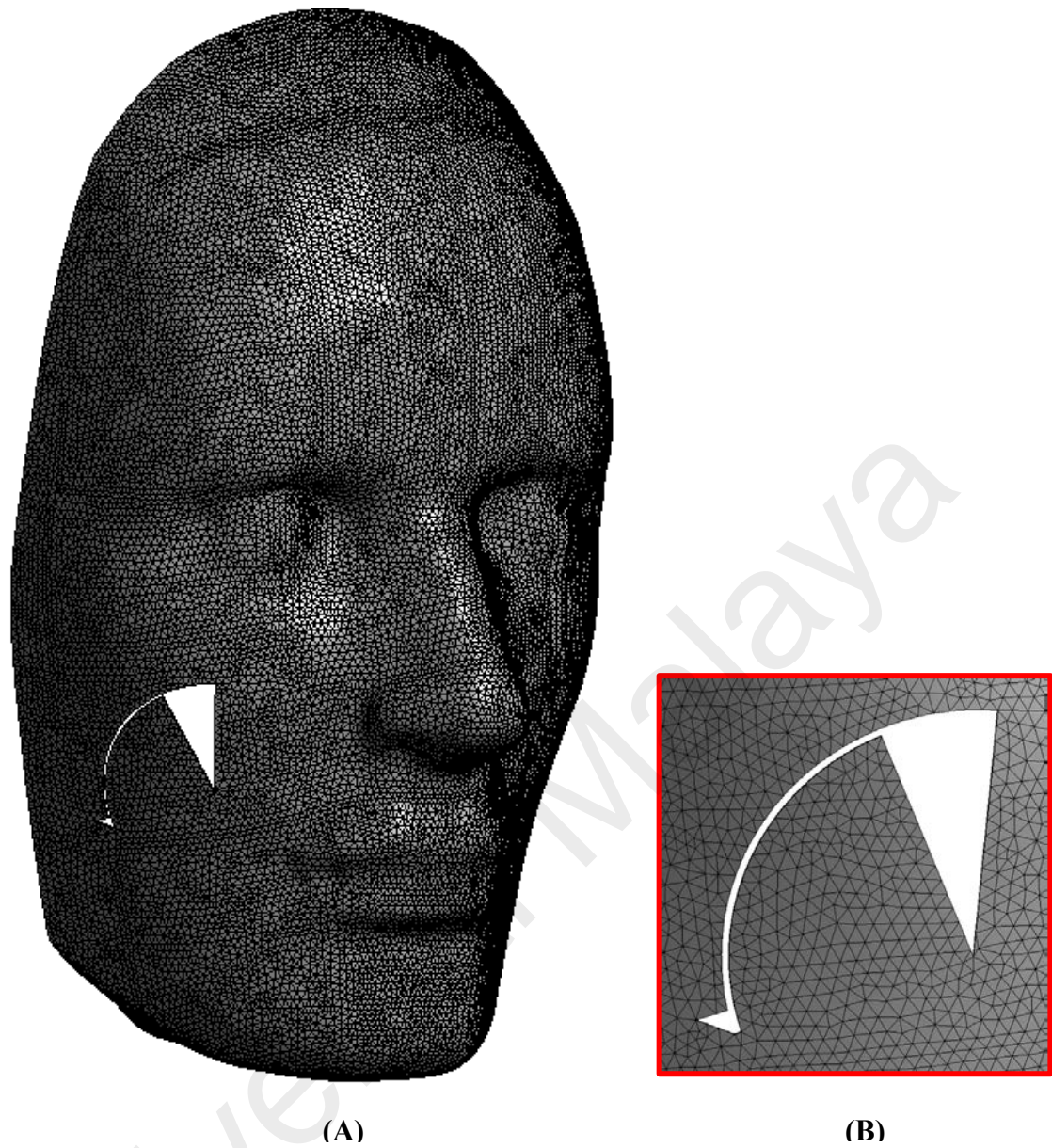


**Figure 3.10.** Meshed geometries of rotation flap with the tetrahedral mesh assuming that cheek thickness was 1.34 mm, element size of 2.60 mm and a total of 124 717 elements **(A)** Caucasian model with an opening rotation-shaped hole. **(B)** Area of interest at close proximity.

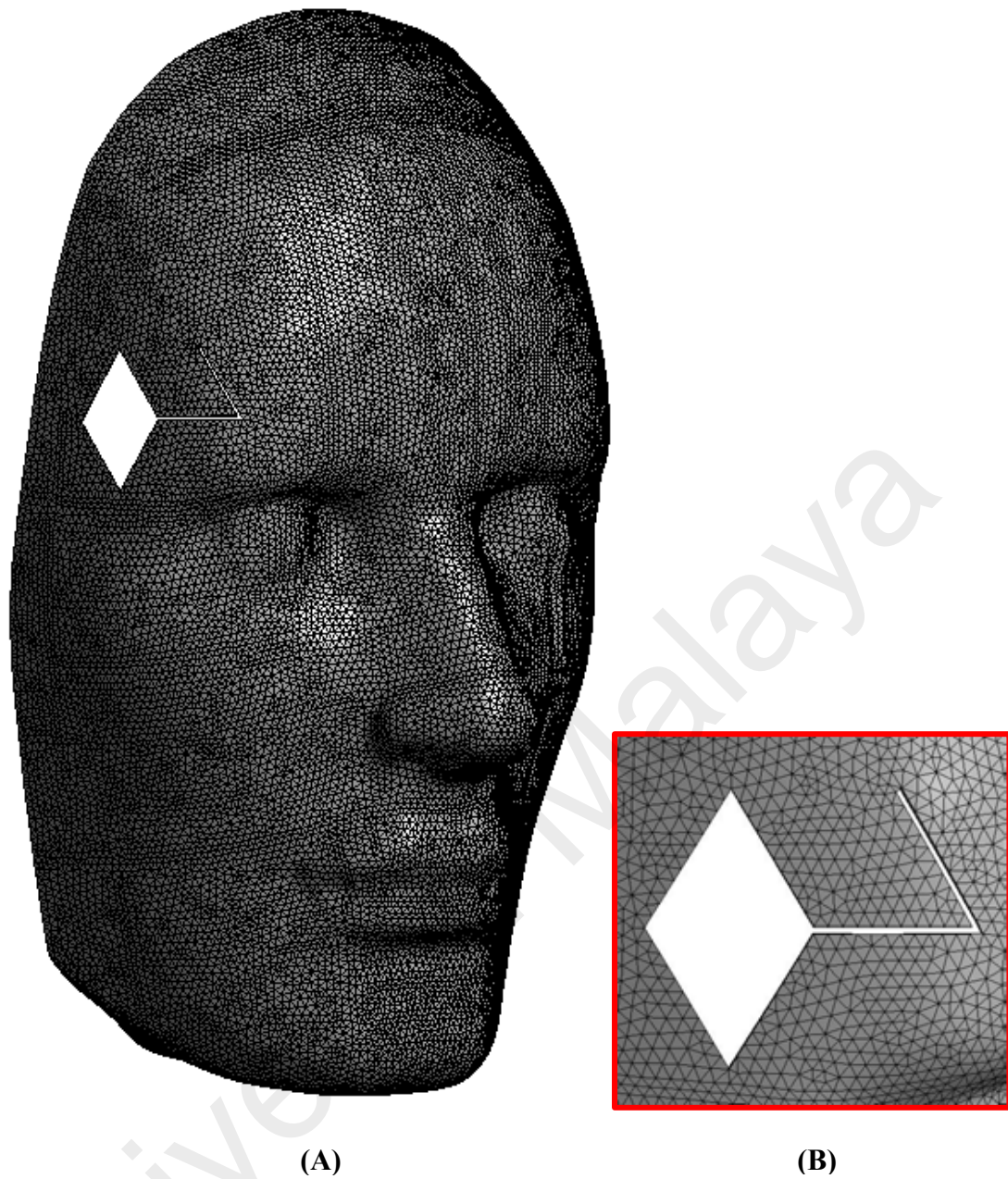


**Figure 3.11.** Meshed geometries of the rhomboid flap with the tetrahedral mesh assuming that temple thickness was 1.29 mm, element size of 2.60 mm and a total of 124 238 elements **(A)** Caucasian model with an opening rhomboid-shaped hole. **(B)** Area of interest at close proximity.

### 3.1.5 Boundary conditions

A face patch of 1 mm thickness was perfectly bonded (using no separation and normal Lagrange type contact pairs) underneath the excised areas for all existing models. It was an ideal condition to allow the flap to deform according to the face's curved surface. The outer edges of the face models were held fixed in all degrees of freedom.

Prescribed displacements were applied along the edges of the skin flaps in X-, Y- and Z-axis direction and X-, Y-, Z-degree rotation (whenever applicable) to indicate the action of skin flap pulling towards wound closure. The direction of the pulling and the amount of the applied displacements to acquire wound closure using three different local flap techniques can be seen in Table 3.3.

**Table 3.3.** A tabulated list of the applied displacements. The arrows show the direction of movement according to the applied values.

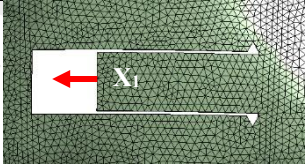
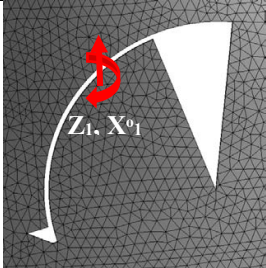
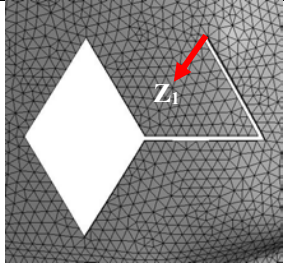
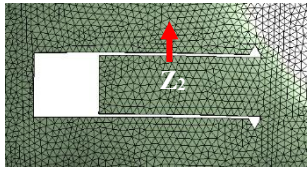
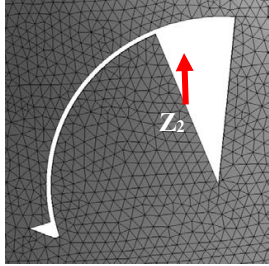
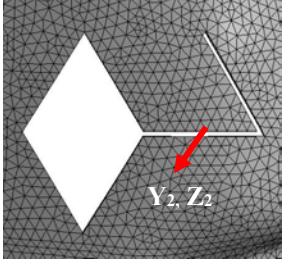
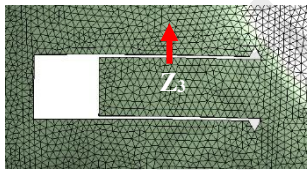
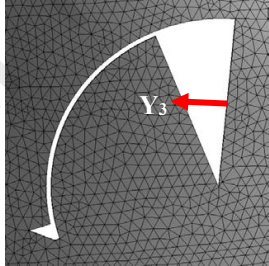
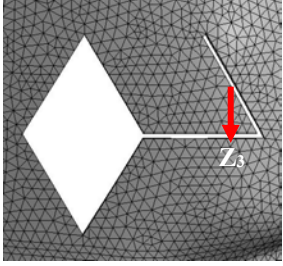
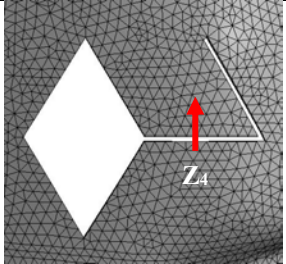
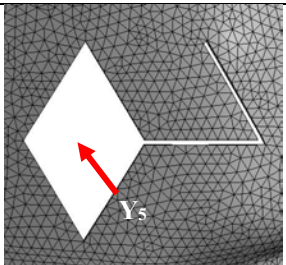
Displacement	Local Flap Design		
	Advancement Flap	Rotation Flap	Rhomboid Flap
Direction-1			
	$X_1 = -24.50 \text{ mm}$ $Y_1 = \text{Free}$ $Z_1 = \text{Free}$ Rotation $X_1 = \text{Free}$ Rotation $Y_1 = \text{Free}$ Rotation $Z_1 = \text{Free}$	$X_1 = \text{Free}$ $Y_1 = \text{Free}$ $Z_1 = 11.50 \text{ mm}$ Rotation $X_1 = 19^\circ$ Rotation $Y_1 = \text{Free}$ Rotation $Z_1 = \text{Free}$	$X_1 = \text{Free}$ $Y_1 = 2.50 \text{ mm}$ $Z_1 = -14.50 \text{ mm}$ Rotation $X_1 = \text{Free}$ Rotation $Y_1 = \text{Free}$ Rotation $Z_1 = \text{Free}$

Table 3.3. Continued.

Displacement	Local Flap Design		
	Advancement Flap	Rotation Flap	Rhomboid Flap
Direction-2	 <p> <math>X_2 = \text{Free}</math>  <math>Y_2 = \text{Free}</math>  <math>Z_2 = 0.60 \text{ mm}</math>                      Rotation <math>X_2 = \text{Free}</math>                      Rotation <math>Y_2 = \text{Free}</math>                      Rotation <math>Z_2 = \text{Free}</math> </p>	 <p> <math>X_2 = \text{Free}</math>  <math>Y_2 = \text{Free}</math>  <math>Z_2 = 1.50 \text{ mm}</math>                      Rotation <math>X_2 = \text{Free}</math>                      Rotation <math>Y_2 = \text{Free}</math>                      Rotation <math>Z_2 = \text{Free}</math> </p>	 <p> <math>X_2 = \text{Free}</math>  <math>Y_2 = 25.00 \text{ mm}</math>  <math>Z_2 = -21.00 \text{ mm}</math>                      Rotation <math>X_2 = \text{Free}</math>                      Rotation <math>Y_2 = \text{Free}</math>                      Rotation <math>Z_2 = \text{Free}</math> </p>
Direction-3	 <p> <math>X_3 = \text{Free}</math>  <math>Y_3 = \text{Free}</math>  <math>Z_3 = -0.60 \text{ mm}</math>                      Rotation <math>X_3 = \text{Free}</math>                      Rotation <math>Y_3 = \text{Free}</math>                      Rotation <math>Z_3 = \text{Free}</math> </p>	 <p> <math>X_3 = \text{Free}</math>  <math>Y_3 = 2.00 \text{ mm}</math>  <math>Z_3 = \text{Free}</math>                      Rotation <math>X_3 = \text{Free}</math>                      Rotation <math>Y_3 = \text{Free}</math>                      Rotation <math>Z_3 = \text{Free}</math> </p>	 <p> <math>X_3 = \text{Free}</math>  <math>Y_3 = \text{Free}</math>  <math>Z_3 = -23.50 \text{ mm}</math>                      Rotation <math>X_3 = \text{Free}</math>                      Rotation <math>Y_3 = \text{Free}</math>                      Rotation <math>Z_3 = \text{Free}</math> </p>

**Table 3.3.** Continued.

Displacement	Local Flap Design		
	Advancement Flap	Rotation Flap	Rhomboid Flap
Direction-4			 <p> <math>X_4 = \text{Free}</math>  <math>Y_4 = \text{Free}</math>  <math>Z_4 = -9.50 \text{ mm}</math>                      Rotation <math>X_4 = \text{Free}</math>                      Rotation <math>Y_4 = \text{Free}</math>                      Rotation <math>Z_4 = \text{Free}</math> </p>
Direction-5			 <p> <math>X_5 = \text{Free}</math>  <math>Y_5 = 0.10 \text{ mm}</math>  <math>Z_5 = \text{Free}</math>                      Rotation <math>X_5 = \text{Free}</math>                      Rotation <math>Y_5 = \text{Free}</math>                      Rotation <math>Z_5 = \text{Free}</math> </p>

### 3.1.6 Assumptions on the FE analysis model

The assumptions made in the present work were as follows:

- 1) The focus of this study was on skin recovery, thus the contour underlying the skin does not significantly interfere with the results.
- 2) The human bone would not be included in the study. In these types of operations, the bone has a minimum influence on the wound closure as the human skin contains multiple layers, as well as the distance from the first layer to the bone, is huge. The bone will also be fixed in terms of position.
- 3) The FE models were modelled as nonlinear, isotropic hyper-elastic, and incompressible models. The notion of isotropic behavior in the simulations was to simplify the computational algorithm and reduced the computational time by avoiding multiple directional variables.
- 4) The FE models did not take into account the effect of the epidermis layer. Although the skin thickness was composed of the combined dermis and epidermis values, the epidermis properties were neglected due to its minimal effect on mechanical behaviour (*Hendriks, 2005; Hendriks et al., 2003*).

## 3.2 Case Study 2: Asian Models

The FE modeling for Case Study 2 involved the creation of surrogate surgery models based on the Asian population using two head templates from two different genders: female and male. The idea was to deliver two post-operative simulations of two genders and compare the sensitiveness of wound closure to respective local flap designs. The post-operative simulations were analyzed and compared based on the sensitiveness of

wound closure between genders. The overall workflow for Case Study 2 is summarized in Figure 3.12.

Since the focus of this case study was related to the gender effect, two head templates of opposite genders were acquired from a credible source. These head templates were used as base models to create facial injuries with different shapes of incision designs. From here, the procedures in modeling the 3D wound closures replicate the methodology used in Case Study 1 (see Figure 3.12) starting from the 'Development of CAD model' until 'Post-processing' and repeated for the following 3D deformed face model using other local flap designs. Final solutions of post-operative simulations from two different genders were then compared and discussed.

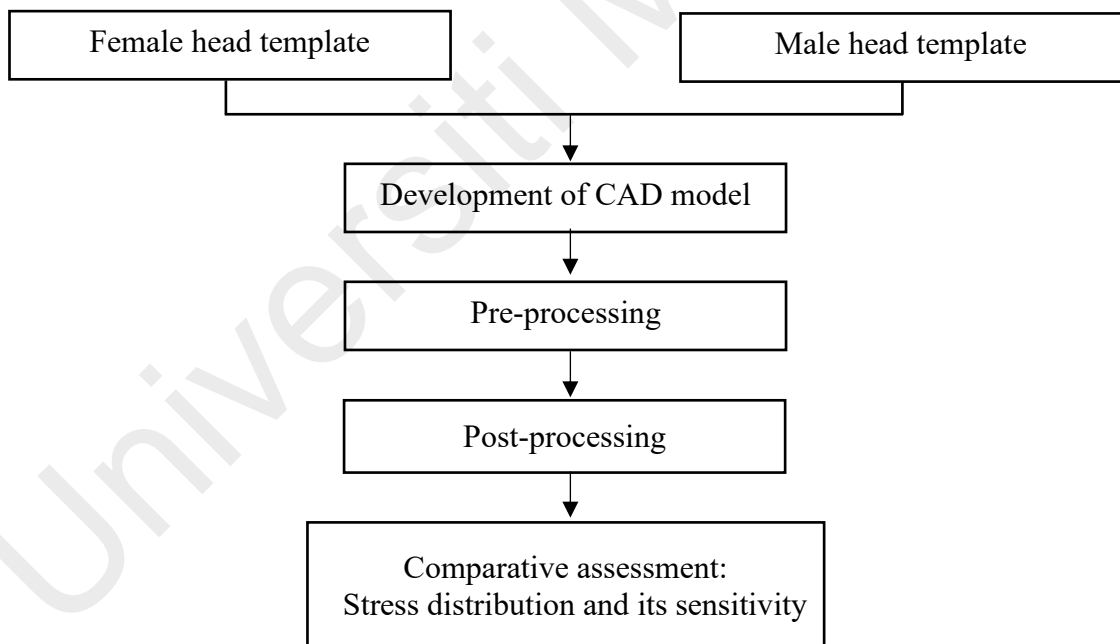


**Figure 3.12.** The overall workflow.

### 3.2.1 Face model

Standardized 3D head templates of Asians were obtained for use. Female and male head templates of Chinese adults were obtained from Dr. Yan Luximon of The Hong Kong Polytechnic University, China. The dimensions of each of the head templates were described in a bounding box of 179 x 204 x 246 mm for an Asian female and 189 x 218 x 254 mm for an Asian male. These templates were generated using facial landmarks on the faces and the structure of the heads and face surfaces were formed simultaneously with multiple anatomic locations via 3D scanning technology. Originally, the head templates were in the form of triangular-shaped cells. It is said that a mesh body would be efficient if it is a structured grid with quadrilateral cells in 2D and hexahedra cells in 3D. Thus, modifications to the mesh bodies were performed by converting the triangular-shaped cells to quadrilateral-shaped cells. Figure 3.13 presents the primary mesh condition of the female head template while Figure 3.14 shows the result of mesh conversion in quadrilateral-shaped cells. Meanwhile, mesh conversion from triangular-shaped to quadrilateral-shaped cells for the male head template can be observed from Figures 3.15 to 3.16. Despite the full features provided on these templates, half of the areas were excluded in this study, including the ears to avoid complications following the conversion to a 3D state.

A 3D state was done by thickening the head templates with the intention of imitating an actual human face. Similar to Case Study 1, three modified head templates from each gender were prepared and thickened according to the chosen anatomic locations (later referred to as “face models”). Hence, a total of six models existed where each gender possessed three models correlated to three different wound closure scenarios. This was due to the limitations provided by the ANSYS software, including the application of a single layer to simplify the numerical simulation. Even so, the

literature on the thickness measurement with Asian subjects was limited to the point where relevant data for facial skin thickness was inaccessible. The solution was to adopt available data from the Caucasian subjects and standardize the gender properties. The nearest possibility of adoption was to employ values from Case Study 1 (see Table 3.1) as their work comprised of a comprehensive collection of facial thicknesses data. It was assumed acceptable to do so due to the small differences of 10% (Querleux *et al.*, 2009) and 20% (Benítez & Montáns, 2017; L.O. Olsen *et al.*, 1995) found in the interindividual ethnicities and genders, respectively.

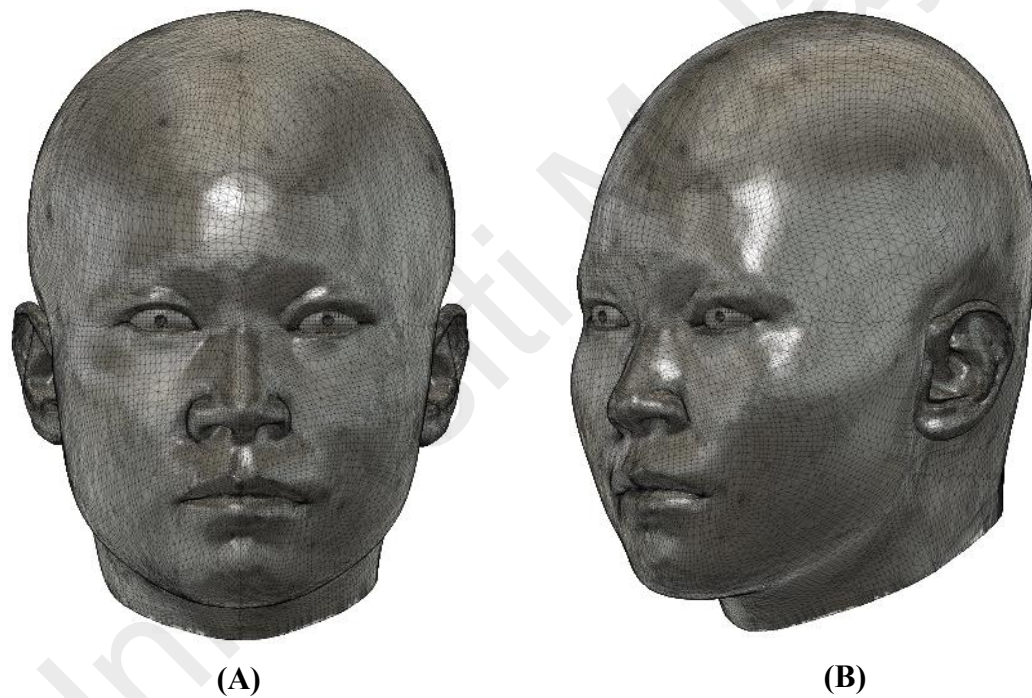


**Figure 3.13.** An unstructured grid with triangular-shaped cells was observed on the SizeChina 3D head template of an Asian female obtained from a credible source. **(A)** Front view. **(B)** Isometric view.

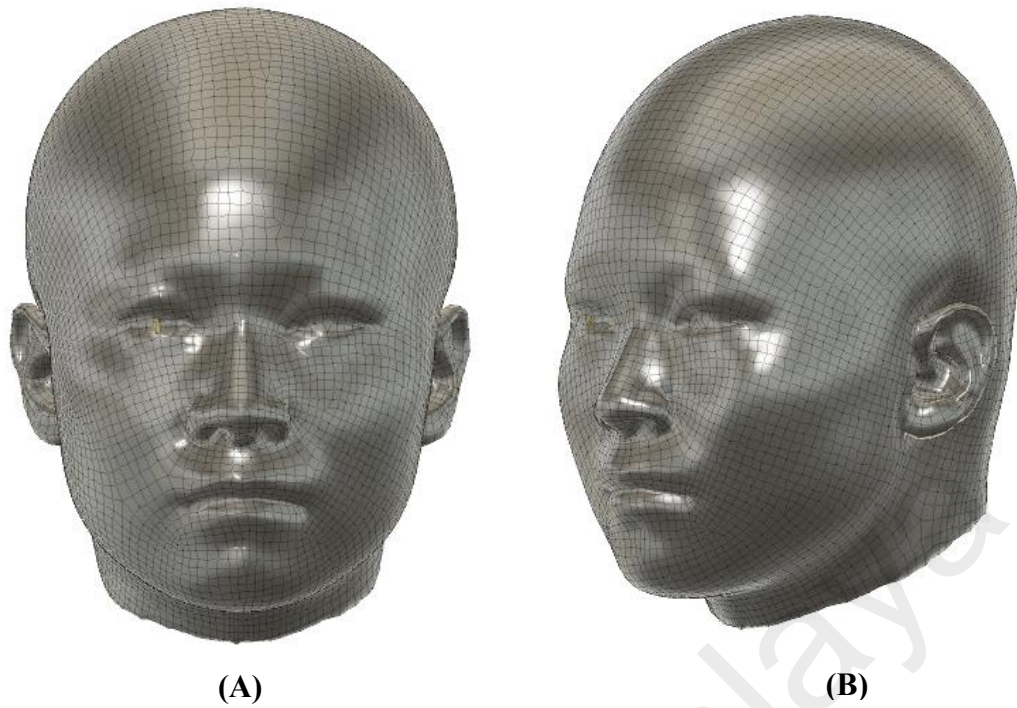


**Figure 3.14.** Quadrilateral-shaped cells of the female head template. **(A)** Front view. **(B)** Isometric view.

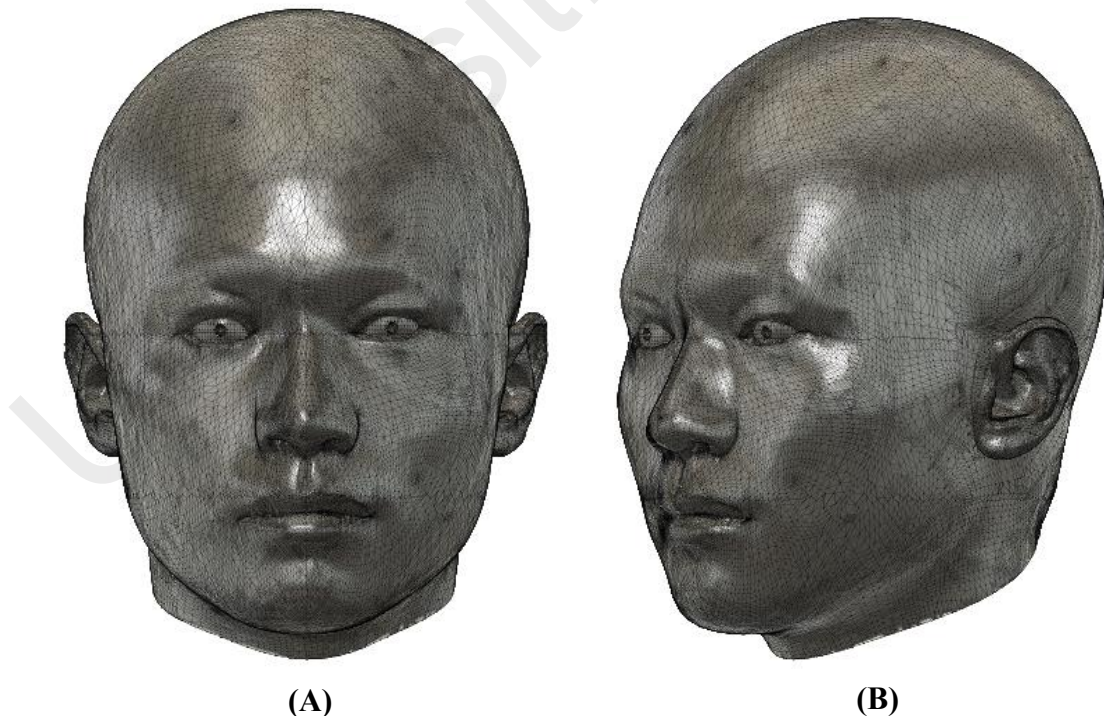


**Figure 3.15.** An unstructured grid with triangular-shaped cells was observed on the SizeChina 3D head template of an Asian male obtained from a credible source. **(A)** Front view. **(B)** Isometric view.

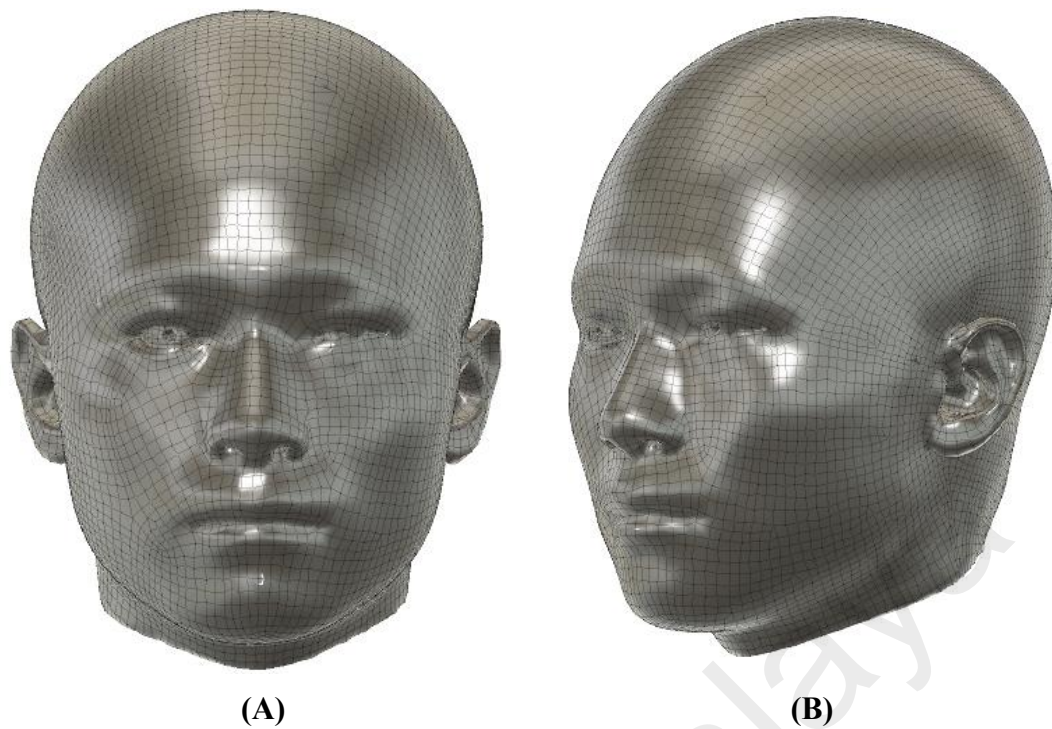


**Figure 3.16.** Quadrilateral-shaped cells of the male head template. **(A)** Front view. **(B)** Isometric view.

### 3.2.2 Local flap designs

Subsequently, disfigurement to the modified face models was carried out to create facial defects that mimicked the reconstructive phenomenon. Likewise, this study dealt with advancement, rotation, and rhomboid flaps. These local flaps were parameterized according to the defect size of 10 mm with their incision lines of 0.60 mm to indicate the incision surgery size. Deformities were formed by embedded these designs on the outermost face layer, which was the epidermis, and then cut extruded thoroughly. Noteworthy that each of the local flaps was assigned to its respective anatomical locations and the placement of these flaps was within RSTL except for the temple-forehead junction where RSTL can be more ambiguous.

Geometry schematics defining each of the local flaps are shown in Figure 3.17. The flap designs were quite similar to the flap designs provided in Case Study 1 except that the parameters were reduced twice to fit the current defect size. Specifically, the advancement flap in Figure 3.17 (a) included an excision of a 15 mm squareshape along with two incision lines of 37.50 mm in length extending from the defect. Two Burow's triangles were superimposed at the ends of incision lines. Next, the rotation flap in Figure 3.17 (b) involved an excision of a triangularshape with a height of 20 mm and a width of 10 mm. The arc indicated the incision lines with an arc length of 20 mm, drawn from the center of the circle. To allow more spreading to the movement of the flap, Burow's triangle was overlaid at the distal end. Finally, the rhomboid flap on Figure 3.17 (c) involved an excision of 14 mm with an equilateral parallelogram in rhombus-shaped as well as two incision lines that extended 120° from the rhombus-shaped defect and 60° from the first incision to the second incision.

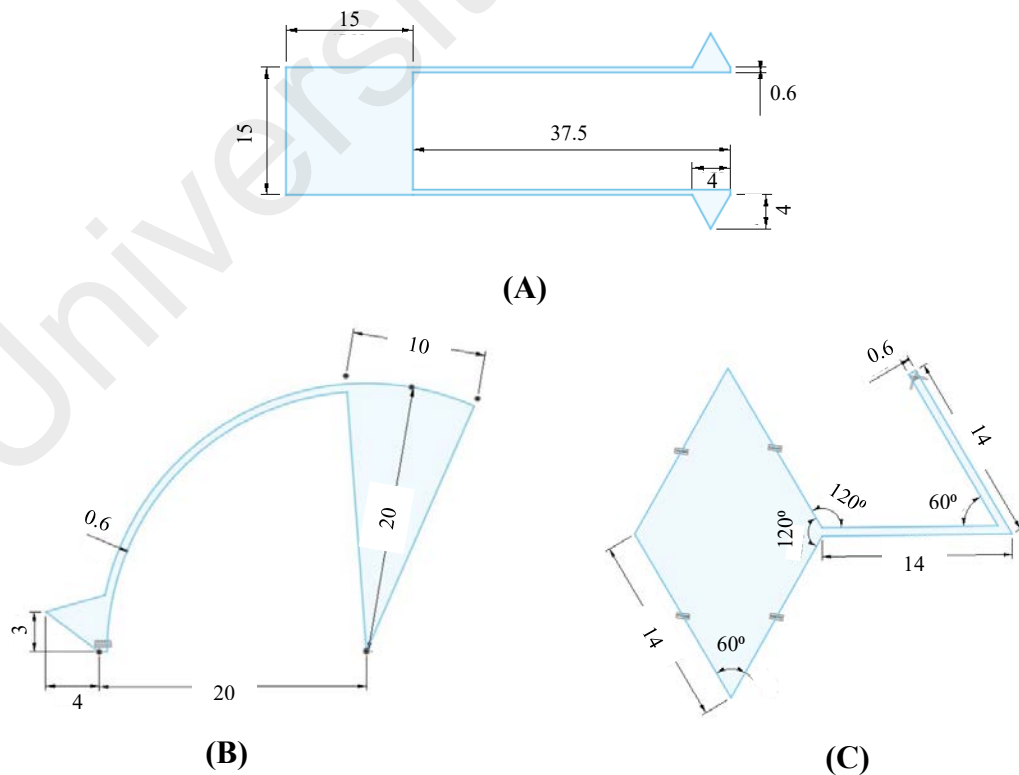


**Figure 3.17.** Geometrical descriptions of (A) advancement flap (B) rotation flap and (C) rhomboid flap. All measurements are in mm unit.

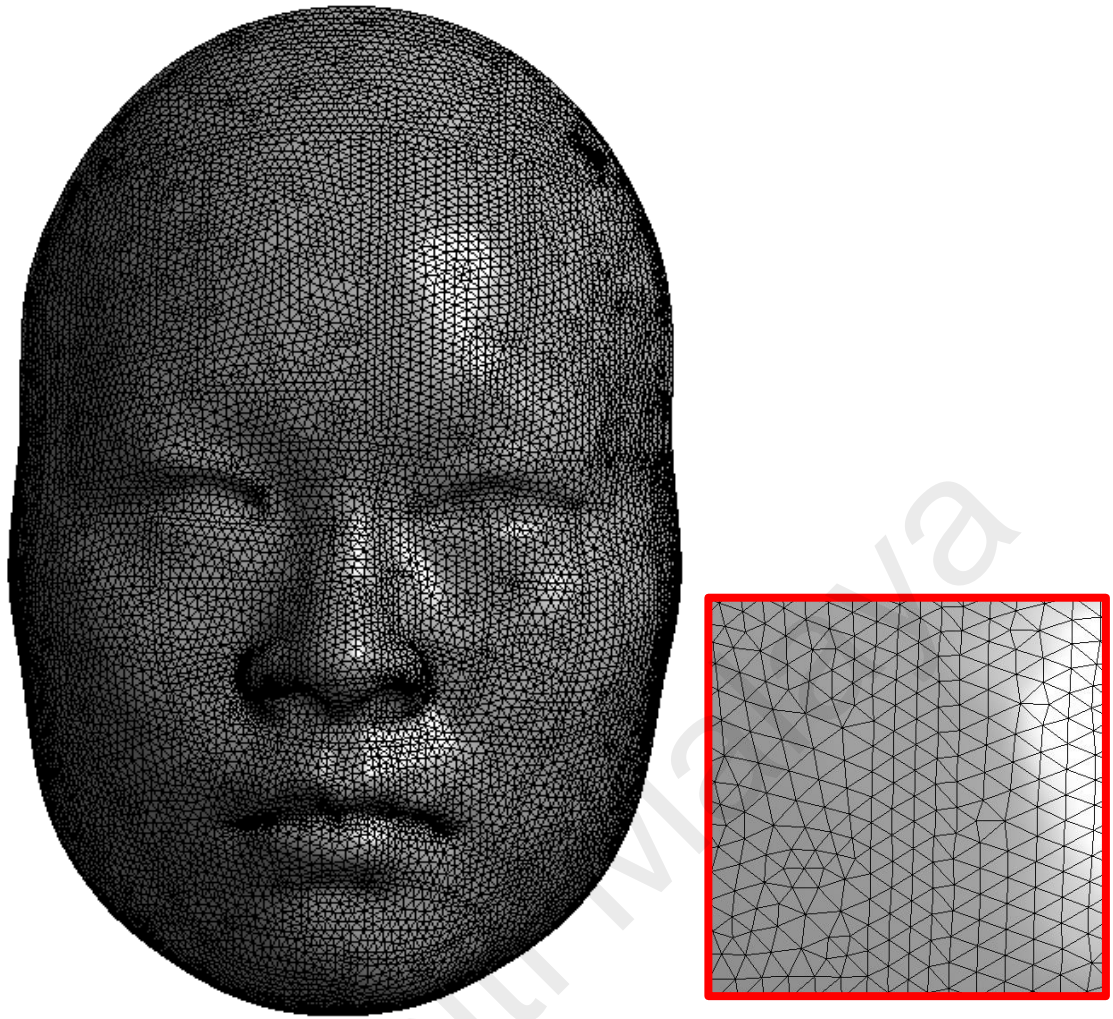
### 3.2.3 Material constitutive model

Since the study approach was mostly adopted from literature instead of deriving from experimental studies, the relevant data for material properties for Asian subjects were limited. Available data related to material properties that can be found in the literature were mostly dominated by the use of cadaveric subjects. As aforementioned, the difference between these ethnicities was found to be less than 10% and due to the low percentage difference, the study assumed the mechanical properties were closest in value. The study has pointed out these limitations while acknowledging that this study would be more accurate to differentiate the mechanical properties between genders. The material properties values were similar to Case Study 1 (see Table 3.2) where the literature assumed a third-order Yeoh model with the incompressibility coefficients  $d_1$ ,  $d_2$ , and  $d_3$  were set to zero to be taken as fully incompressible material (Shahzad et al., 2015). Note that the skin material properties were dominated by dermis properties while the epidermis was neglected as it was common to disregard the contribution of the epidermis due to its minimum influence on mechanical behaviour (Hendriks, 2005; Hendriks et al., 2003) compared to the dermal layer.

### 3.2.4 Finite element mesh

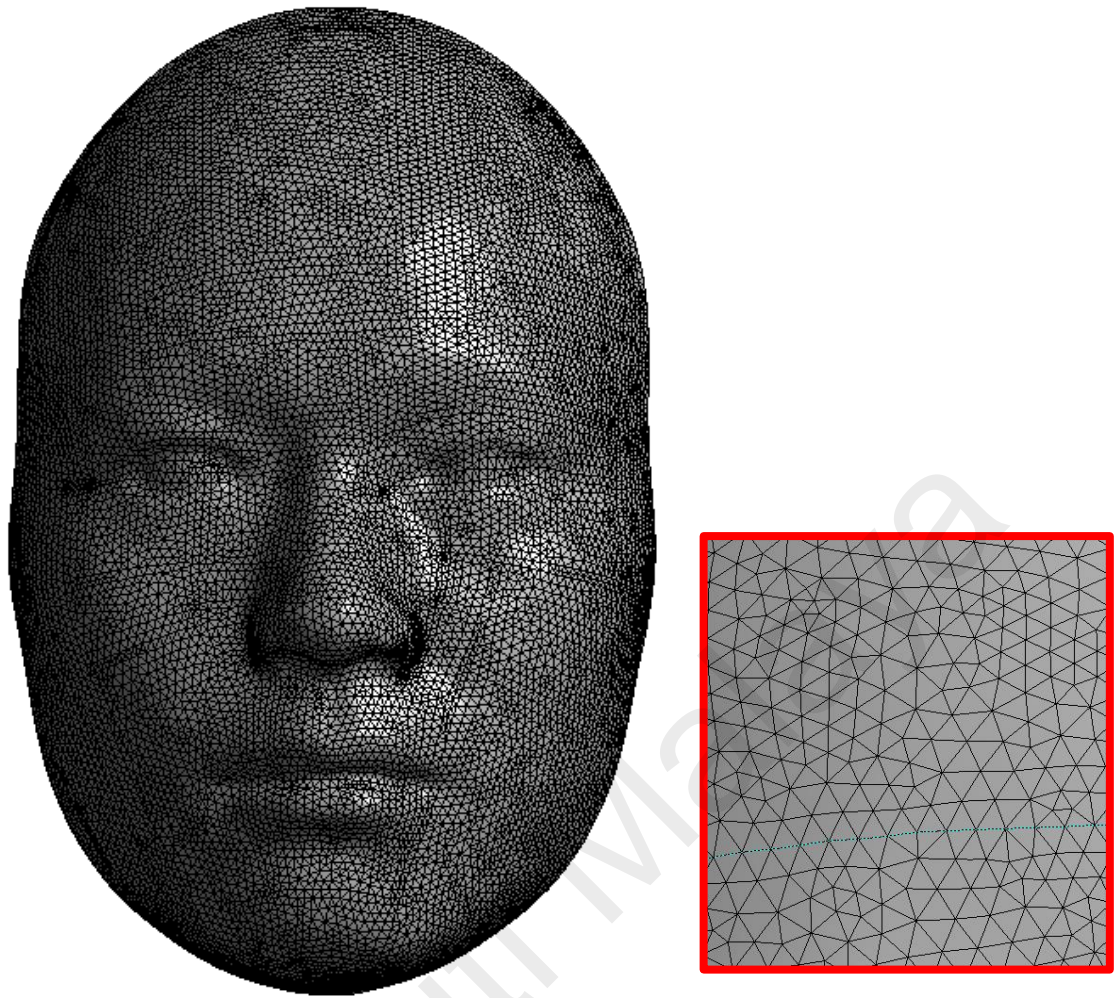
To ensure the accuracy of the FE analysis models, various mesh quality criteria were used. Similar to Case Study 1, the quality of the meshes was assessed through Jacobian ratio and mesh skewness. As aforementioned in 3.1.4, the general rules of Jacobian ratio and mesh skewness were that the Jacobian matrix should be between 1 and 10 as well as in the same sign (+ve or -ve) while the maximum value of skewness should be kept less than 0.95 (Fabritius & Tabor, 2016; Ruggiero et al., 2019).

Subsequently, a mesh optimization study was performed to determine the best option for the mesh method. Two main polygon meshes of tetrahedral and hex dominant mesh method using base Asian models were compared. Using the size function control, a significant amount of effort was used to determine the appropriate element size that fitted within the general rule of the selected mesh quality criterion. It was found that 2.20 mm was the best element size for both gender models. The generated meshes in tetrahedral and hex dominant mesh are shown in Figures 3.18 and 3.19, respectively. It was clear that the tetrahedral mesh method contained more uniform elements compared to the hex dominant mesh method which contained a mix of quads- and triangular-shaped cells. Likewise, when comparing between the latter based on the selected mesh quality criterion, the tetrahedral mesh method fitted within the general rule (see Figure 3.20 for Jacobian ratio and Figure 3.21 for skewness). Thus, it was decided that the tetrahedral mesh method was the best option to employ. Subsequently, all deformed models were meshed using a 2.20 mm element size and tetrahedral mesh method. After meshing, the female face models were discretized with 63 037 elements for advancement flap, rotation flap with 65 221 elements and finally, rhomboid flap with 63 029 elements. Whereas, the male face models were discretized with 64 419 elements, rotation flap with 63 470 elements and finally, rhomboid flap with 62 222 elements. These results are presented in Figures 3.22 to 3.24.



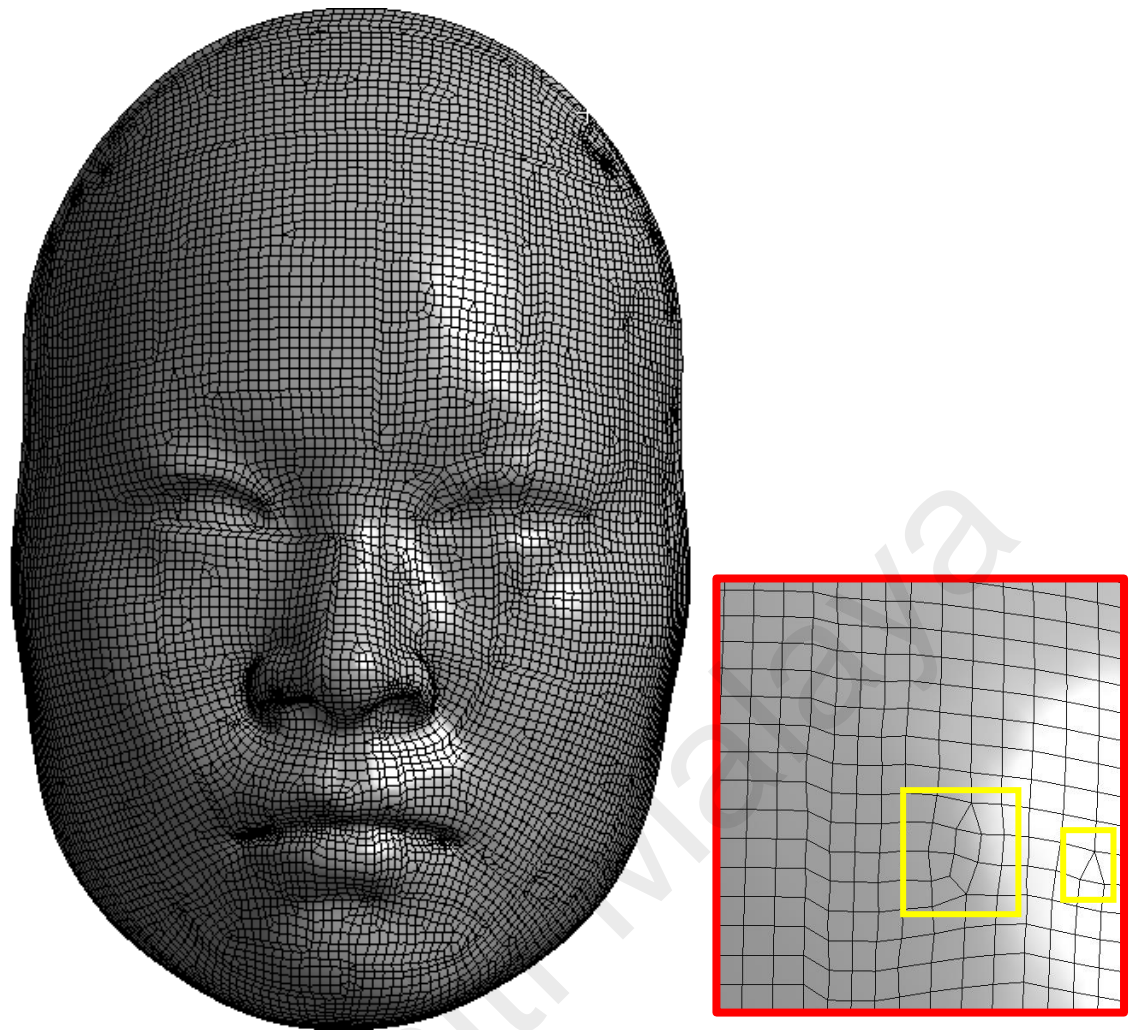
(A)

*Figure 3.18.* Meshed base face model from tetrahedral mesh method. (A) Meshed female face model in full view (left) and close-up view (right) (B) Meshed male face model in full view (left) and at close proximity (right).



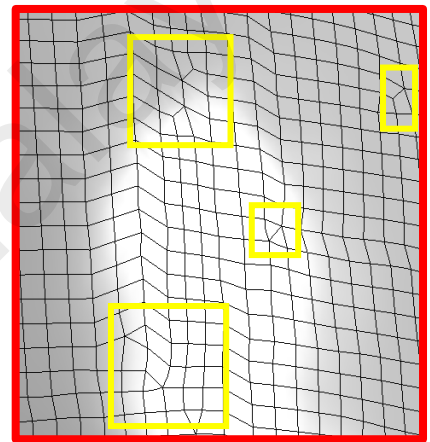
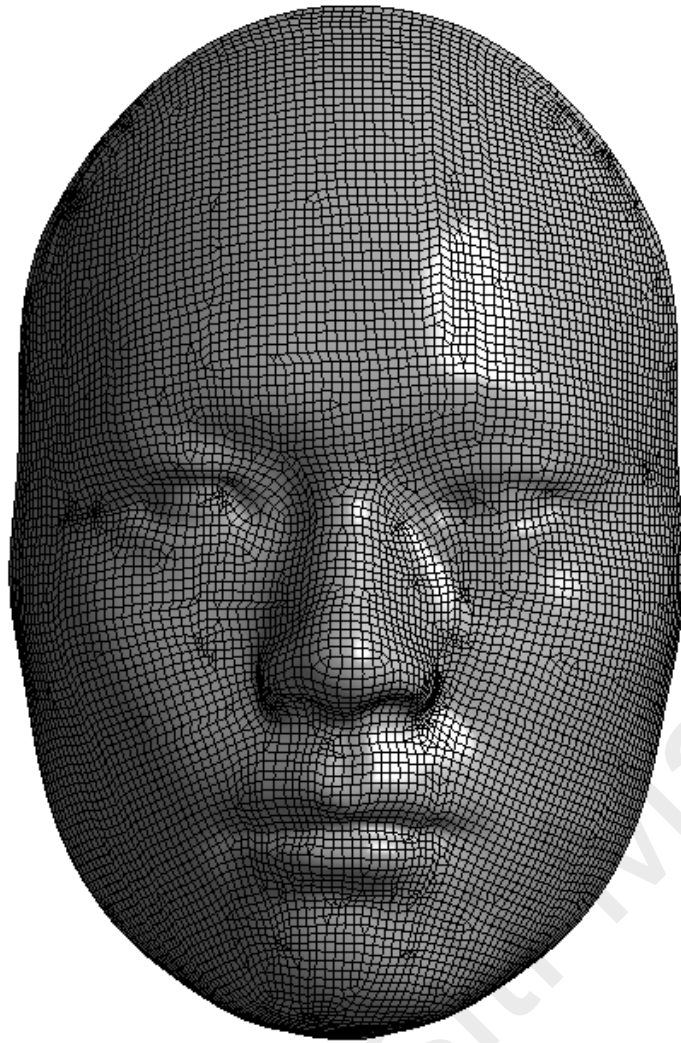
(B)

*Figure 3.18.* Continued.



(A)

**Figure 3.19.** Meshed base face model using the hex dominant mesh method. (A) Meshed female face model in full view (left) and at the close-up view (B) Meshed male face model in full view (left) and at close-up view.



(B)

*Figure 3.19.* Continued.

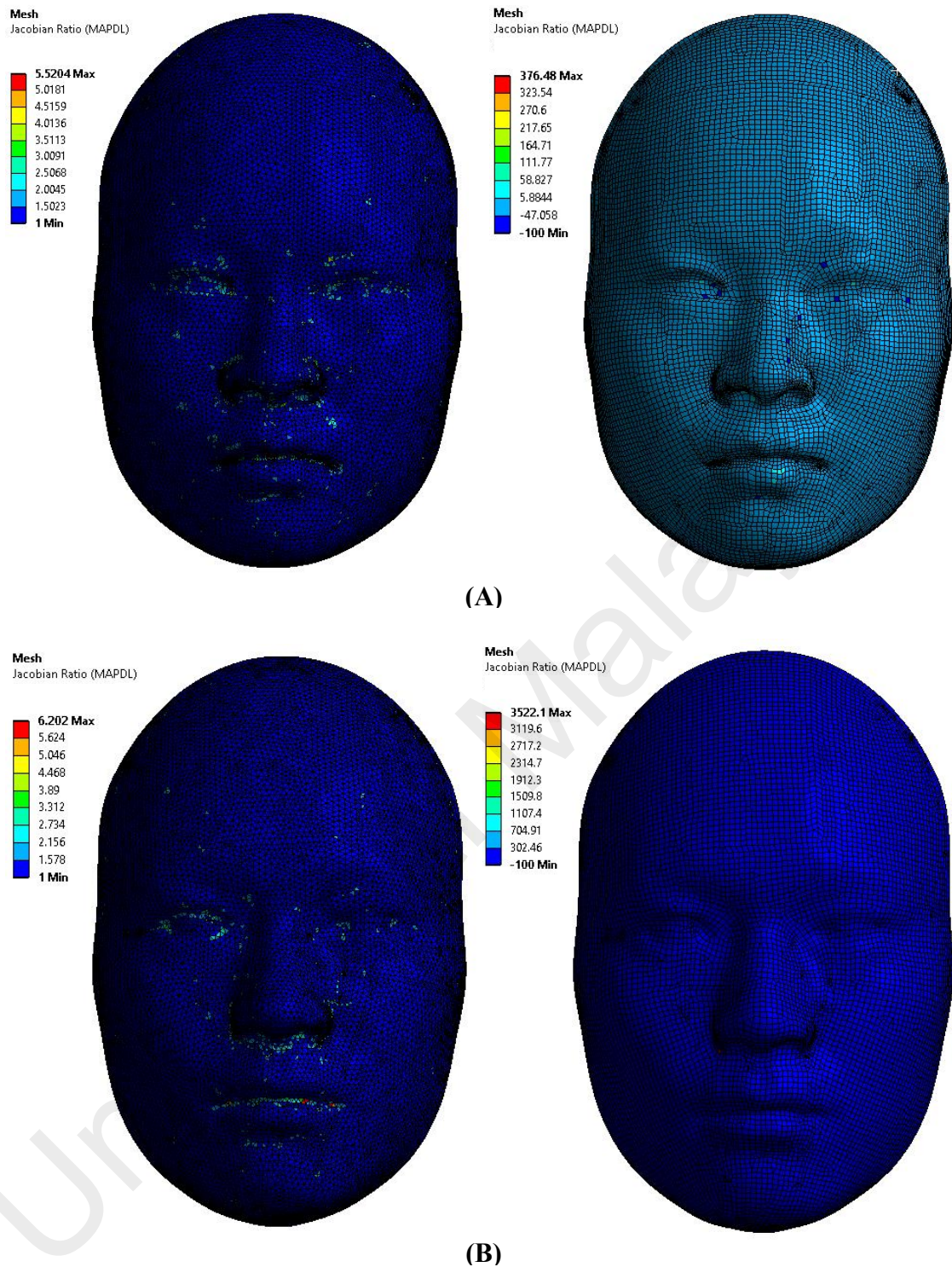
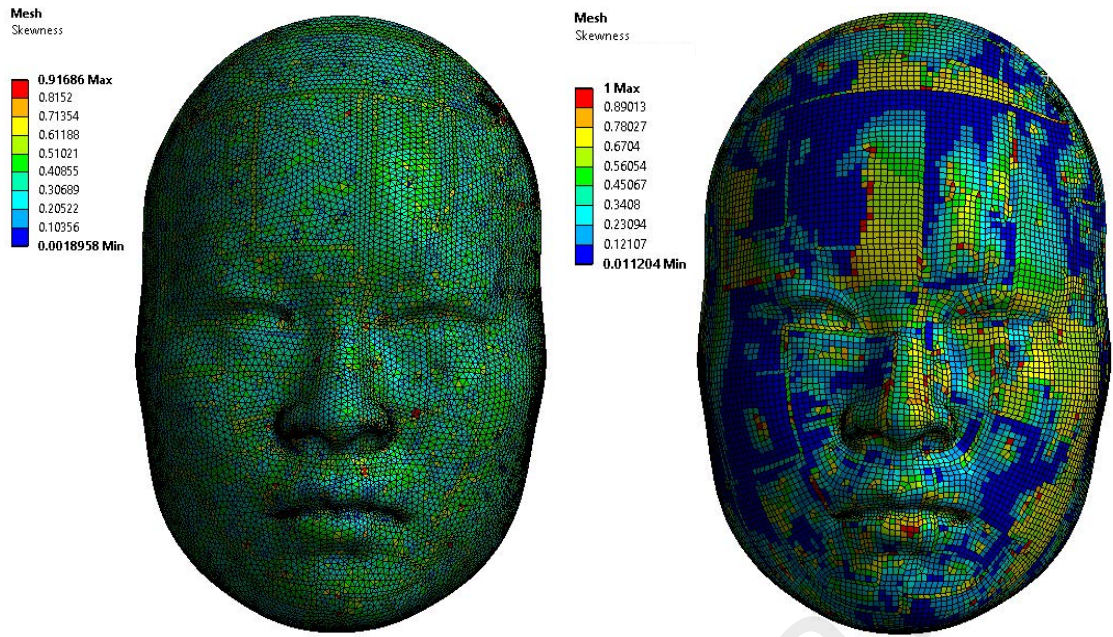
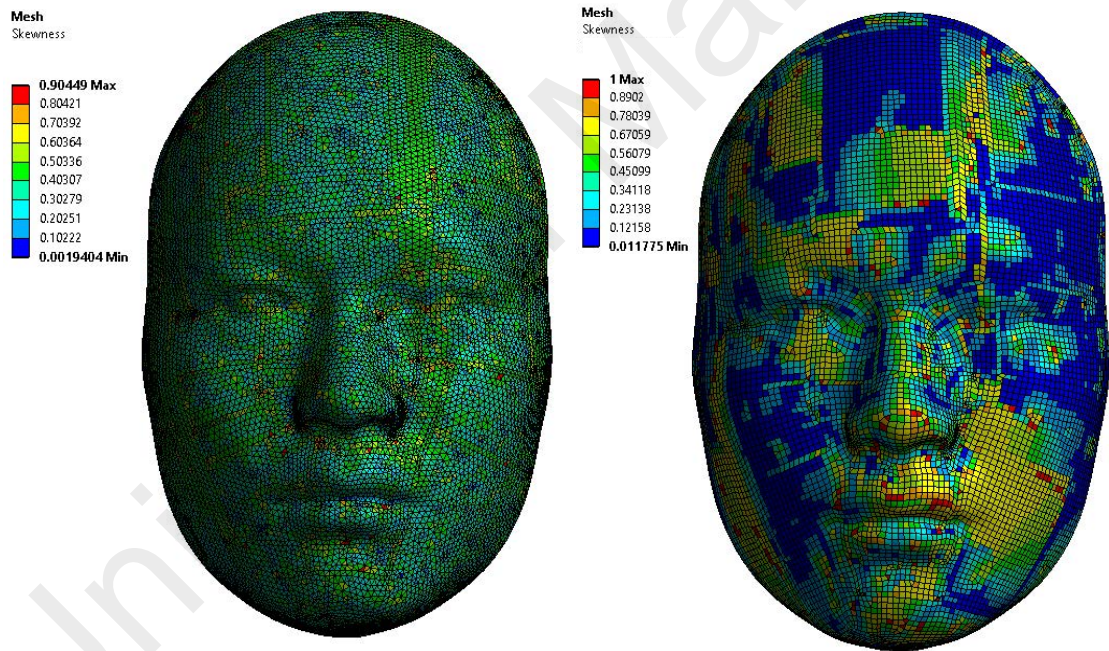


**Figure 3.20.** Tetrahedral method generated the best mesh quality out of Jacobian ratio. **(A)** Meshed female face model in the tetrahedral mesh (left) and hex dominant mesh (right). **(B)** Meshed male face model in the tetrahedral mesh (left) and hex dominant mesh (right)

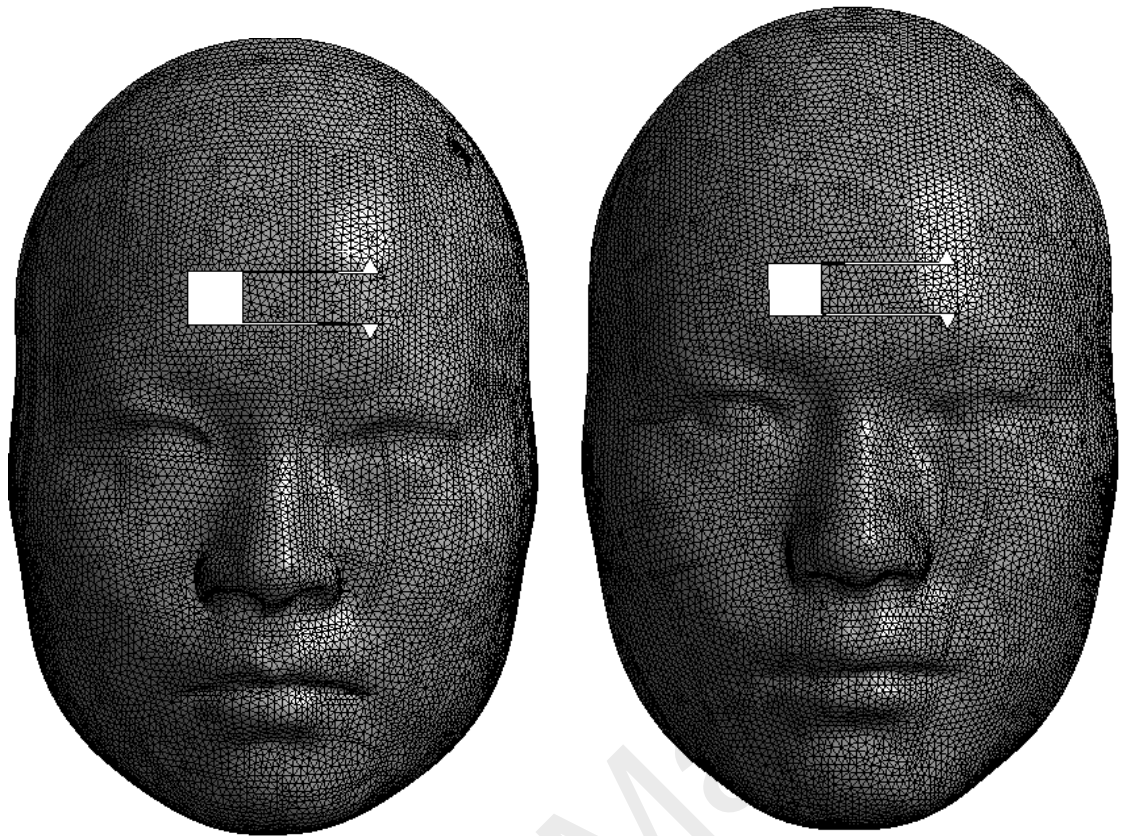


(A)

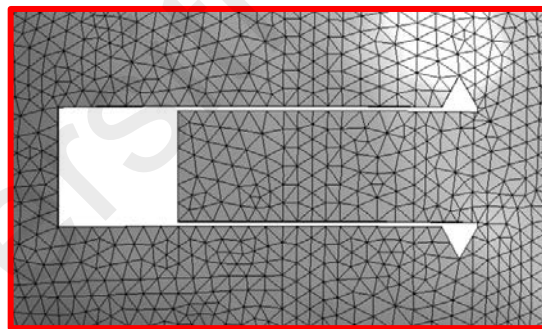


(B)

**Figure 3.21.** Tetrahedral method generated the best mesh quality out of skewness. (A) Meshed female face model in the tetrahedral mesh (left) and hex dominant mesh (right). (B) Meshed male face model in the tetrahedral mesh (left) and hex dominant mesh (right).

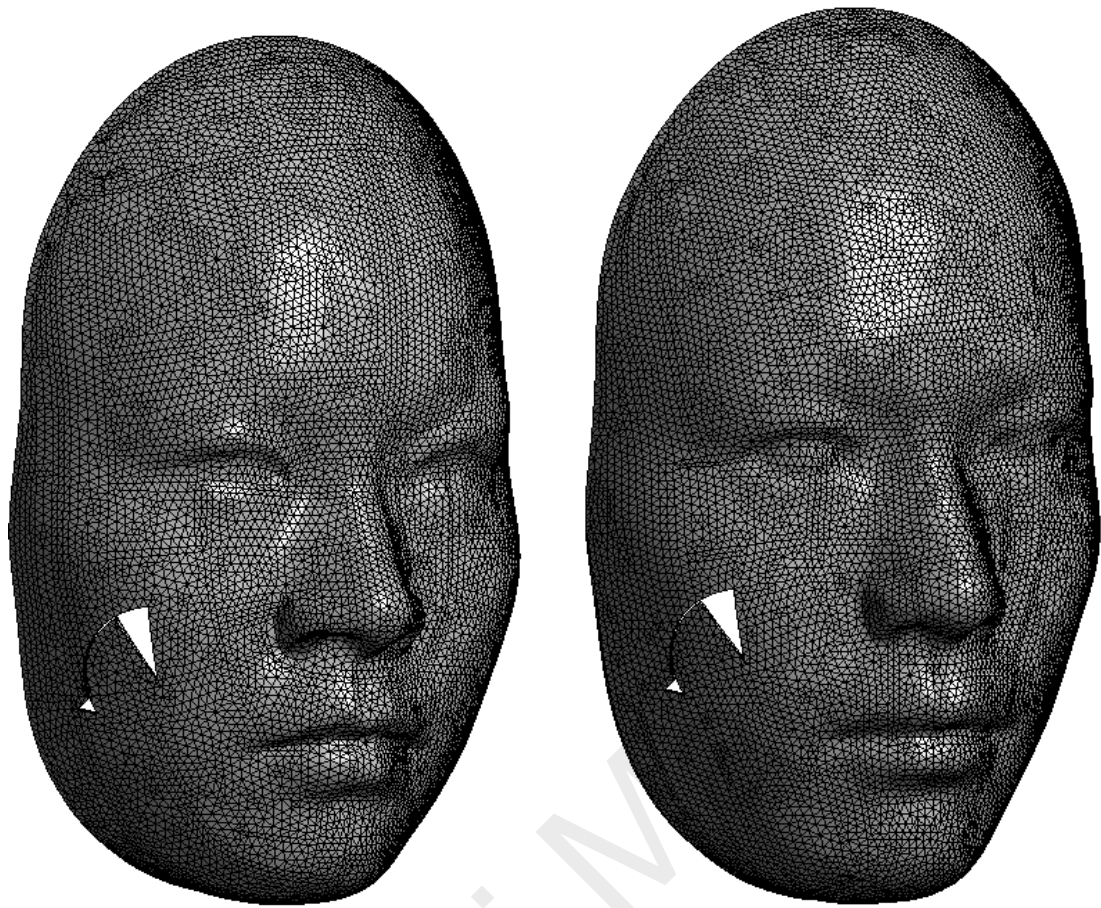


(A)

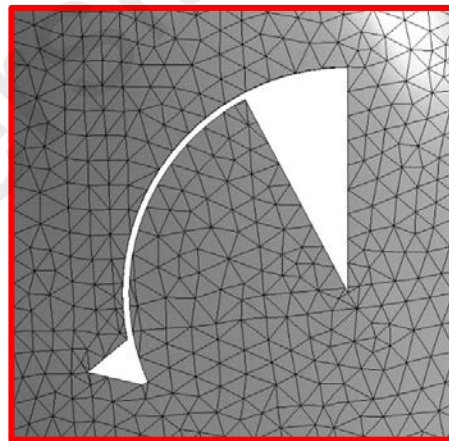


(B)

**Figure 3.22.** Meshed geometries of advancement flap with the tetrahedral mesh assuming that forehead thickness was 1.22 mm and 2.20 mm element size (A) From left to right: female (63 037 elements) and male (64 419 elements) face models. (B) Area of interest at close proximity.



(A)

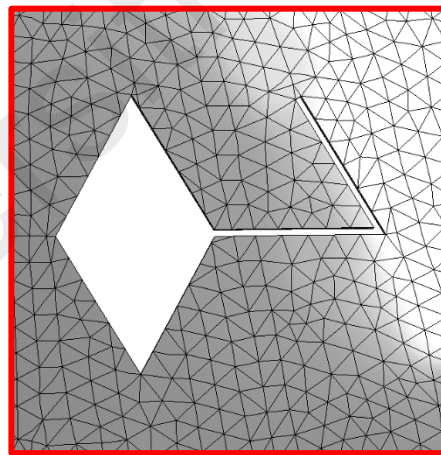


(B)

**Figure 3.23.** Meshed geometries of rotation flap with the tetrahedral mesh assuming that cheek thickness was 1.34 mm and 2.20 mm element size (A) From left to right: female (65 221 elements) and male (63 470 elements) face models. (B) Area of interest at close proximity.



(A)



(B)

**Figure 3.24.** Meshed geometries of the rhomboid flap with the tetrahedral mesh assuming that temple thickness was 1.29 mm and 2.20 mm element size (A) From left to right: female (63 029 elements) and male (62 222 elements) face models. (B) Area of interest at close proximity.

### 3.2.5 Boundary conditions

Separate ‘surfaces from faces’ were pasted underneath the excised surfaces where the latter were treated as no separation and normal Lagrange type contact pairs. This was done to ensure the flap moved according to the face’s curved surface. The separate surfaces were fixed at 1 mm thickness. The outer edges of the face models were held fixed in all directions so that the parts were unable to move.

In closing, distributed displacements were applied along the edges of skin flaps to calculate the post-operative simulation. The displacements were described in X-, Y- and Z-axis direction and X-, Y-, Z-degree rotation (whenever applicable). The action of the skin pulling towards wound closure (directions) and the reported values are tabulated in Table 3.4 (for female face model) and Table 3.5 (for male face model).

**Table 3.4.** A tabulated list of the applied displacements on Asian female model. The arrows show the direction of movement according to the applied values.

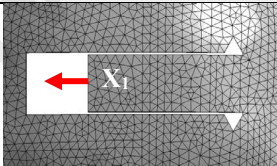
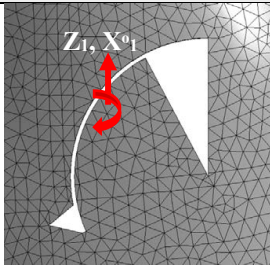
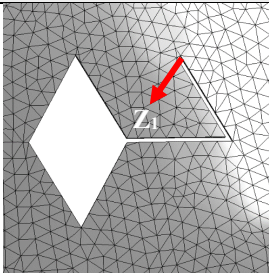
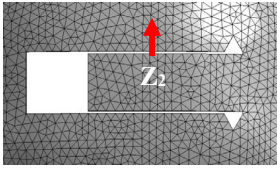
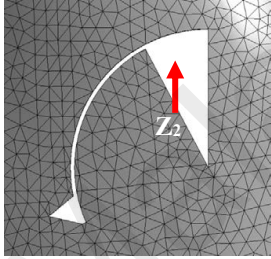
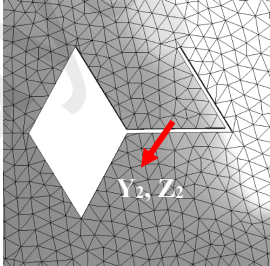
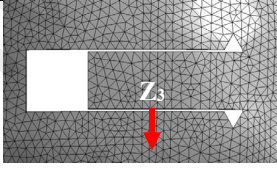
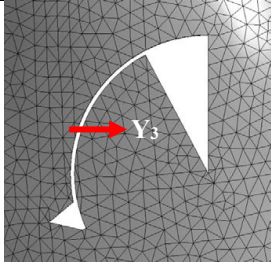
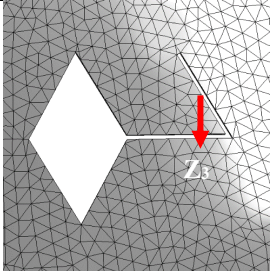
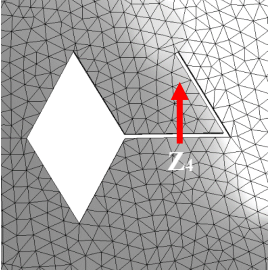
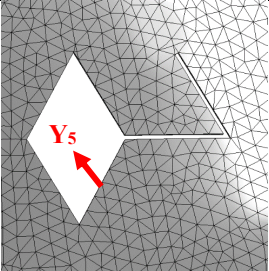
Displacement	Local Flap Design		
	Advancement Flap	Rotation Flap	Rhomboid Flap
Direction-1			

Table 3.4. Continued.

Displacement	Local Flap Design		
	Advancement Flap	Rotation Flap	Rhomboid Flap
	$X_1 = -14.30 \text{ mm}$ $Y_1 = \text{Free}$ $Z_1 = \text{Free}$ Rotation $X_1 = \text{Free}$ Rotation $Y_1 = \text{Free}$ Rotation $Z_1 = \text{Free}$	$X_1 = \text{Free}$ $Y_1 = \text{Free}$ $Z_1 = 6.00 \text{ mm}$ Rotation $X_1 = 20^\circ$ Rotation $Y_1 = \text{Free}$ Rotation $Z_1 = \text{Free}$	$X_1 = \text{Free}$ $Y_1 = 3.00 \text{ mm}$ $Z_1 = -8.50 \text{ mm}$ Rotation $X_1 = \text{Free}$ Rotation $Y_1 = \text{Free}$ Rotation $Z_1 = \text{Free}$
Direction-2	  $X_2 = \text{Free}$ $Y_2 = \text{Free}$ $Z_2 = 1.5 \text{ mm}$ Rotation $X_2 = \text{Free}$ Rotation $Y_2 = \text{Free}$ Rotation $Z_2 = \text{Free}$	  $X_2 = \text{Free}$ $Y_2 = \text{Free}$ $Z_2 = 2.00 \text{ mm}$ Rotation $X_2 = \text{Free}$ Rotation $Y_2 = \text{Free}$ Rotation $Z_2 = \text{Free}$	  $X_2 = \text{Free}$ $Y_2 = 13.50 \text{ mm}$ $Z_2 = -7.10 \text{ mm}$ Rotation $X_2 = \text{Free}$ Rotation $Y_2 = \text{Free}$ Rotation $Z_2 = \text{Free}$
Direction-3	  $X_3 = \text{Free}$ $Y_3 = \text{Free}$ $Z_3 = -1.50 \text{ mm}$ Rotation $X_3 = \text{Free}$ Rotation $Y_3 = \text{Free}$ Rotation $Z_3 = \text{Free}$	  $X_3 = \text{Free}$ $Y_3 = -1.00 \text{ mm}$ $Z_3 = \text{Free}$ Rotation $X_3 = \text{Free}$ Rotation $Y_3 = \text{Free}$ Rotation $Z_3 = \text{Free}$	  $X_3 = \text{Free}$ $Y_3 = \text{Free}$ $Z_3 = -9.80 \text{ mm}$ Rotation $X_3 = \text{Free}$ Rotation $Y_3 = \text{Free}$ Rotation $Z_3 = \text{Free}$

**Table 3.4.** Continued.

Displacement	Local Flap Design		
	Advancement Flap	Rotation Flap	Rhomboid Flap
Direction-4			 <p> <math>X_4 = \text{Free}</math>  <math>Y_4 = \text{Free}</math>  <math>Z_4 = 4.00 \text{ mm}</math>                      Rotation <math>X_4 = \text{Free}</math>                      Rotation <math>Y_4 = \text{Free}</math>                      Rotation <math>Z_4 = \text{Free}</math> </p>
Direction-5			 <p> <math>X_5 = \text{Free}</math>  <math>Y_5 = 0.10 \text{ mm}</math>  <math>Z_5 = \text{Free}</math>                      Rotation <math>X_5 = \text{Free}</math>                      Rotation <math>Y_5 = \text{Free}</math>                      Rotation <math>Z_5 = \text{Free}</math> </p>

**Table 3.5.** A tabulated list of the applied displacements on Asian male model. The arrows show the direction of movement according to the applied values.

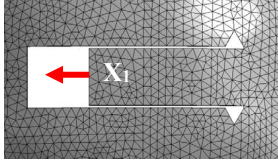
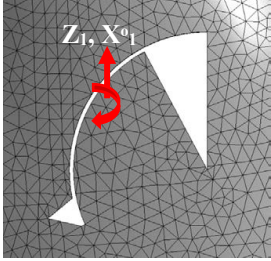
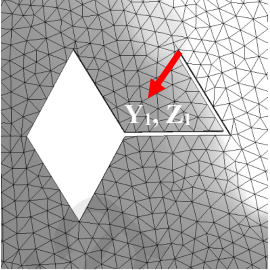
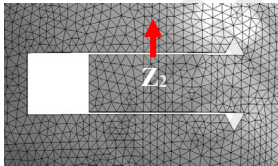
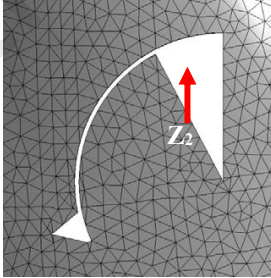
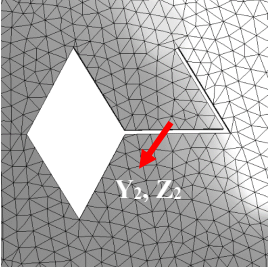
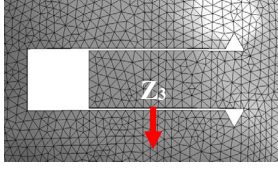
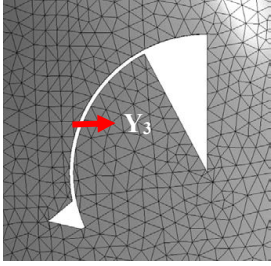
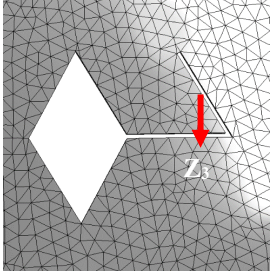
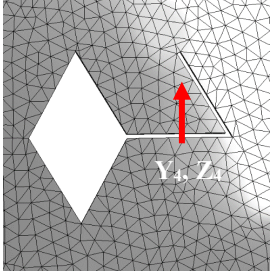
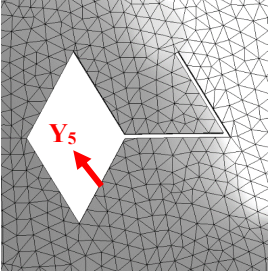
Displacement	Local Flap Design		
	Advancement Flap	Rotation Flap	Rhomboid Flap
Direction-1	 <p> <math>X_1 = -14.80 \text{ mm}</math>  <math>Y_1 = \text{Free}</math>  <math>Z_1 = \text{Free}</math>                      Rotation <math>X_1 = \text{Free}</math>                      Rotation <math>Y_1 = \text{Free}</math>                      Rotation <math>Z_1 = \text{Free}</math> </p>	 <p> <math>X_1 = \text{Free}</math>  <math>Y_1 = \text{Free}</math>  <math>Z_1 = 6.50 \text{ mm}</math>                      Rotation <math>X_1 = 18^\circ</math>                      Rotation <math>Y_1 = \text{Free}</math>                      Rotation <math>Z_1 = \text{Free}</math> </p>	 <p> <math>X_1 = \text{Free}</math>  <math>Y_1 = 3.00 \text{ mm}</math>  <math>Z_1 = -7.00 \text{ mm}</math>                      Rotation <math>X_1 = \text{Free}</math>                      Rotation <math>Y_1 = \text{Free}</math>                      Rotation <math>Z_1 = \text{Free}</math> </p>
Direction-2	 <p> <math>X_2 = \text{Free}</math>  <math>Y_2 = \text{Free}</math>  <math>Z_2 = 0.30 \text{ mm}</math>                      Rotation <math>X_2 = \text{Free}</math>                      Rotation <math>Y_2 = \text{Free}</math>                      Rotation <math>Z_2 = \text{Free}</math> </p>	 <p> <math>X_2 = \text{Free}</math>  <math>Y_2 = \text{Free}</math>  <math>Z_2 = 1.00 \text{ mm}</math>                      Rotation <math>X_2 = \text{Free}</math>                      Rotation <math>Y_2 = \text{Free}</math>                      Rotation <math>Z_2 = \text{Free}</math> </p>	 <p> <math>X_2 = \text{Free}</math>  <math>Y_2 = 13.80 \text{ mm}</math>  <math>Z_2 = -7.50 \text{ mm}</math>                      Rotation <math>X_2 = \text{Free}</math>                      Rotation <math>Y_2 = \text{Free}</math>                      Rotation <math>Z_2 = \text{Free}</math> </p>

Table 3.5. Continued.

Displacement	Local Flap Design		
	Advancement Flap	Rotation Flap	Rhomboid Flap
Direction-3	 <p> <math>X_3 = \text{Free}</math>  <math>Y_3 = \text{Free}</math>  <math>Z_3 = -0.30 \text{ mm}</math>                      Rotation <math>X_3 = \text{Free}</math>                      Rotation <math>Y_3 = \text{Free}</math>                      Rotation <math>Z_3 = \text{Free}</math> </p>	 <p> <math>X_3 = \text{Free}</math>  <math>Y_3 = -1.00 \text{ mm}</math>  <math>Z_3 = \text{Free}</math>                      Rotation <math>X_3 = \text{Free}</math>                      Rotation <math>Y_3 = \text{Free}</math>                      Rotation <math>Z_3 = \text{Free}</math> </p>	 <p> <math>X_3 = \text{Free}</math>  <math>Y_3 = \text{Free}</math>  <math>Z_3 = -9.50 \text{ mm}</math>                      Rotation <math>X_3 = \text{Free}</math>                      Rotation <math>Y_3 = \text{Free}</math>                      Rotation <math>Z_3 = \text{Free}</math> </p>
Direction-4			 <p> <math>X_4 = \text{Free}</math>  <math>Y_4 = -1.00 \text{ mm}</math>  <math>Z_4 = 5.50 \text{ mm}</math>                      Rotation <math>X_4 = \text{Free}</math>                      Rotation <math>Y_4 = \text{Free}</math>                      Rotation <math>Z_4 = \text{Free}</math> </p>

**Table 3.5.** Continued.

Displacement	Local Flap Design		
	Advancement Flap	Rotation Flap	Rhomboid Flap
Direction-5			 <p> <math>X_5 = \text{Free}</math>  <math>Y_5 = 0.10 \text{ mm}</math>  <math>Z_5 = \text{Free}</math>                      Rotation <math>X_5 = \text{Free}</math>                      Rotation <math>Y_5 = \text{Free}</math>                      Rotation <math>Z_5 = \text{Free}</math> </p>

### 3.2.6 Assumptions on the FE analysis model

The assumptions made in the present work were similar to Case Study 1 with an extension of limited options for Asian and gender simulation. The extended assumptions are listed as follows:

- 1) Although different ethnicities and genders were examined, all of them were defined using the same material properties and thickness values while acknowledging that the said parameters were completely varied between individuals. The simulations used normalizing factors without taking into account gender differences with notable acceptance of below 20% differences (*Benítez & Montáns, 2017; L.O. Olsen et al., 1995; Querleux et al., 2009*) for both material properties and thickness.

2) The data used were mostly adopted from the literature since deriving the data from experimental studies required expertise and approval from various parties. Hence, relevant data, especially for Asians, were limited.

Universiti Malaya

## CHAPTER 4

### NUMERICAL RESULT

This chapter presents the findings from the post-operative simulations. Equivalent von Mises stress was utilized to describe the flap tension after closure. Post-operative simulation displayed a variety of colors that were mapped over the models where each of the colors was arranged in a spectrum according to a set of range values. The contour spectrum around the closed-form defect areas illustrated the peak closure tension in which blue-, green-, and red-colored to represent minimum, medium, and maximum stress values, respectively. Generally, the blue-colored contour illustrated that the skin was in a relaxation state and up to the red-colored contour indicated that the skin experienced its maximum stretches. Noted that the equivalent stress values resulted from the local flap closures were forecasted with no justified values and they were used to indicate the stress comparison between genders for this study.

#### 4.1 Case Study 1: Caucasian Model

Figure 4.1 demonstrated the motion of local flaps designs from initial posture to final closure. Each of the local flaps was advanced according to their method of movement.

The advancement flap was seen to stretch forward until it covered the excised area. The color spectrum indicated the amount of elongation experienced by the flap which led to thickness thinning. Since the load applications followed the tensile stress theory, it seemed logical that the furthest part from the stretching area would experience a more relaxed state (from light blue- to yellow-colored contour). However, stress was found to

be more concentrated at one side of lateral corners near the Burow's triangles with maximal stress of 23.63 MPa. The stress distribution and maximal stress position of the advancement flap closure can be seen in Figure 4.2.

Meanwhile, the rotation flap was seen to advance under the damaged area in rotational motion. As the angle of rotation increases, the contour spectrum gradually tones down from a red-colored contour (started at the tip of Burow's triangle) to a blue-colored contour, which implies relief from the deforming stress. Moreover, stress can be seen concentrated along the distal border of the flap with a value of 150.57 MPa. Figure 4.3 showcased the stress distribution as well as the location of the maximal stress incurred during the rotation flap closure.

The rhomboid flap, likewise, moved in rotational motion from the 120° side to the 60° side to execute the primary closure. In Figure 4.4, maximal stress was concentrated at the point of the rhombus edge adjacent to the primary closure with a value of 302.97 MPa. The stress spread upward yet tamed (from red- to light blue-colored contour) which indicated the relaxation of tissues from tension to a composed state.

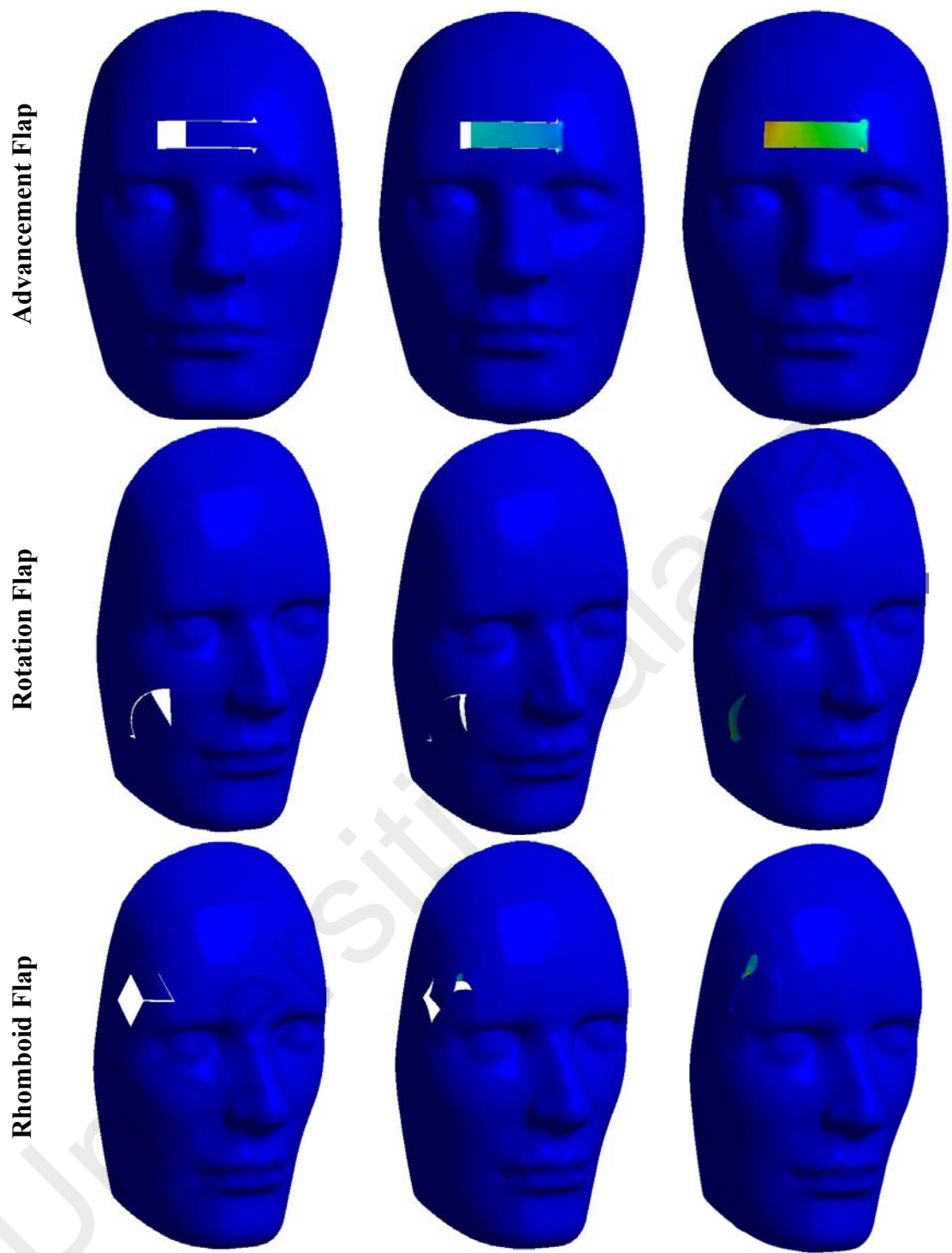


*Figure 4.1.* Sequential steps of closed-form simulations of advancement, rotation, and rhomboid flaps for the Caucasian face model are shown from left to right.

**A: Static Structural**  
Equivalent Stress  
Type: Equivalent (von-Mises) Stress  
Unit: MPa

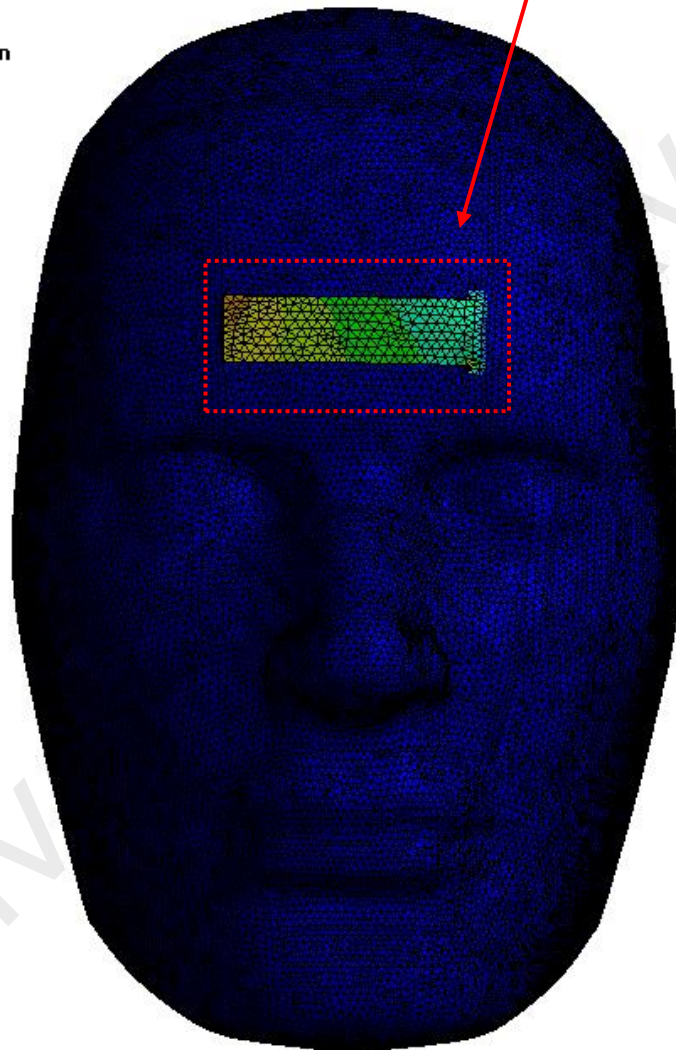
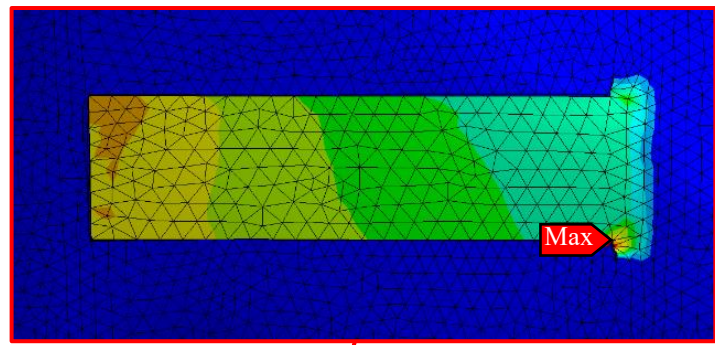
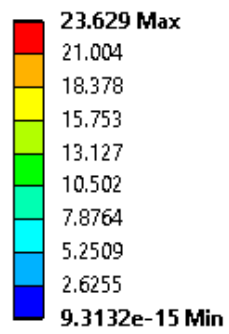


**Figure 4.2.** Advancement flap closure on the Caucasian face model. Maximal von Mises stress concentrated on one side of lateral corners.

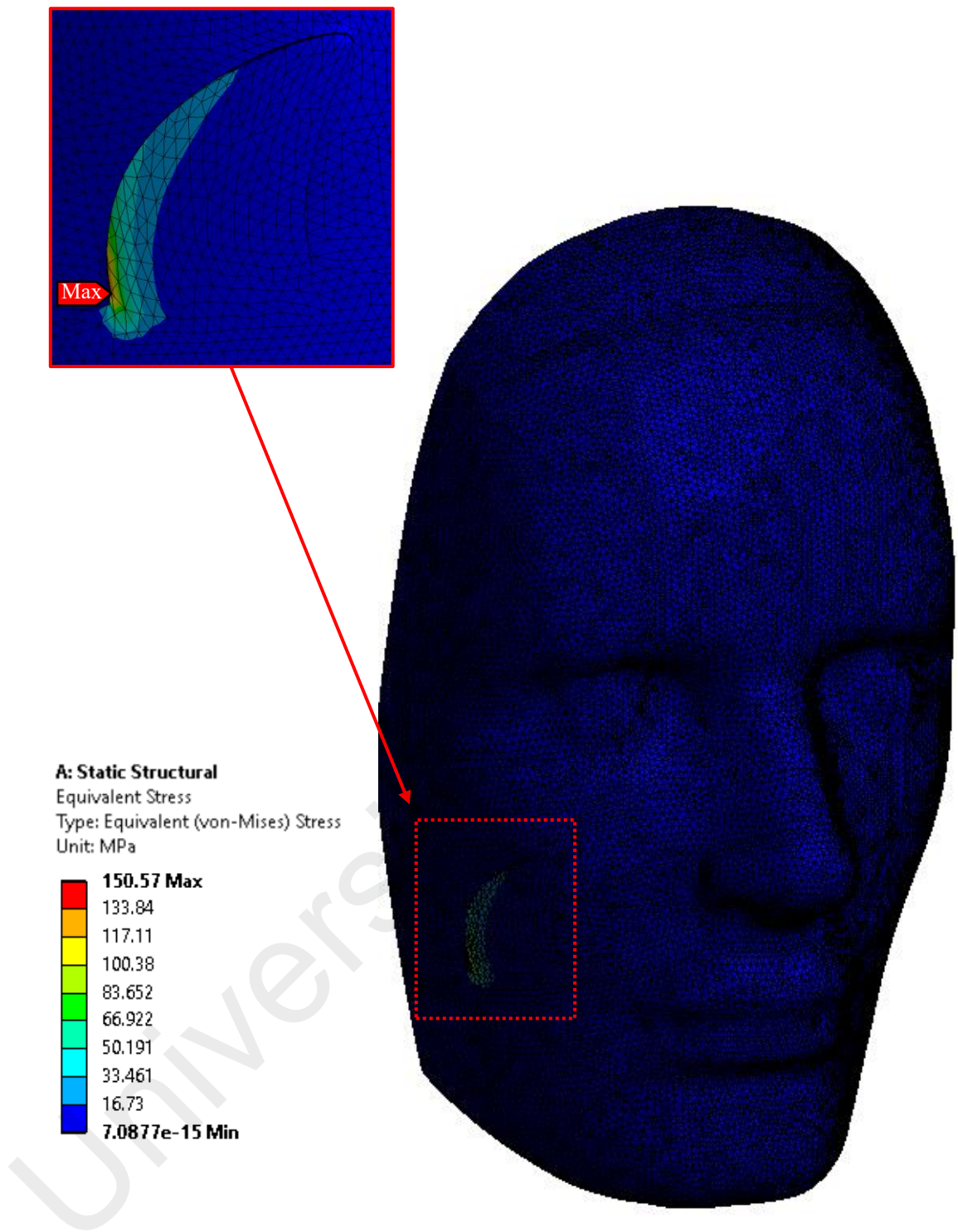


*Figure 4.3.* Rotation flap closure on the Caucasian face model. Maximal von Mises stress concentrated along the distal border of the flap.

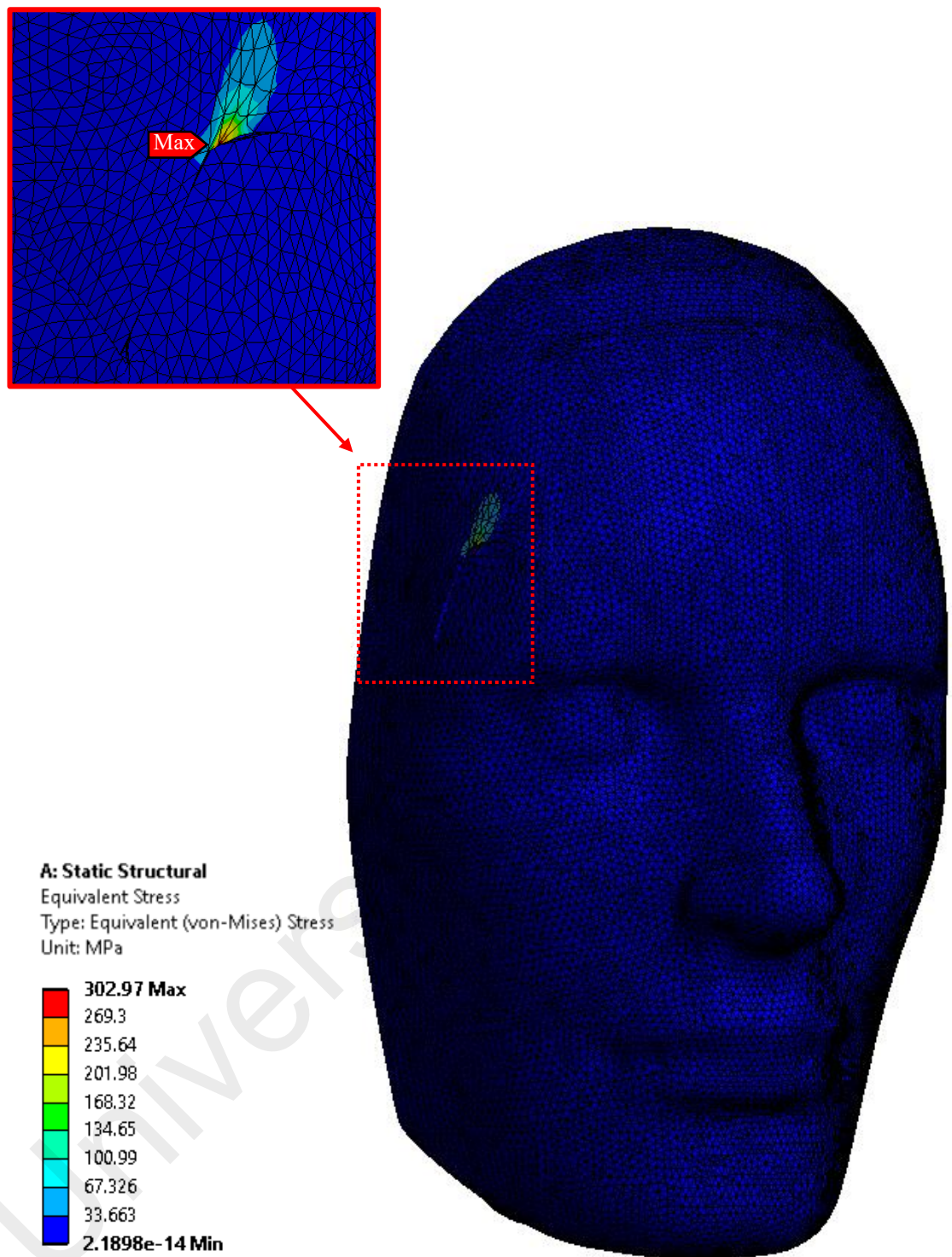


*Figure 4.4.* Rhomboid flap closure on the Caucasian face model. Maximal von Mises stress concentrated at the point of the edges of the rhombus adjacent to the primary defect closure.

## 4.2 Case Study 2: Asian Models

Closed-form solution of local flap surgery from initial posture until final closure was further shown in Figures 4.5 and 4.6. It can be seen that each of the local flaps moves toward the boundary of the defect consistent with their respective method of movement.

Advancement flaps were seen to move directly forward without any rotational movement in the forehead area. When subjected to tension, the amount of skin elongated along the incision border produced a stress distribution where the color spectrum indicated that the skin experienced a decrease in thickness that led to thinning due to the high degree of skin stretching. The displayed color spectrum varied in genders as the female showed a soothe stress distribution (light blue- to green-colored contour) compared to the male (light blue- to yellow- colored contour). However, both genders indicated a rational skin stretching where the stress is distributed from the lowest to the highest rank in the color code starting from the right to left. Moreover, the displacement of the maximal stress contrasted between the latter. Stress was found concentrated at the top vertical of Burow's triangle with maximal von Mises stress of 33.79 MPa in the female face model (see Figure 4.7). Whereas, in the male face model, this was conversely concentrated at the border of incision lines with 78.94 MPa (see Figure 4.8).

Rotation flaps were seen rotating along the flap arc with an eye towards the triangular-shaped defect at the cheek area. As the amount of the arc rotation increased, stresses were revealed to be concentrated at the distal end of the flaps. This showed that the tip of the distal end experienced maximum stretching while enduring skin thinning. However, the contour tones down gradually around the incision length, indicating the relief from the deforming stress (from red- to light blue-colored contour). Aside from that, the stress distribution between the opposite genders was found to be relatively

similar despite the differences in the maximal stress values. Figures 4.9 and 4.10 presented a closed-view of rotation flap with 32.82 MPa in the female face model and 60.19 MPa in the male face model, respectively.

A rhomboid flap was designed to cover the 60° and 120° of the rhombus-shaped defect at the temple area. The flap was seen oriented from the 120° side and extended toward the 60° side. Similar to the rotation flap scenario, both of the opposite genders demonstrated relatively identical stress distribution as well as the maximal stress location. Stress was concentrated at the point of rhombus edge adjacent to the primary defect closure and gradually toned down (from red- to light blue-colored contour). The contour spreading indicated the relaxation of tissues from tension to a composed condition. Corresponding to the maximal stresses, the male face model displayed higher stress with 431.28 MPa (see Figure 4.12) compared to the female face model with 207.19 MPa (see Figure 4.11).

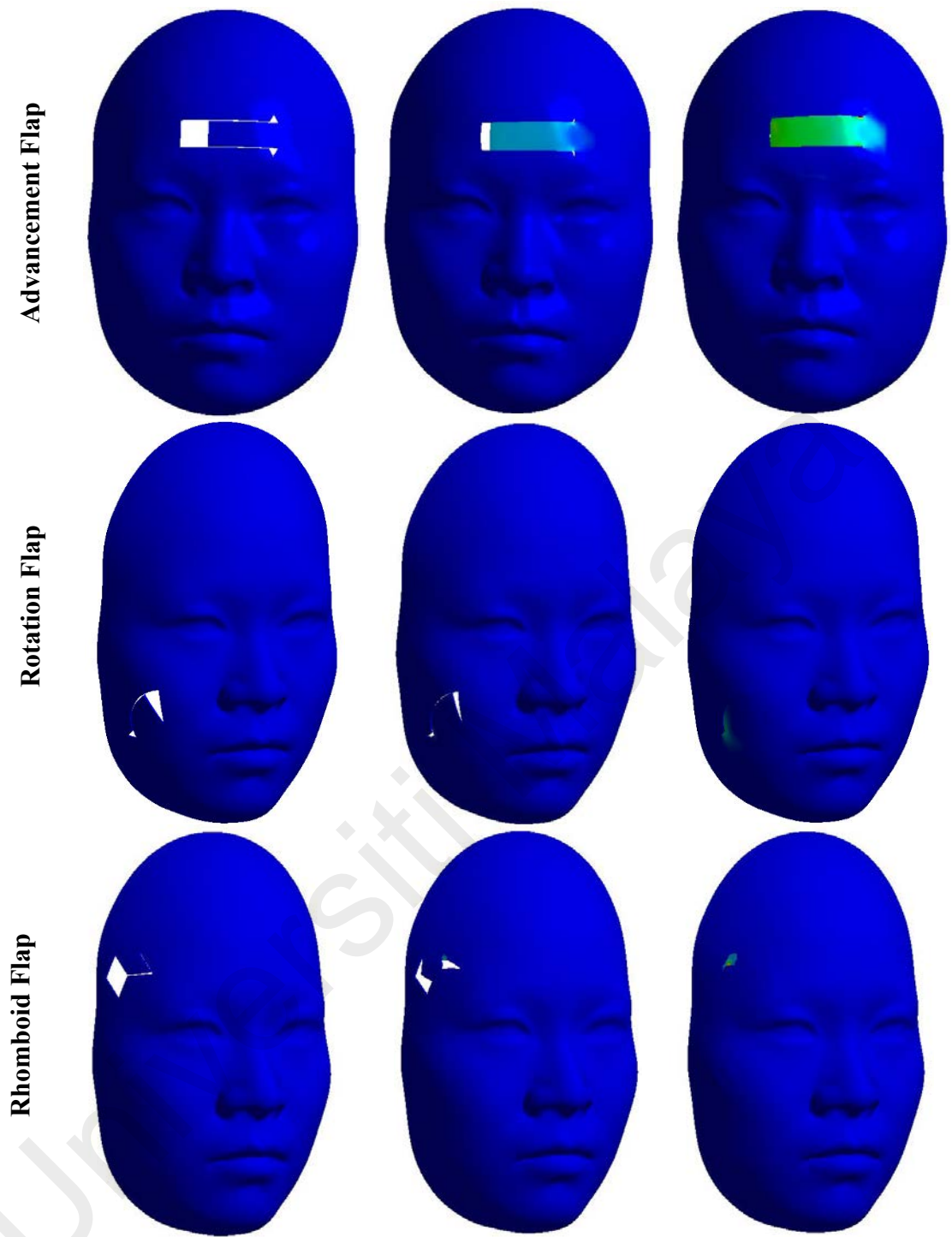


*Figure 4.5.* Sequential steps of closed-form simulations of advancement, rotation, and rhomboid flaps for Asian female are shown from left to right.

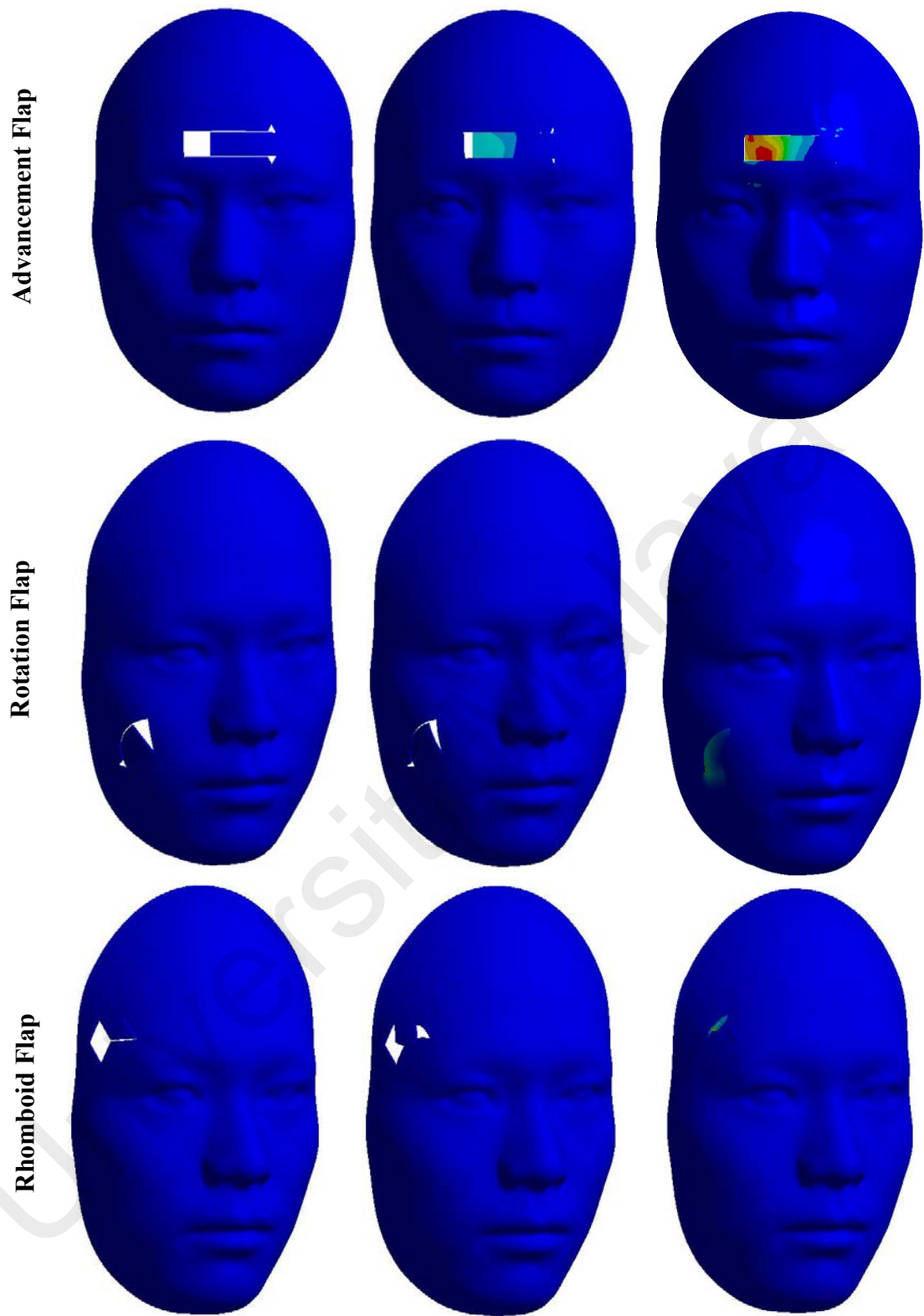


*Figure 4.6.* Sequential steps of closed-form simulations of advancement, rotation, and rhomboid flaps for the Asian male face model are shown from left to right.

**A: Static Structural**  
Equivalent Stress  
Type: Equivalent (von-Mises) Stress  
Unit: MPa

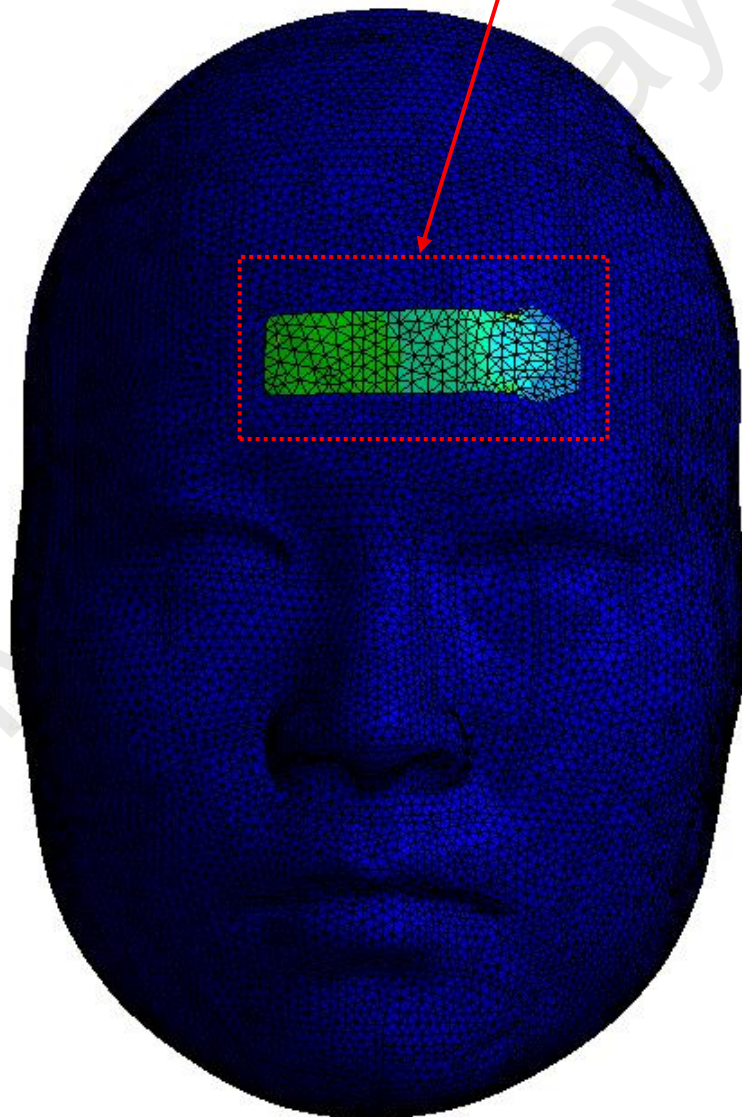
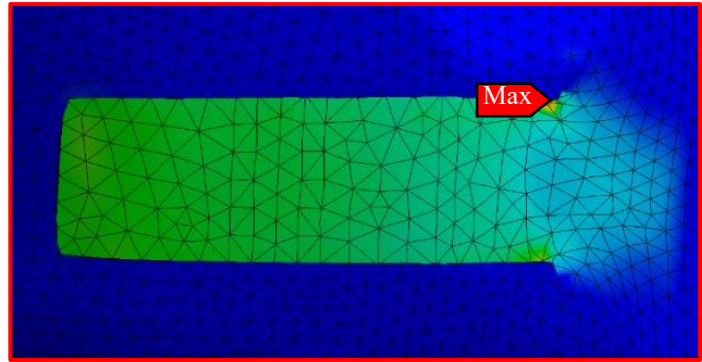
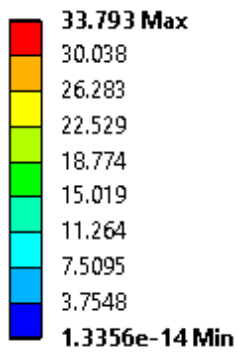


**Figure 4.7.** Advancement flap closure on the Asian female face model. Maximal von Mises stress concentrated on one side of lateral corners.

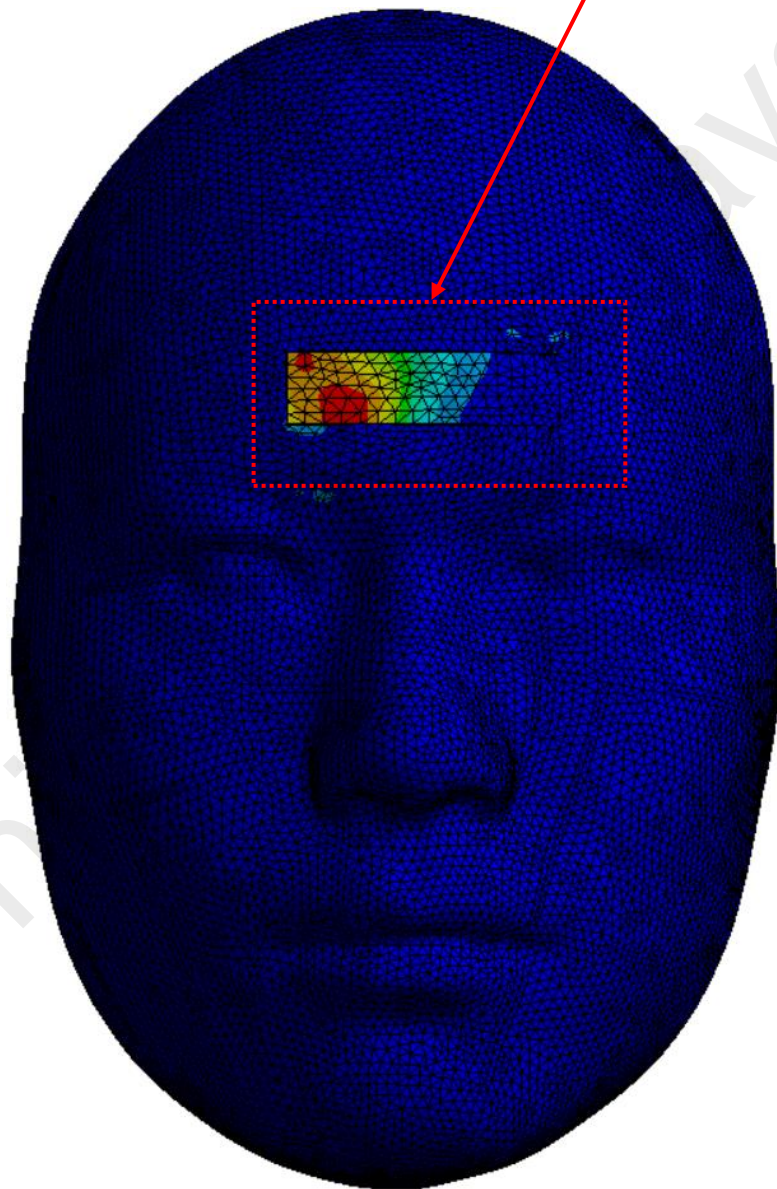
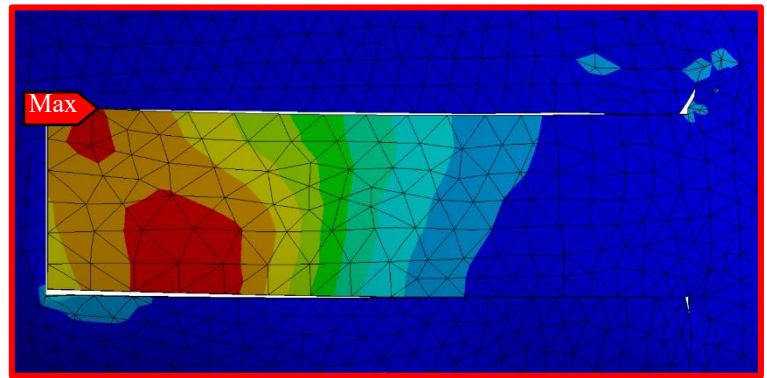
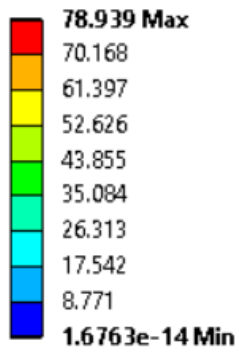


*Figure 4.8.* Advancement flap closure on a male face model. Maximal von Mises concentrated at the border of the incision lines.

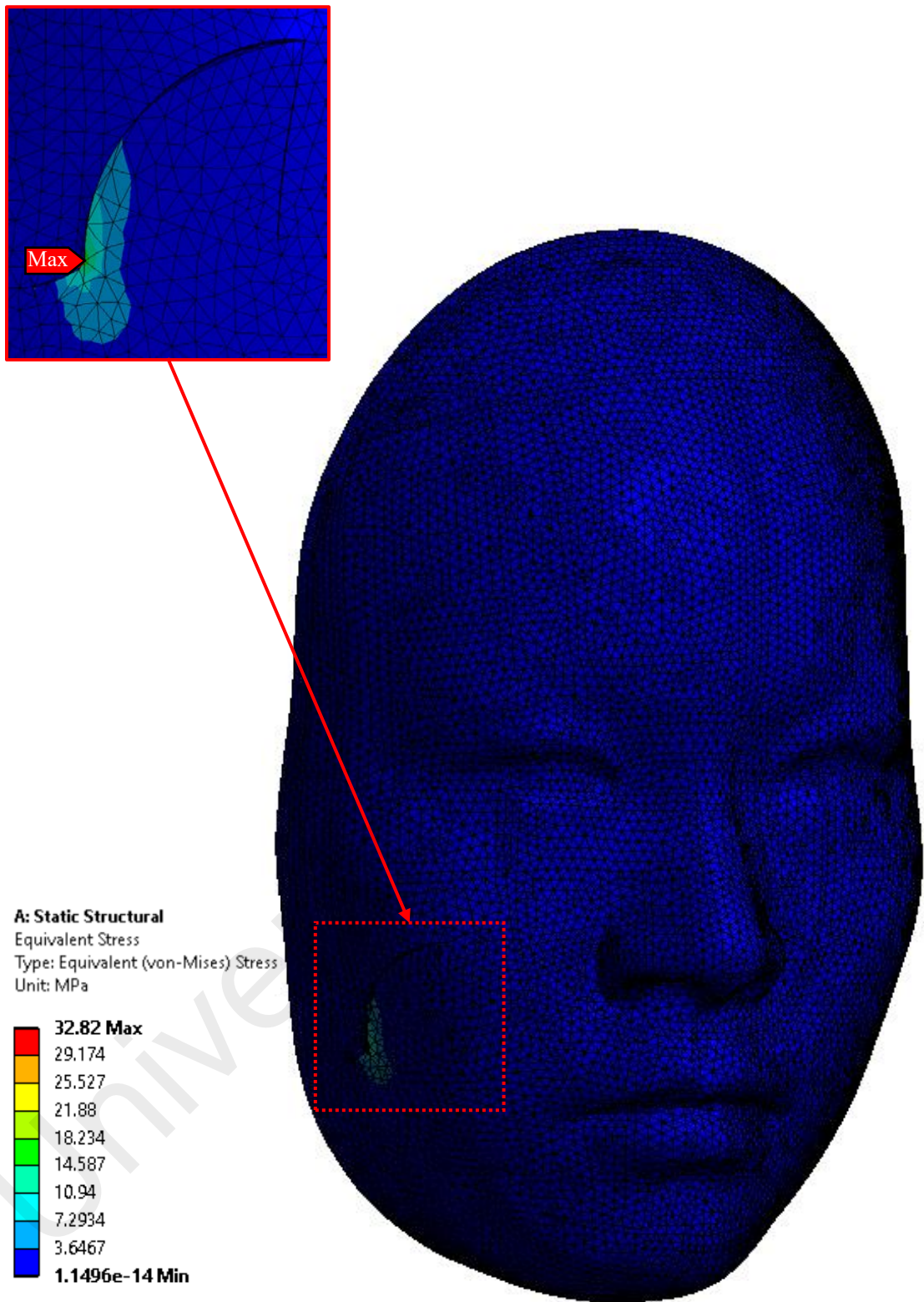


*Figure 4.9.* Rotation flap closure on the Asian female face model. Maximal von Mises stress concentrated at the tip of Burow’s triangle.

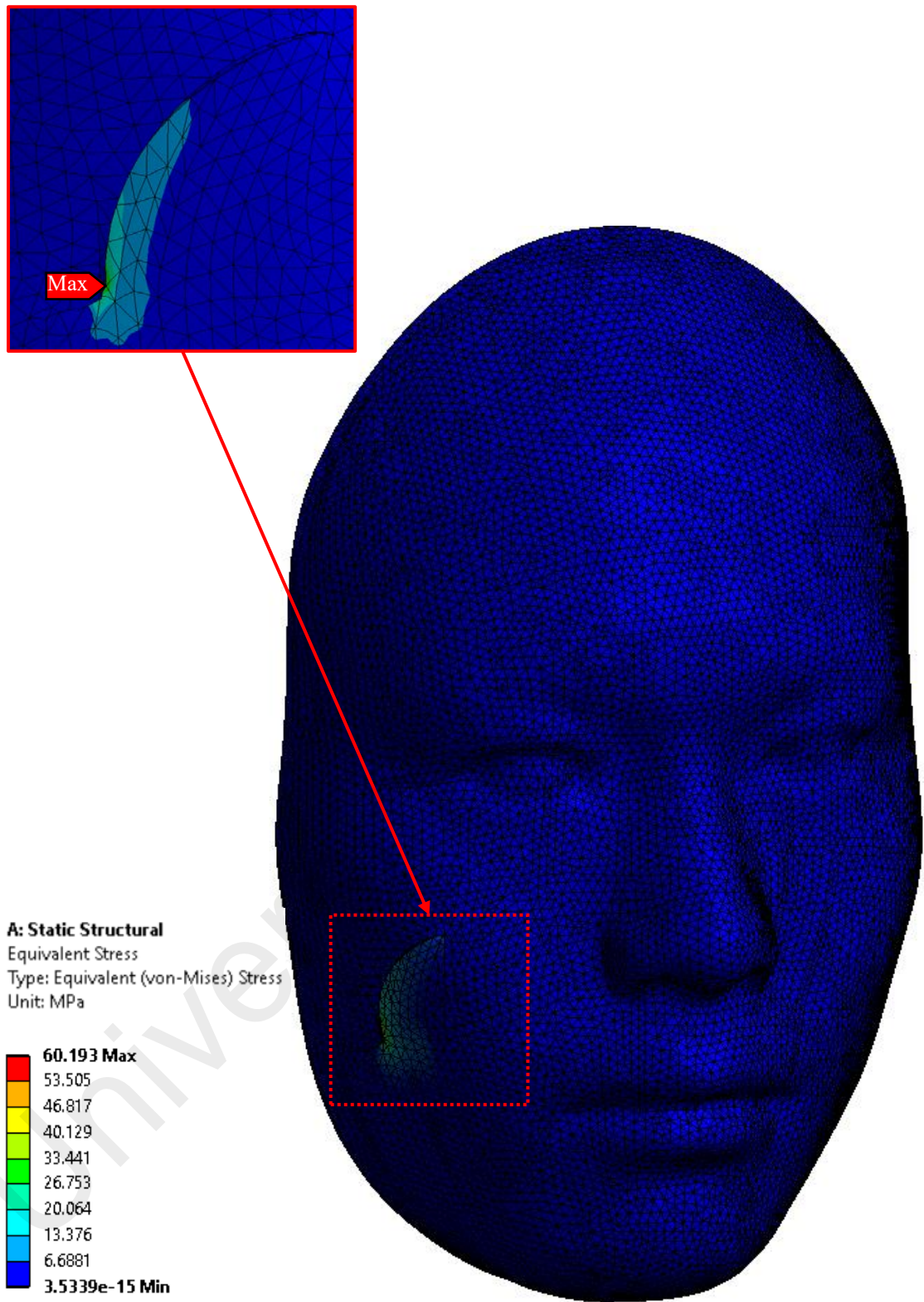


*Figure 4.10.* Rotation flap closure on a male face model. Maximal von Mises stress concentrated at the tip of Burow's triangle.

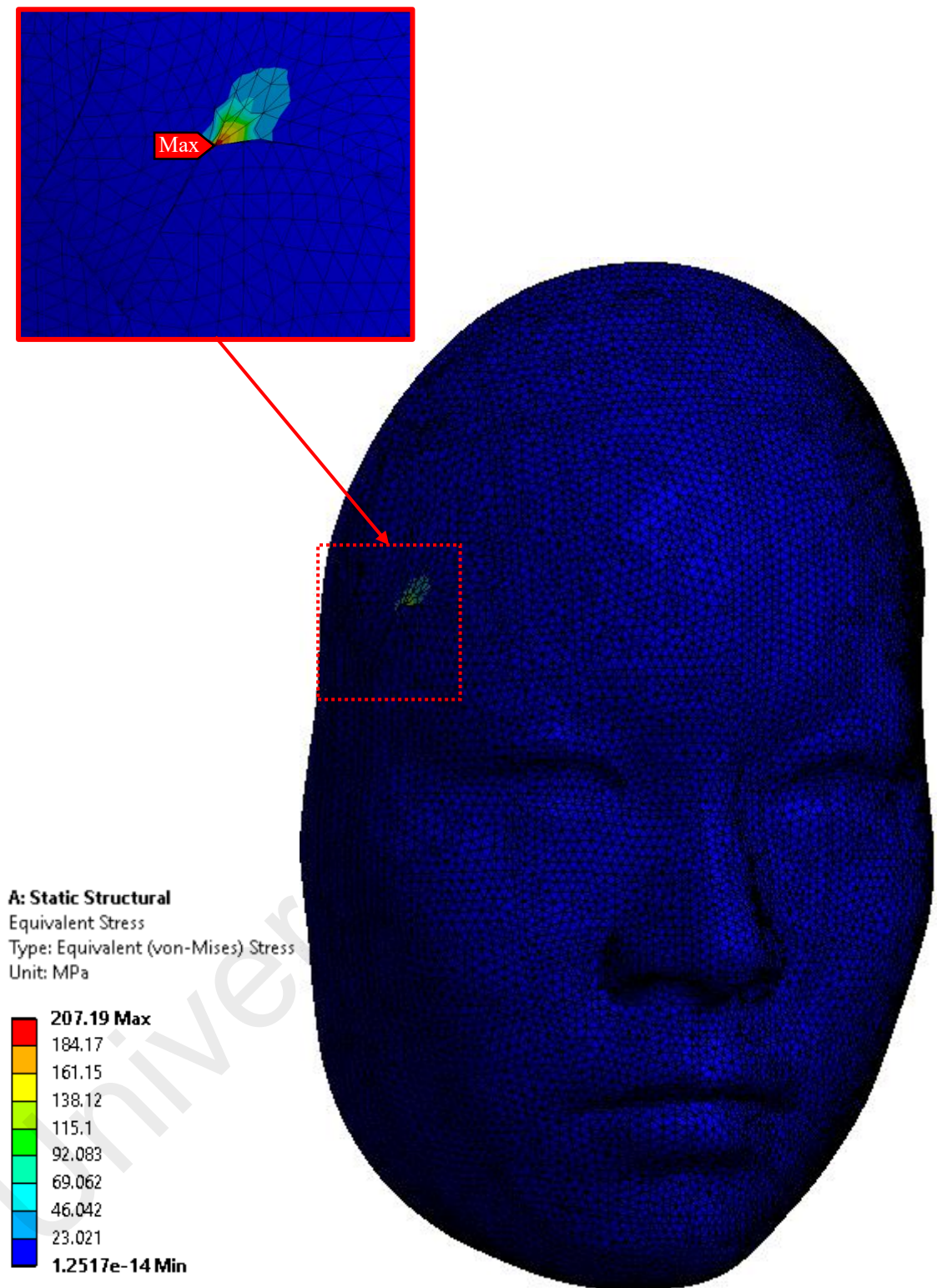


*Figure 4.11.* Rhomboid flap closure on the Asian female face model. Maximal von Mises stress concentrated at the point of rhombus edges adjacent to the primary defect closure.

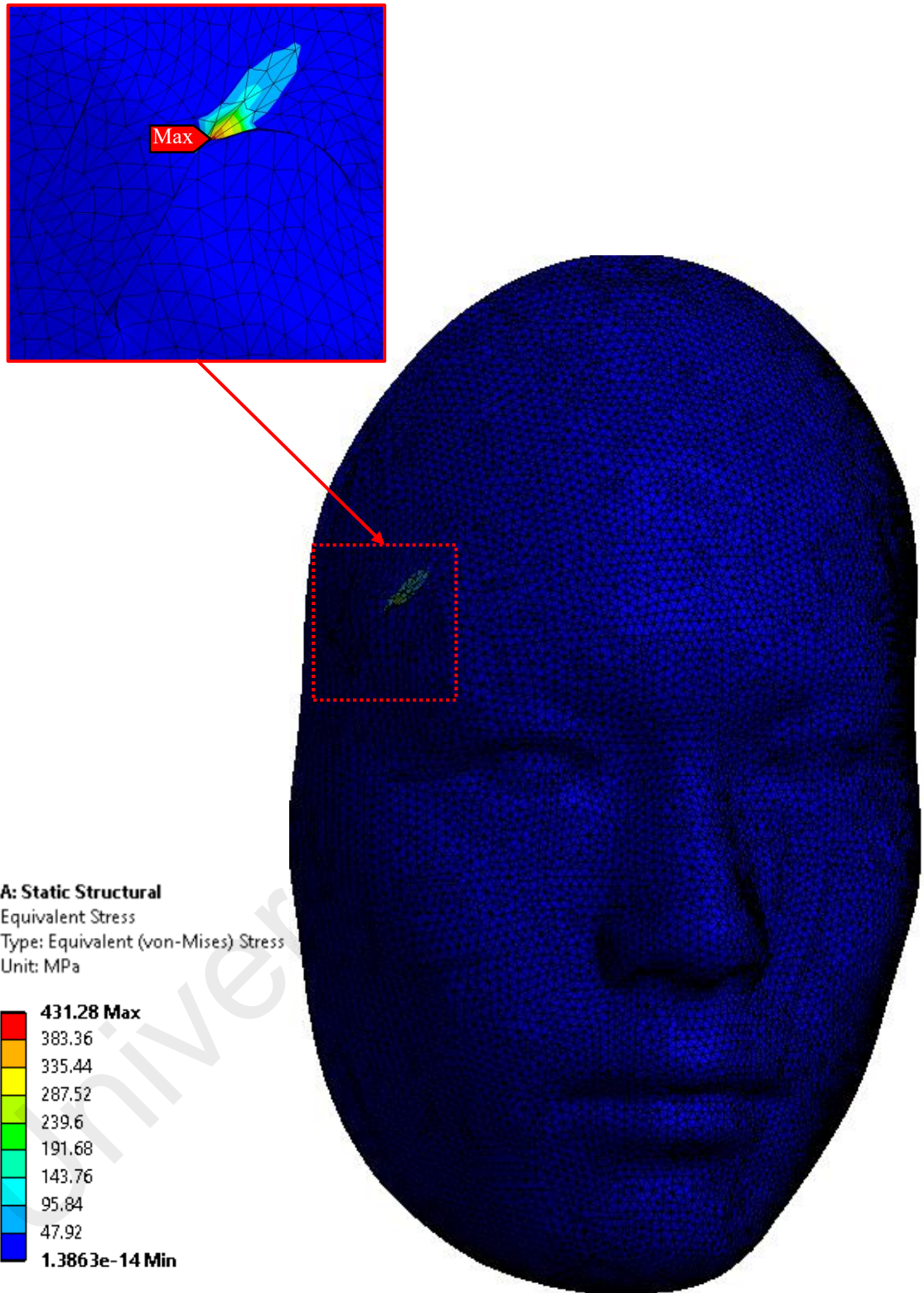


*Figure 4.12.* Rhomboid flap closure on the Asian male face model. Maximal von Mises stress concentrated at the point of rhombus edges adjacent to the primary defect closure.

## CHAPTER 5

### DISCUSSION

The study is intended to build inexpensive digital surgeries that are capable of simulating surgical outcomes as well as predicting stress contours for flaps used in reconstruction surgery with a focus on three common local flap designs: advancement, rotation, and rhomboid flaps. With lots of effort, the presented work successfully demonstrated the possibility of local flap closures on 3D face models using the FE method. These digital surgeries were carried out based on tumor diagnosis at a designated facial area where an local flap surgery is required following tumor excision. The idea was to design deformities models with local-flap-shaped holes that mimic the real-life defect present on the patient's face. From there, the FE analysis calculated a predictive wound closure for each of the local flap designs where the motions of closures were practically moved according to their method of transfer. Noted that the applications have been in the area of the face without the attachment of the skull since the study focuses more on skin recovery rather than the effect of the underlying structures.

These frameworks were made possible by replacing high-fidelity virtual surgery with efficient surrogates by modeling the human face models with nonlinear hyper-elastic, isotropic, and incompressible behavior as material properties. Certainly, the nonlinearity of the hyper-elastic law played a role in providing the skin stiffness and manifest the outcomes. Current modeling used a third-order of Yeoh's hyper-elastic parameter data from *Chanda and Unnikrishnan (2017)* in order to characterize the skin behavior. The curve fitting for the existing material coefficients,  $c_{10}$ ,  $c_{20}$ , and  $c_{30}$ , exhibited a nonlinear response that satisfactorily fit as close to the J-shaped nonlinear

response of a typical skin stress-strain curve (*Barnhill et al., 1984; Joodaki & Panzer, 2018; Ni Annaidh et al., 2012*) as shown in Figure 5.1. As proposed by *Lapeer et al. (2011)*, the Yeoh model was indeed the best choice to match the uniaxial stress-strain curve due to its advantages in corresponding to the experimental data at small and large values of strains compared to the other hyper-elastic models such as Neo-hookean, Mooney-Rivlin, Ogden, etc. (*Shahzad et al., 2015*).

Although it was stated that Burow's triangle may not be that useful in clinical settings, however, after many trials of simulations, this work decided to superimpose the Burow's triangle on the advancement and rotation flaps as the movement of the flaps were found technically limited in the absence of Burow's triangles. Closure by this approach was somehow more convenient to simulate than without the Burow's triangle. This was done to free the margins to allow more mobility for the flaps to stretch, thus ultimately relieving the stress along the closure site. Although these have been described as rarely required, Burow's triangle may still be implemented in reality as long as the skin laxity was insufficient to move towards the wounded site. This showed that the mechanical properties used may not be as flexible as the real skin elasticity, yet they served their purposes in providing relevant skin elasticity.

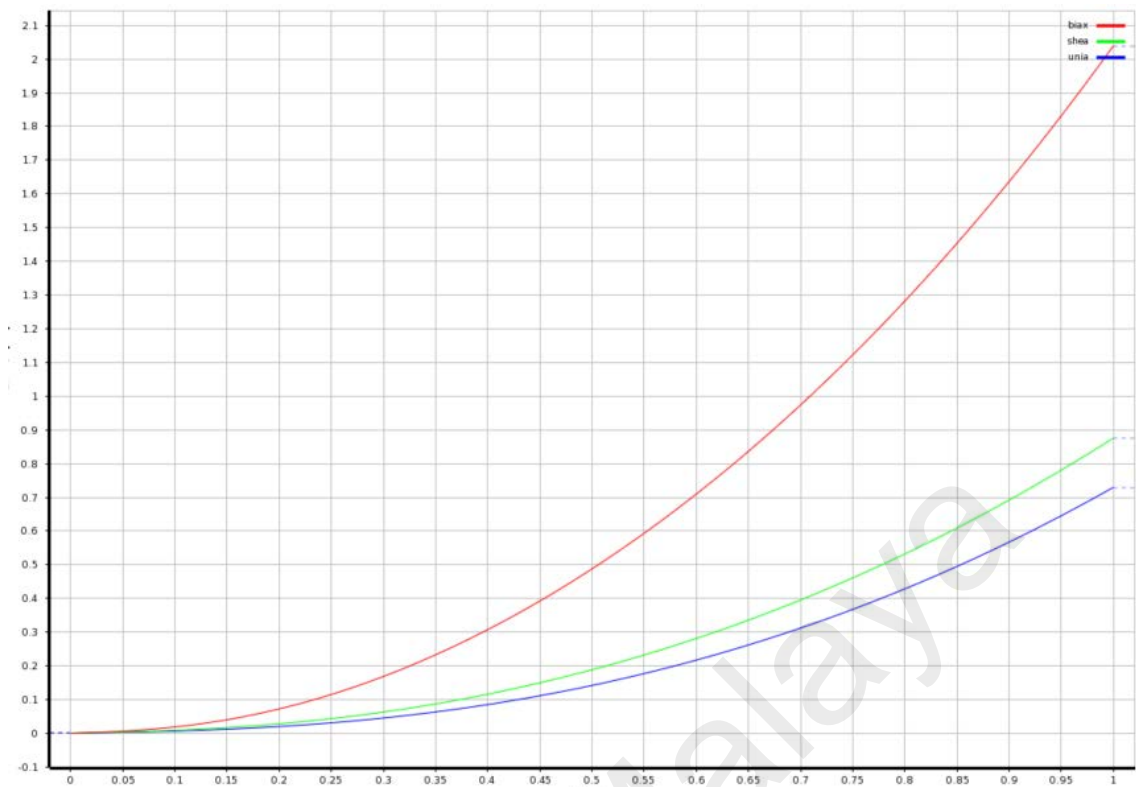


**Figure 5.1.** J-shaped nonlinear curve of the skin stress-strain generated from the existing material coefficients,  $c_{10}$ ,  $c_{20}$ , and  $c_{30}$ .

### 5.1 Case Study 1 – Accuracy and Stress Evaluation

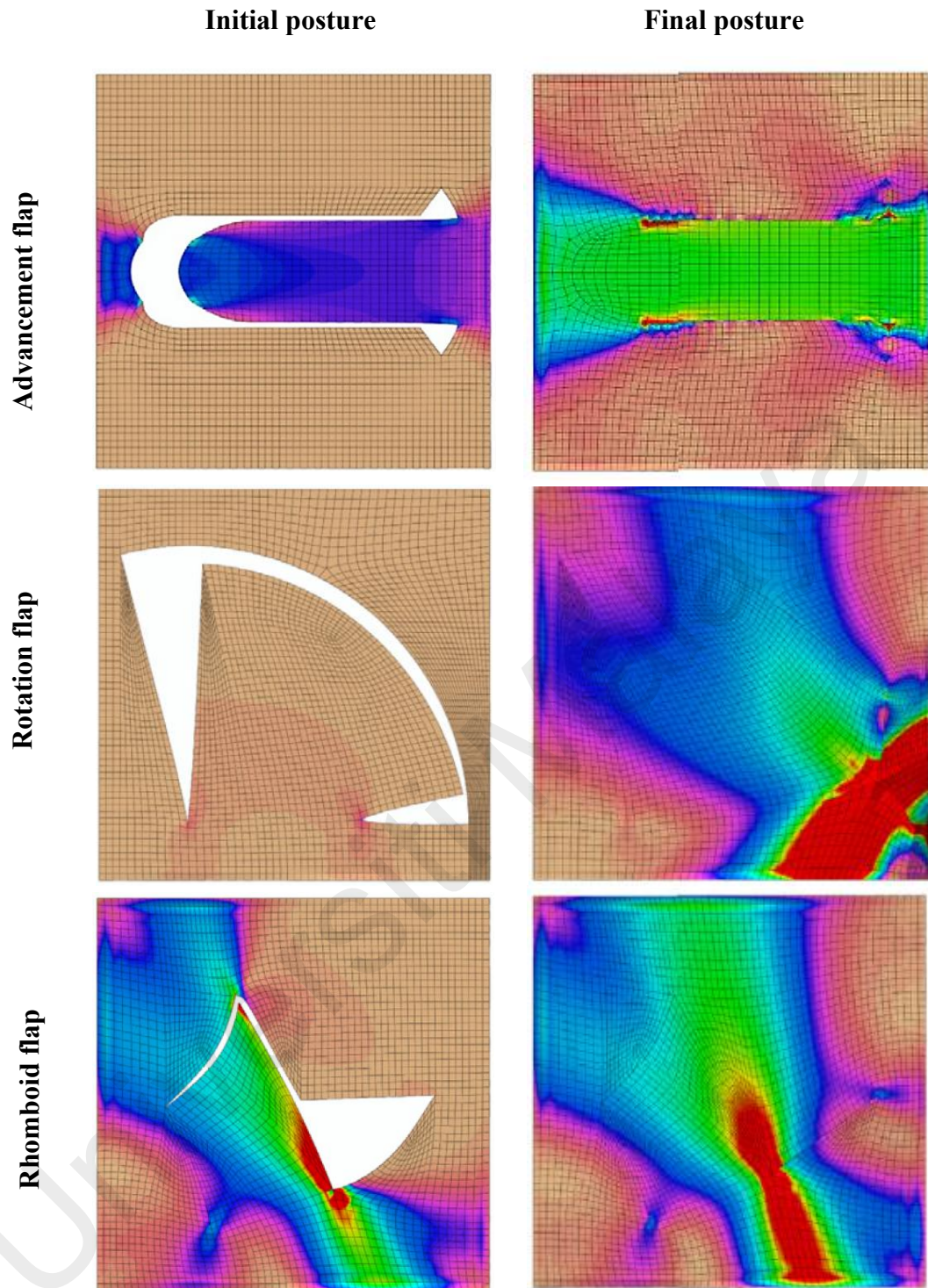
The current state of computational modeling of wound closures presents a realistic deformation and relevant wound closing that are practical for surgical simulations. The incision lines for these three flaps were designed within RSTL except for the temple-forehead junction where RSTL can be more ambiguous. The closures were executed manually where the magnitude and the orientation of the local flaps were determined with various attempts of load inputs until the opening holes were completely covered. Stress profiles for each opening-shaped hole were expressed in terms of equivalent von Mises stress. Interestingly, although these local flaps were aimed at correcting the

identical defect sizes as well as corresponding to similar material properties input, meshing sizes and boundary conditions, the resulting stress contours were found divergent from one another. This was possible considering that the stress distributions were mostly driven by the geometry of the local flap designs, unlike material behavior where its variation has a greater influence on the stress values compared to the stress contours (*Lee et al., 2019*). As seen in Figures 4.1, the equivalent stresses were predictably increased as the flaps stretched to the wounded site, which indicated the skin persistency towards elongation. The advancement flap demonstrated uniform stress along the flap, yet showed greater stress at one side of lateral corners. The rotation flap produced higher stress at its distal end with a band of stress surrounding the area. In the rhomboid flap, a band of stress confined the area of rhombus edges adjacent to the primary defect closure with high stress concentrated at its point. These peak locations can be alternatively served as validation for the present work.

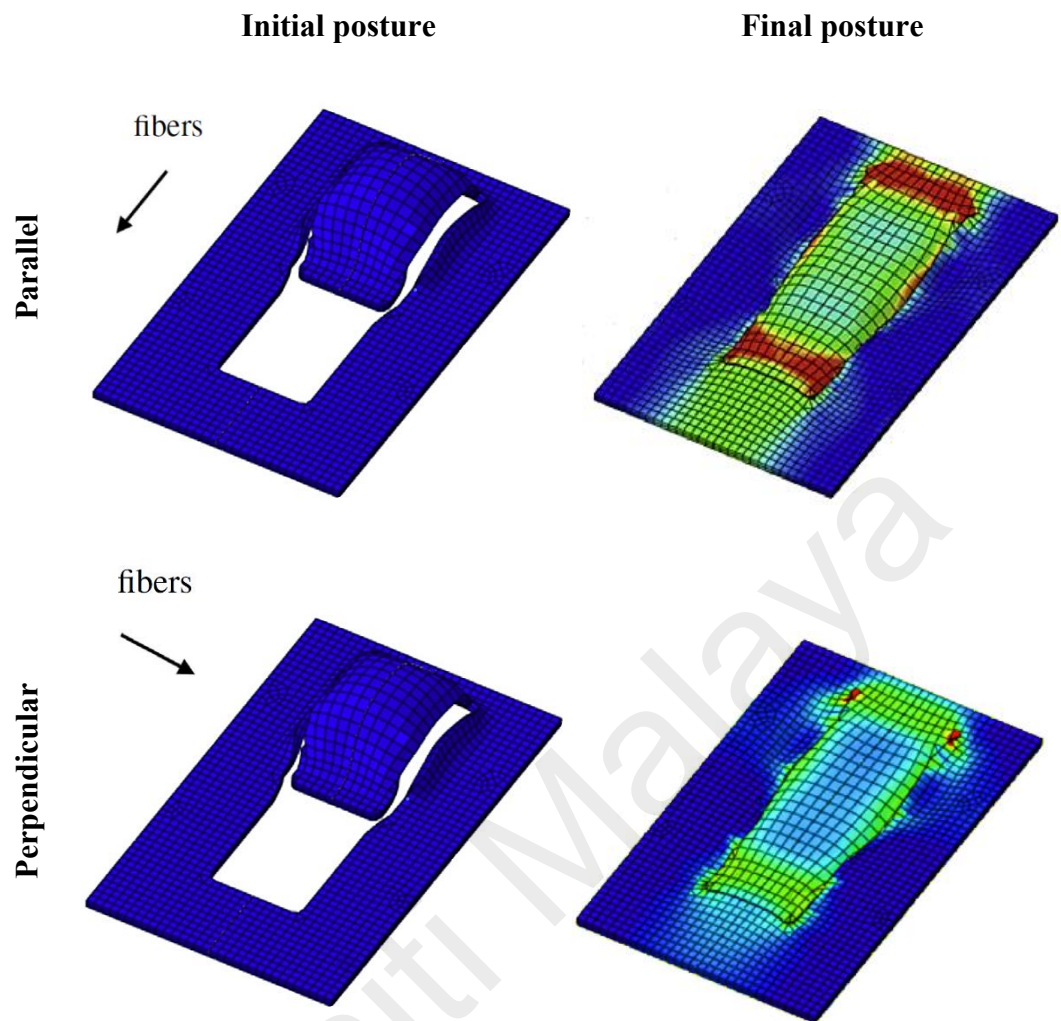
Validations were assessed by comparing current findings with the existing literature based on the location of the maximum stresses. Interestingly, all of the said peak locations were aligned with the referred literature, thereby, confirming the validity of the present work. Although the methods are diverse among the referred literature, it is wise to baseline the comparison based on the use of hyper-elastic material properties so that correlation can be made despite on having different geometry of local flap designs. To better grasp the comparison, findings from the referred literature are included with initial and final posture are arranged side by side. The color code shows the von Mises stress where red-colored illustrates the highest stress while blue-colored is at the lowest of the legend.

Figure 5.2 illustrates findings from the work of *Lee et al. (2019)*. They dealt with the three most common local flaps: advancement, rotation and transpositions with material nonlinearities by GOH hyper-elastic model. Their advancement flap closure

was reported to be highest in stress at the flap's distal ends with Burow's triangle attached at its base. The rotation flap produced greater stress distal to the flap whereas the stress in the rhomboid flap was concentrated at the suture line of the rhombus edge near the secondary closure. On the other hand, *Tepole et al. (2014)* employed the Holzapfel model in their FE model to assess the direct advancement flap with different orientations of collagen fibers. As can be seen in Figure 5.3, they excluded the utilization of Burow's triangle, yet, greater stress was still located at the distal and proximal edges of the flap. The red-colored spectrum was seen to be more heterogeneous for collagen fiber that was oriented parallel to the direction of the flap advancement than the perpendicular one. In viewing the result in Figure 5.4, *Rajabi et al. (2015)* studied a number of rhomboid flaps with the inclusion of Limberg flap configuration. Given the parametric of Limberg flap were  $\phi = \theta_2 = 60^\circ$  and  $\theta_1 = 0$  with equilateral parallelogram of 30 mm and material nonlinearities by Ogden hyper-elastic model, the maximum von Mises was almost identical to the work of *Lee et al. (2019)*. Aside from the FE modelling, the present work is also consistent with the common places of peak tensions encountered in clinical practice. *Starkman et al. (2017)* stated that the amount of arc orientation in the rotation flap caused a cutaneous deformity at the flap base, thus exerting maximal stress at the distal border of the flap instead of at the length of the flap. They also added the probability of maximal stress in the rhomboid flap corresponded to the point of rhombus edges of secondary closure. Their statement agreed with the clinical investigation presented by *Momeni and Souza (2019)*.



**Figure 5.2.** Findings from the work of *Lee et al. (2019)* that focused on advancement, rotation and rhomboid flap. Advancement flap produced higher stress at the linear corner of the flap base. Rotation flap produced greater stress distal to the flap. The rhomboid flap exerted maximal stress at the point of rhombus edges near to the secondary closure.



**Figure 5.3.** Findings from the work of *Tepole et al. (2014)* focused on direct advancement flap with parallel and perpendicular collagen fiber orientations. Both cases exerted maximal stresses at the distal edges of the flaps.

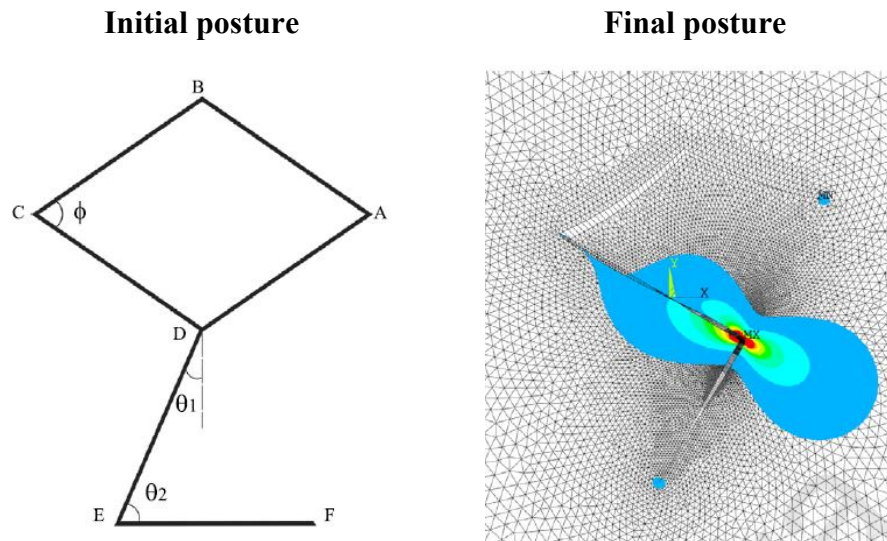


**Figure 5.4.** Findings from the work of *Rajabi et al. (2015)*. Limberg flap with  $\phi = \theta_2 = 60^\circ$  and  $\theta_1 = 0$  and edges of equal lengths. The flap exerted maximal stress at a point of distal edges adjacent to the primary closure.

## 5.2 Case Study 2 – The Sensitiveness of Local Flaps Towards Gender Group

Following the results of the previous simulations, the study attempted another investigation using Asian-like head templates, yet adding a new approach with two different genders. This case study focused on exploring the sensitivity of local flaps associated with Asian genders. The frameworks were modelled based on a clinical scenario following tumour excision that required immediate local flap surgeries. As such, the FE modelling calculated predictive wound closures resulted from the skin flap deformation with an eye towards the excision border. The magnitude and the direction of the skin flaps were determined through many trials of load inputs until both of the borders' ends of the skin flaps and defects were converged. As the skin flaps stretched towards the wounded site, the equivalent von Mises stresses were predictively increased, indicating the skin persistency towards elongation. The contour illustrated the amount

of skin elongated to indicate the decrease in skin thickness. While the red-colored contour indicated the maximum stress where the skin experienced its maximum stretches, the blue-colored contour stated otherwise. The toning down of the contour was much to indicate the skin relief from the deforming stress. Special attention to the peak location is needed to prevent overstretching and pitfall to the donor site that could lead to poor aesthetic results and persistent pain. Achieving a tension-free closure is essential to the success of reconstruction surgery.

The current case study presented the framework to model the head templates as nonlinear hyper-elastic, isotropic, and incompressible behavior. The underlying behavior properties were based on data from *Chanda and Unnikrishnan (2017)* and the material properties used were adopted into both genders. It is important to emphasize the significant variance of mechanical properties between men and women (*Luebberding et al., 2014*). However, due to the limited information available in the literature, the study considered using normalizing factors, specifically excluding the gender differences. Owing to the small differences of skin thickness below 20% between Asian genders (*Ha et al., 2005; L.O. Olsen et al., 1995*), the study assumed it is acceptable to generalize the mechanical properties. The study aimed to improve the implementation of mechanical properties separately in the near future. Nevertheless, the curve fitting generated from the existing material coefficients,  $c_{10}$ ,  $c_{20}$ , and  $c_{30}$  produced a nonlinear curve that corresponded satisfactorily to the J-shaped curve of skin nonlinear response.

The latest status of computational modeling of two different Asian genders presented appropriate wound closing that were relevant to the clinical settings and, thus, indicating the successfulness of the creation of these surrogate models. The credibility of these simulations was compared with those verified simulations in Case Study 1. Interestingly, stress profiles in rotation and rhomboid flaps demonstrated by both

genders approximately matched the stress profiles shown by the Caucasian models. Specifically, high-stress concentrations were observed at the apex of the rotation flaps whereas rhomboid flap closures showed maximal stresses located at the point of rhombus edges adjacent to the primary closures. This also applied to advancement flap closure, though the male face model demonstrated a different position of maximal than the female face model. Unlike the male face model, the maximal stress in the female face model is aligned with the previous model and thus justifies the result. Surprisingly, the male face model forecasted maximal stress at the border of the incision lines. However, the result can still be acceptable when comparing the stress distribution presented by previous studies (*Lee et al., 2019; Tepole et al., 2014*).

Another finding to take note of was the sensitivity of the local flap closures between the genders. The simulations revealed that the male has twofold higher stress than the female. This shows that the male responded more sensitively compared to the female. The discrepancy of the maximal stresses between male and female face models can be approximated to a 70.34% mean difference. The reason behind the discrepancy may be due to the face structure distinction between men and women, which also contributed to the difference in the input displacement values. In general, men and women manifest different facial structures which contribute to the masculine and feminine appearance, respectively. Men are generally broader than women in all aspects, including the head and face (*Ball et al., 2012; Luximon et al., 2015*). The influence of gender on local flap closures was significant and the present work demonstrated that models with a broader structure generated higher stress despite having similar incised coordination and geometrical designs.

## CHAPTER 6

### CONCLUSIONS

The present work provided several local flap scenarios using numerical methods associated with ethnic and gender groups. Using Caucasian and Asian head templates, detailed simulations on the advancement, rotation, and rhomboid flap designs have been performed using ANSYS software and discussed. In addition to the flaps' design, Burow's triangle has been superimposed on the advancement and rotation flaps to assist the mobility of the flaps towards the defect. Von Mises stress has been exploited to describe the deformation experienced by the skin flap due to the elongation. Overall results have demonstrated standard local flap closures along with the common places of peak tension. Moreover, a correlation with the existing results has been conducted to ensure the accuracy of the simulations. That being said, the post-operative simulations were in agreement with the mentioned literature as well as what was observed clinically and therefore concludes the establishment of these simulations.

The simulations first approached a Caucasian study as the base research, followed by Asian study where a comparative study between genders has been conducted. Therefore, two case studies were involved where Case Study 1 discussed the effect of wound closures on the Caucasian model, whereas Case Study 2 discussed the sensitivity of gender difference among Asians towards wound closures. The results from the Case Study 1 have revealed maximal stresses of 23.63 MPa for advancement flap at the tip of the flap base whereas rotation, and rhomboid flaps were at the forming point of the rotations with 150.57 MPa and 302.97 MPa, respectively. Following the validation of the simulations from the base research, the study was then carried forward to Case Study 2. In Case Study 2, a comparative gender-related effect from the local flap

closures has been discussed. It can be summarized that female produced 33.79 MPa for advancement flap, 32.82 MPa for rotation flap and 207.19 MPa for rhomboid flap whereas male produced 78.94 MPa for advancement flap, 60.19 MPa for rotation flap and 431.28 MPa for rhomboid flap. While rotation and rhomboid flaps of both genders presented maximal stresses at the apex of the flap, the advancement flap demonstrated otherwise for the male model, although the female model illustrated similar peak tension as the other flaps. Nevertheless, the results were still acceptable. Another finding found that male models generated high maximal stress compared to the female models.

The challenges in preparing and conducting the FE analysis have been identified and addressed. Several limitations of the numerical simulations should be acknowledged as boundaries were established in light of minimizing the complicity of these 3D analyses. For a start, the face models neglected the effect of multiple layering. Geometrically, a two-layer model is able to present a realistic human face since skin consists of two main distinct layers called the epidermis and dermis. Incorporating multiple layers in the FE analysis would directly affect the current stress values, although maximal stress locations would be slightly affected. Moreover, the pre-stress effect was also neglected, although *Capek et al. (2012)* justified the implication of zero pre-stress to maximal pre-stress would contrast by 44% (*Chanda & Unnikrishnan, 2017*). The inclusion of pre-stress into the models would ultimately affect the skin behavior as the effect would represent natural skin tension. Furthermore, the skin behavior model used was very straightforward where the isotropic model has the same behavior in tension and compression. It is known that compression does not occur in the skin and for that reason, accounting for anisotropic behavior may satisfy the exact skin behavior. Another notable limitation was the generalization of the hyper-elastic behavior and skin thicknesses. Mostly, the adopted parameters were collected from

older-aged cadaveric Caucasians. Though the parameters satisfied the underlying behavior in Case Study 1, there is insufficient data for the intended group in Case Study 2. Deriving the relevant parameters from experimental studies should be the next logical step in refining the models as well as incorporating multiple layers, pre-stress effects, and an anisotropic model. Last but not least, future of work research would include quantitative stress study and stress distribution around stitches region.

In summary, the findings of all case studies have been proven to be novel and thus met the research objectives successfully. Specifically, FE modeling using ANSYS software has shown its capability to impersonate the skin behavior and simulated skin-flap closure on a curved surface, yet challenging due to its limited configurations. Though ANSYS software implements a manual approach in determining the magnitude and orientation of the flaps, the software delivered the stress profiles and the mechanical movements of the three local flaps successfully. Therefore, the direction of this study specifically in exploring the sensitivity of the local flaps associated with ethnic and gender groups has been successfully conducted and discussed. On a practical level, implementing 3D head templates into computerized surgical planning may aid in assessing local flap optimization techniques more realistically. Future applications of this simulation include educational purposes as well as to counsel patients preoperatively with an end goal of creating an application or software to simulate the outcomes.

## REFERENCES

- Baker, S. R. (2015). *Advancement Flaps*. Pocket Dentistry. Retrieved 14 January from <https://pocketdentistry.com/9-advancement-flaps/>
- Ball, R. M., Luximon, Y., & Chow, E. H. C. (2012). Anthropometric Study on Chinese Head. Proceeding of Asian Workshop on 3D scanning Technologies, Tokyo, Japan.
- Barnhill, R. L., Bader, D. L., & Ryan, T. J. (1984). A Study of Uniaxial Tension on the Superficial Dermal Microvasculature. *The Journal of Investigative Dermatology*, 82(5), 511 - 514. <https://doi.org/10.1111/1523-1747.ep12261069>
- Benítez, J. M., & Montáns, F. J. (2017). The Mechanical Behavior of Skin: Structures and Models For the Finite Element Analysis. *Computers & Structures*, 190, 75 - 107. <https://doi.org/10.1016/j.compstruc.2017.05.003>
- Capek, L., Jacquet, E., Dzan, L., & Simunek, A. (2012). The Analysis of Forces Needed For the Suturing of Elliptical Skin Wounds. *Medical and Biological Engineering Computational*, 50(2), 193 - 198. <https://doi.org/10.1007/s11517-011-0857-5>
- Chanda, A., & Callaway, C. (2018). Tissue Anisotropy Modeling Using Soft Composite Materials. *Applied Bionics and Biomechanics*, 2018, 1-9. <https://doi.org/10.1155/2018/4838157>
- Chanda, A., & Unnikrishnan, V. (2017). A Realistic 3d Computational Model of the Closure of Skin Wound with Interrupted Sutures. *Journal of Mechanics in Medicine and Biology*, 17(1), 21. <https://doi.org/10.1142/s0219519417500257>
- Chanda, A., & Upchurch, W. (2018). Biomechanical Modeling of Wounded Skin. *Journal of Composites Science*, 2(4). <https://doi.org/10.3390/jcs2040069>
- Cheng, J., & Zhang, L. T. (2018). A General Approach to Derive Stress and Elasticity Tensors for Hyperelastic Isotropic and Anisotropic Biomaterials. *International Journal of Computational Methods*, 15(1). <https://doi.org/10.1142/S0219876218500287>
- Chopra, K., Calva, D., Sosin, M., Tadisina, K. K., Banda, A., De La Cruz, C., Chaudhry, M. R., Legesse, T., Drachenberg, C. B., Manson, P. N., & Christy, M. R. (2015). A Comprehensive Examination of Topographic Thickness of Skin in the Human Face. *Aesthetic Surgery Journal*, 35(8), 1007 - 1013. <https://doi.org/10.1093/asj/sjv079>
- Cuddy, L. C. (2017). Wound Closure, Tension-Relieving Techniques, and Local Flaps. *Veterinary Clinic North Am Small Anim Pract*, 47(6), 1221 - 1235. <https://doi.org/10.1016/j.cvsm.2017.06.007>
- De, S., Guilak, F., & Mofrad, M. R. K. (2010). *Computational Modeling In Biomechics*. Springer.
- Delalleau, A., Josse, G., Lagarde, J. M., Zahouani, H., & Bergheau, J. M. (2008). A Nonlinear Elastic Behavior to Identify the Mechanical Parameters of Human Skin In-Vivo. *Skin Research and Technology*, 14(2), 152 - 164. <https://doi.org/10.1111/j.1600-0846.2007.00269.x>

- Dockery, G. D. (2012). Advancement and Rotational Flaps. In *Lower Extremity Soft Tissue & Cutaneous Plastic Surgery* (pp. 177-193). Elsevier Ltd. <https://doi.org/10.1016/b978-0-7020-3136-6.00017-5>
- Ebrahimi, A., Motamedi, M. H., Nejadsarvari, N., Ebrahimi, A., & Rasouli, H. R. (2016). Salient Points in Reconstruction of Nasal Skin after Tumor Ablation with Local Flaps. *Journal of Cutaneous and Aesthetic Surgery*, 9(3), 177-182. <https://doi.org/10.4103/0974-2077.191644>
- Fabritius, B., & Tabor, G. (2016). Improving the Quality of Finite Volume Meshes Through Genetic Optimisation. *Journal of Engineering with Computers*, 32, 425-440. <https://doi.org/doi.org/10.1007/s00366-015-0423-0>
- Flynn, C. (2010). Finite Element Models of Wound Closure. *Journal of Tissue Viability*, 19(4), 137 -149. <https://doi.org/10.1016/j.jtv.2009.10.001>
- Gasson, P., Lapeer, R. J., & Karri, V. (2008). *Fitting Hyperelastic Material Models to Stress-Strain Data From an In-Vitro Experiment on Human Skin* International Conference on Polymers and Moulds Innovations, Ghent, Belgium.
- Groves, R. B., Coulman, S. A., Birchall, J. C., & Evans, S. L. (2013). An Anisotropic, Hyperelastic Model For Skin: Experimental Measurements, Finite Element Modelling and Identification of Parameters For Human and Murine Skin. *Journal of the Mechanical Behavior of Biomedical Materials*, 18, 167 - 180. <https://doi.org/10.1016/j.jmbbm.2012.10.021>
- Ha, R. Y., Nojima, K., Adams, W. P., Jr., & Brown, S. A. (2005). Analysis of Facial Skin Thickness: Defining the Relative Thickness Index. *Plastic Reconstruction Surgery*, 115(6), 1769-1773. <https://doi.org/10.1097/01.prs.0000161682.63535.9b>
- Heller, L., Cole, P., & Kaufman, Y. (2008). Cheek Reconstruction: Current Concepts in Managing Facial Soft Tissue Loss. *Semin Plast Surg*, 22(4), 294 - 305. <https://doi.org/10.1055/s-0028-1095888>
- Hendriks, F. M. (2005). *Mechanical Behavior of Human Epidermal and Dermal Layer In-Vivo* [Eindhoven University of Technology]. Eindhoven.
- Hendriks, F. M., Brokken, D., J.T.W.M, v. E., C.W.J, O., F.P.T, B., & Horsten, J. B. A. M. (2003). A Numerical-Experiment Method to Characterize the Non-Linear Mechanical Behaviour of Human Skin *Skin Research and Technology*, 9, 274 - 283.
- Hofer, S. O. P., & Mureau, M. A. M. (2011). Improving Outcomes in Aesthetic Facial Reconstruction. *Perioperative Nursing Clinics*, 6(2), 147 - 158. <https://doi.org/10.1016/j.cpen.2011.03.005>
- Igarashi, T., Nishino, K., & Nayar, S. K. (2007). *The Appearance of Human Skin* (Publication Number CUCS-024-05) University of Columbia]. USA.
- Jee, T., & Komvopoulos, K. (2014). Skin Viscoelasticity Studied In Vitro by Microprobe-based Techniques. *Journal of Biomechanics*, 47(2), 553-559. <https://doi.org/10.1016/j.jbiomech.2013.10.006>
- Jin, H. R., & Jeong, W. J. (2009). Reconstruction of Nasal Cutaneous Defects in Asians. *Auris Nasus Larynx*, 36(5), 560 - 566. <https://doi.org/10.1016/j.anl.2009.01.007>
- Joodaki, H., & Panzer, M. B. (2018). Skin Mechanical Properties and Modeling: A Review. *Journal Engineering in Medicine*, 232(4), 323 - 343. <https://doi.org/10.1177/0954411918759801>

- Kalra, A., Lowe, A., & AM, A.-J. (2016). Mechanical Behaviour of Skin: A Review. *Journal of Material Science & Engineering*, 5(4), 254. <https://doi.org/10.4172/2169-0022.1000254>
- Kang, M. (2017). *Vision-based Flap Planning Software Tool for Reconstructive Facial Plastic Surgery* [University of Toronto]. Toronto, Canada.
- Kaufman, A. J. (2016). *Practical Facial Reconstruction: Theory and Practice* (K. McGowan, Ed.). Wolters Kluwer Health.
- Kirby, S. D., Wang, B., Solomon To, C. W., & Lampe, H. B. (1998). Nonlinear, Three-Dimensional Finite Element Model of Skin Biomechanics. *Journal of Otolaryngology*, 27(3), 153 - 159
- Kolarsick, P. A. J., Kolarsick, M. A., & Goodwin, C. (2011). Anatomy and Physiology of the Skin. *Journal of the Dermatology Nurses' Association*, 3(4), 203 - 213.
- Lapeer, R. J., Gasson, P. D., & Karri, V. (2011). A Hyperelastic Finite-Element Model of Human Skin for Interactive Real-Time Surgical Simulation. *IEEE Trans Biomed Eng*, 58(4), 1013 - 1022. <https://doi.org/10.1109/TBME.2009.2038364>
- Laurent, A., Mistretta, F., Bottiglioli, D., Dahel, K., Goujon, C., Nicolas, J. F., Hennino, A., & Laurent, P. E. (2007). Echographic Measurement of Skin Thickness in Adults by High Frequency Ultrasound to Assess the Appropriate Microneedle Length for Intradermal Delivery of Vaccines. *Vaccine*, 25(34), 6423-6430. <https://doi.org/10.1016/j.vaccine.2007.05.046>
- Lee, K. S., Kim, J. O., Kim, N. G., Lee, Y. J., Park, Y. J., & Kim, J. S. (2017). A Comparison of the Local Flap and Skin Graft by Location of Face in Reconstruction after Resection of Facial Skin Cancer. *Archives of Craniofacial Surgery*, 18(4), 255 - 260. <https://doi.org/10.7181/acfs.2017.18.4.255>
- Lee, T., Gosain, A. K., Billionis, I., & Tepole, A. B. (2019). Predicting the Effect of Aging and Defect Size on the Stress Profiles of Skin from Advancement, Rotation and Transposition Flap Surgeries. *Journal of the Mechanics and Physics of Solids*, 125, 572 - 590. <https://doi.org/10.1016/j.jmps.2019.01.012>
- Limbert, G. (2017, Jul). Mathematical and Computational Modelling of Skin Biophysics: A Review. *Proc Math Phys Eng Sci*,
- Lin, C.-Y., & Lin, S.-R. (2021). Investigating the Accuracy of Ultrasound Viscoelastic Creep Imaging for Measuring the Viscoelastic Properties of a Single-Inclusion Phantom. *International Journal of Mechanical Sciences*, 199. <https://doi.org/10.1016/j.ijmecsci.2021.106409>
- Liu, Z., & Yeung, K. (2008). The Preconditioning and Stress Relaxation of Skin Tissue. *Journal of Biomedical and Pharmaceutical Engineering* 2(1), 22-28.
- Livarinen, J. T., Korhonen, R. K., Julkunen, P., & Jurvelin, J. S. (2011). Experimental and Computational Analysis of Soft Tissue Stiffness in Forearm Using a Manual Indentation Device. *Medical Engineering & Physics*, 33(10), 1245-1253. <https://doi.org/10.1016/j.medengphy.2011.05.015>
- Losco, L., Bolletta, A., Pierazzi, D. M., Spadoni, D., Cuomo, R., Marcasciano, M., Cavalieri, E., Roxo, A. C., Ciamarra, P., Cantisani, C., & Cigna, E. (2020). Reconstruction of the Nose: Management of Nasal Cutaneous Defects According to Aesthetic Subunit and Defect Size. A Review. *Medicina (Kaunas)*, 56(12). <https://doi.org/10.3390/medicina56120639>

- Lovald, S. T., Topp, S. G., Ochoa, J. A., & Gaball, C. W. (2013). Biomechanics of the Monopodicle Skin Flap. *Otolaryngol Head and Neck Surgery*, 149(6), 858 -864. <https://doi.org/10.1177/0194599813505836>
- Luebberding, S., Krueger, N., & Kerscher, M. (2014). Mechanical Properties of Human Skin In Vivo: A Comparative Evaluation in 300 Men and Women. *Skin Res Technol*, 20(2), 127-135. <https://doi.org/10.1111/srt.12094>
- Luximon, Y., Ball, R. M., & Chow, E. H. C. (2015). A Design and Evaluation Tool Using 3D Head Templates. *Computer-Aided Design and Applications*, 13(2), 153 - 161. <https://doi.org/10.1080/16864360.2015.1084188>
- Mad Mouse Design. (2007). *Basic Male Head*. Turbosquid. <https://www.turbosquid.com/3d-models/male-head-obj/346686>
- Mahmud, J., Holt, C., Evans, S., Manan, N. F. A., & Chizari, M. (2012). A Parametric Study and Simulations in Quantifying Human Skin Hyperelastic Parameters. *Procedia Engineering*, 41, 1580 - 1586. <https://doi.org/10.1016/j.proeng.2012.07.353>
- Martins, P. A. L. S., Natal Jorge, R. M., & Ferreira, A. J. M. (2006). A Comparative Study of Several Material Models for Prediction of Hyperelastic Properties: Application to Silicone-Rubber and Soft Tissues. *International Journal of Experimental Mechanics*, 42(3), 135-147. <https://doi.org/10.1111/j.1475-1305.2006.00257.x>
- Massella, D., Argenziano, M., Ferri, A., Guan, J., Giraud, S., Cavalli, R., Barresi, A. A., & Salaun, F. (2019). Bio-Functional Textiles: Combining Pharmaceutical Nanocarriers with Fibrous Materials for Innovative Dermatological Therapies. *Pharmaceutics*, 11(8). <https://doi.org/10.3390/pharmaceutics11080403>
- McGrath, J. A., & J., U. (2010). *Anatomy and Organization of Human Skin* (Vol. 1). Blackwell Publishing Ltd.
- Molinari, E., Fato, M., De Leo, G., Riccardo, D., & Beltrame, F. (2005). Simulation of the Biomechanical Behavior of the Skin in Virtual Surgical Applications by Finite Element Method. *IEEE Trans Biomedical Engineering*, 52(9), 1514 - 1521. <https://doi.org/10.1109/TBME.2005.851529>
- Momeni, A., & Souza, K. E. (2019). Local Skin Flaps. In J. Chang (Ed.), *Global Reconstructive Surgery* (pp. 86 - 99). Elsevier. <https://doi.org/10.1016/b978-0-323-52377-6.00014-8>
- Naegel, A., Heisig, M., & Wittum, G. (2011). Computational Modeling of the Skin Barrier. *Methods in Molecular Biology*, 763, 1 - 32. [https://doi.org/10.1007/978-1-61779-191-8\\_1](https://doi.org/10.1007/978-1-61779-191-8_1)
- Ni Annaidh, A., Bruyere, K., Destrade, M., Gilchrist, M. D., & Ottenio, M. (2012). Characterization of the Anisotropic Mechanical Properties of Excised Human Skin. *Journal of the Mechanical Behavior of Biomedical Materials*, 5(1), 139 - 148. <https://doi.org/10.1016/j.jmbbm.2011.08.016>
- Oliaei, S., & Chu, A. A. (2013). Local Flaps. *Encyclopedia of Otolaryngology, Head and Neck Surgery*, 1482-1486. [https://doi.org/10.1007/978-3-642-23499-6\\_348](https://doi.org/10.1007/978-3-642-23499-6_348)
- Olsen, L. O., Takiwak, H., & Serup, J. (1995). High-frequency ultrasound characterization of normal skin. Skin thickness and echographic density of 22 anatomical sites. *Skin Research and Technology*, 1(2), 74-80. <https://doi.org/10.1111/j.1600-0846.1995.tb00021.x>

- Olsen, L. O., Takiwaki, H., & Serup, J. (1995). High-Frequency Ultrasound Characterization of Normal Skin. Skin Thickness and Ecographic Density of 22 Anatomical Sites *Skin Research and Technology*, 1(2), 74-80. <https://doi.org/10.1111/j.1600-0846.1995.tb00021.x>
- Ottenio, M., Tran, D., Ni Annaidh, A., Gilchrist, M. D., & Bruyere, K. (2015). Strain Rate and Anisotropy Effects on the Tensile Failure Characteristics of Human Skin. *Journal of the Mechanical Behavior of Biomedical Materials*, 41, 241-250. <https://doi.org/10.1016/j.jmbbm.2014.10.006>
- Patria, F. F., Ceccarini, M. R., Codini, M., Conte, C., Perioli, L., Beccari, T., & Albi, E. (2019). A Role for Neutral Sphingomyelinase in Wound Healing Induced by Keratinocyte Proliferation upon 1alpha, 25-Dihydroxyvitamin D3 Treatment. *International Journal of Molecular Sciences*, 20(15). <https://doi.org/10.3390/ijms20153634>
- Pawlaczyk, M., Lelonkiewicz, M., & Wieczorowski, M. (2013). Age-Dependent Biomechanical Properties of the Skin. *Postepy Dermatol Alergol*, 30(5), 302 - 306. <https://doi.org/10.5114/pdia.2013.38359>
- Pellacani, G., & Seidenari, S. (1999). Variations in Facial Skin Thickness and Echogenicity with Site and Age. *Acta Derm Venereol*, 79, 366 -369.
- Querleux, B., Baldeweck, T., Diridollou, S., de Rigal, J., Huguet, E., Leroy, F., & Holloway Barbosa, V. (2009). Skin From Various Ethnic Origins and Aging: an In Vivo Cross-Sectional Multimodality Imaging Study. *Skin Research and Technology*, 15(3), 306-313. <https://doi.org/10.1111/j.1600-0846.2009.00365.x>
- Rajabi, A., Dolovich, A. T., & Johnston, J. D. (2015). From the Rhombic Transposition Flap Toward Z-Plasty: An Optimized Design Using the Finite Element Method. *Journal of Biomechanics*, 48(13), 3672-3678. <https://doi.org/10.1016/j.jbiomech.2015.08.021>
- Rao, J. K., & Shende, K. S. (2016). Overview of Local Flaps of the Face for Reconstruction of Cutaneous Malignancies: Single Institutional Experience of Seventy Cases. *Journal of Cutaneous and Aesthetic Surgery*, 9(4), 220 - 225. <https://doi.org/10.4103/0974-2077.197029>
- Retel, V., Vescovo, P., Jacquet, E., Trivaudey, F., Varchon, D., & Burtheret, A. (2001). Nonlinear Model of Skin Mechanical Behavior Analysis with Finite Element Method. *Skin Research and Technology*, 7, 152 - 158.
- Ruggiero, A., D'Amato, R., & Affatato, S. (2019). Comparison of Meshing Strategies in THR Finite Element Modelling. *Materials (Basel)*, 12(14). <https://doi.org/10.3390/ma12142332>
- Salgarelli, A. C., Bellini, P., Multinu, A., Magnoni, C., Francomano, M., Fantini, F., Consolo, U., & Seidenari, S. (2011). Reconstruction of Nasal Skin Cancer Defects With Local Flaps. *Journal of Skin Cancer*, 2011, 181093. <https://doi.org/10.1155/2011/181093>
- Shahzad, M., Kamran, A., Siddiqui, M. Z., & Farhan, M. (2015). Mechanical Characterization and FE Modelling of a Hyperelastic Material. *Materials Research*, 18(5), 918 - 924. <https://doi.org/10.1590/1516-1439.320414>
- Starkman, S. J., Williams, C. T., & Sherris, D. A. (2017). Flap Basics I: Rotation and Transposition Flaps. *Facial Plast Surg Clin North Am*, 25(3), 313 - 321. <https://doi.org/10.1016/j.fsc.2017.03.004>

- Tepole, A. B., Gosain, A. K., & Kuhl, E. (2014). Computational Modeling of Skin: Using Stress Profiles As Predictor For Tissue Necrosis in Reconstructive Surgery. *Comput Struct*, 143, 32 - 39. <https://doi.org/10.1016/j.compstruc.2014.07.004>
- Topp, S. G., Lovald, S., Khraishi, T., & Gaball, C. W. (2014). Biomechanics of the Rhombic Transposition Flap. *Otolaryngol Head Neck Surg*, 151(6), 952 - 959. <https://doi.org/10.1177/0194599814551128>
- Tur, E. (1997). Physiology of the Skin - Difference Between Women and Men. *Clinic in Dermatology*, 15(1), 5-16. [https://doi.org/10.1016/s0738-081x\(96\)00105-8](https://doi.org/10.1016/s0738-081x(96)00105-8)
- Turner, M. J., & Smith, W. P. (2011). Reconstruction of Forehead Skin: The Unilateral Horizontal Advancement Flap. *Journal of Oral Maxillofacial Surgery*, 69(7), 2048-2051. <https://doi.org/10.1016/j.joms.2010.10.003>
- Weinzweig, J., & Weinzweig, N. (2010). Chapter 2 - Techniques and Geometry of Wound Repair. In *Plastic Surgery Secrets Plus* (pp. 8 - 14). Mosby. <https://doi.org/https://doi.org/10.1016/B978-0-323-03470-8.00002-8>
- Wentrup-Byrne, E., Grøndahl, L., & Chandler-Temple, A. (2020). Replacement Materials for Facial Reconstruction at the Soft Tissue–Bone Interface. In *Biointegration of Medical Implant Materials* (pp. 45 - 77). Elsevier Ltd. . <https://doi.org/10.1016/b978-0-08-102680-9.00003-2>
- Wong, W. L., Joyce, T. J., & Goh, K. L. (2016). Resolving the Viscoelasticity and Anisotropy Dependence of the Mechanical Properties of Skin From a Porcine Model. *Biomechanics and Modeling in Mechanobiology*, 15(2), 433-446. <https://doi.org/10.1007/s10237-015-0700-2>
- Yousef, H., Sharma, S., Futterman, B., & T., B. N. (2019). *Anatomy, Skin (Integument), Epidermis* Petersburg, FL, USA.
- Zahouani, H., Pailler-Mattei, C., Sohm, B., Vargiolu, R., Cenizo, V., & Debret, R. (2009). Characterization of the Mechanical Properties of a Dermal Equivalent Compared with Human Skin In Vivo by Indentation and Static Friction Tests. *Skin Research and Technology*, 15(1), 68-76. <https://doi.org/10.1111/j.1600-0846.2008.00329.x>

## LIST OF PUBLICATION AND PAPER PRESENTED

Published work:

- 1) Kwan, Z., Khairu Najhan, N. N., Yau, Y. H., Luximon, Y., & Fethma, M. N. (2020). Anticipating local flaps closed-form solution on 3D face models using finite element method. *International Journal for Numerical Methods in Biomedical Engineering*, 36(11), e3390.

Universiti Malaya

## CO-AUTHORS CONSENT

**Thesis Title:** *Anticipating Local Flaps Closed-Form Solution on Nonlinear Three-Dimensional (3D) Face Models.*

The authors whose names are listed immediately below report the following details of affiliation or involvement in an organization or entity with a financial or non-financial interest in the subject matter or materials discussed in this thesis. On behalf of all authors, the corresponding author states that there is no conflict of interest.

<b>Authors</b>	<b>Affiliations</b>
Zhenli Kwan	<i>Division of Dermatology, Department of Medicine, Faculty of Medicine, University of Malaya, Malaysia</i>
Nur Nadirah Khairu Najhan	<i>Department of Mechanical Engineering, Faculty of Engineering, University of Malaya, Malaysia</i>
Yat Huang Yau	<i>Department of Mechanical Engineering, Faculty of Engineering, University of Malaya, Malaysia</i>
Yan Luximon	<i>School of Design, The Hong Kong Polytechnic University, Hong Kong</i>
Fethma M. Nor	<i>Department of Mechanical Engineering, Curtin University, Malaysia</i>

This statement is signed by all the authors to indicate agreement that the above information is true and correct,